

University of Kentucky

UKnowledge

---

Theses and Dissertations--Physics and  
Astronomy

Physics and Astronomy

---

2012

## The development and implementation of electromechanical devices to study the physical properties of Sr<sub>2</sub>IrO<sub>4</sub> and TaS<sub>3</sub>

John A. Nichols

University of Kentucky, [john.nichols@uky.edu](mailto:john.nichols@uky.edu)

[Right click to open a feedback form in a new tab to let us know how this document benefits you.](#)

### Recommended Citation

Nichols, John A., "The development and implementation of electromechanical devices to study the physical properties of Sr<sub>2</sub>IrO<sub>4</sub> and TaS<sub>3</sub>" (2012). *Theses and Dissertations--Physics and Astronomy*. 3. [https://uknowledge.uky.edu/physastron\\_etds/3](https://uknowledge.uky.edu/physastron_etds/3)

This Doctoral Dissertation is brought to you for free and open access by the Physics and Astronomy at UKnowledge. It has been accepted for inclusion in Theses and Dissertations--Physics and Astronomy by an authorized administrator of UKnowledge. For more information, please contact [UKnowledge@lsv.uky.edu](mailto:UKnowledge@lsv.uky.edu).

## **STUDENT AGREEMENT:**

I represent that my thesis or dissertation and abstract are my original work. Proper attribution has been given to all outside sources. I understand that I am solely responsible for obtaining any needed copyright permissions. I have obtained and attached hereto needed written permission statements(s) from the owner(s) of each third-party copyrighted matter to be included in my work, allowing electronic distribution (if such use is not permitted by the fair use doctrine).

I hereby grant to The University of Kentucky and its agents the non-exclusive license to archive and make accessible my work in whole or in part in all forms of media, now or hereafter known. I agree that the document mentioned above may be made available immediately for worldwide access unless a preapproved embargo applies.

I retain all other ownership rights to the copyright of my work. I also retain the right to use in future works (such as articles or books) all or part of my work. I understand that I am free to register the copyright to my work.

## **REVIEW, APPROVAL AND ACCEPTANCE**

The document mentioned above has been reviewed and accepted by the student's advisor, on behalf of the advisory committee, and by the Director of Graduate Studies (DGS), on behalf of the program; we verify that this is the final, approved version of the student's dissertation including all changes required by the advisory committee. The undersigned agree to abide by the statements above.

John A. Nichols, Student

Dr. Kwok-Wai Ng, Major Professor

Dr. Tim Gorringer, Director of Graduate Studies

The development and implementation of electromechanical devices to study the  
physical properties of  $\text{Sr}_2\text{IrO}_4$  and  $\text{TaS}_3$

---

DISSERTATION

---

A dissertation submitted in partial  
fulfillment of the requirements for  
the degree of Doctor of Philosophy  
in the College of Arts and Sciences  
at the University of Kentucky

By  
John Nichols  
Lexington, Kentucky

Director: Dr. Kwok-Wai Ng, Professor of Physics  
Lexington, Kentucky 2012

Copyright© John Nichols 2012

## ABSTRACT OF DISSERTATION

The development and implementation of electromechanical devices to study the physical properties of  $\text{Sr}_2\text{IrO}_4$  and  $\text{TaS}_3$

Transition metal oxides (TMO) have proven to exhibit novel properties such as high temperature superconductivity, magnetic ordering, charge and spin density waves, metal to insulator transitions and colossal magnetoresistance. Among these are a spin-orbit coupling (SOC) induced Mott insulator  $\text{Sr}_2\text{IrO}_4$ . The electric transport properties of this material remain finite even at cryogenic temperatures enabling its complex electronic structure to be investigated by a scanning tunneling microscope. At  $T = 77$  K, we observed two features which represent the Mott gap with a value of  $2\Delta \sim 615$  meV. Additionally an inelastic loss feature was observed inside this gap due to a single magnon excitation at an energy of  $\sim 125$  meV. These features are consistent with similar measurements with other probes. In addition to these features, at  $T = 4.2$  K lower energy features appear which are believed to be due to additional magnetic ordering. Another material that exhibits a unique physical behavior is the sliding charge density wave (CDW) material  $\text{TaS}_3$ . It is a quasi-one dimensional material that forms long narrow ribbon shaped crystals. It exhibits anomalies including non-ohmic conductivity, a decrease in the Young's modulus, a decrease in the shear modulus and voltage induced changes in the crystal's overall length. In addition, we have observed the torsional piezo-like response, voltage induced torsional strain (VITS), in  $\text{TaS}_3$  which was first discovered by Pokrovskii *et. al.* in 2007. Our measurements were conducted with a helical resonator. The VITS response has a huge effective piezoelectric coefficient of  $\sim 10^{-4}$  cm/V. In addition we have concluded that the VITS is a very slow response with time constants of  $\sim 1$  s near the CDW depinning threshold, that these time constants are dependent on the CDW current, and we suggest that the VITS is due to residual twists being initially present in the crystal.

KEYWORDS: scanning tunneling microscope, Mott insulator, spin-orbit coupling, charge density wave, voltage induced torsional strain

Author's signature: John Nichols

Date: October 4, 2012



The development and implementation of electromechanical devices to study the  
physical properties of  $\text{Sr}_2\text{IrO}_4$  and  $\text{TaS}_3$

By  
John Nichols

Director of Dissertation: Kwok-Wai Ng

Director of Graduate Studies: Tim Gorringer

Date: October 4, 2012

## ACKNOWLEDGMENTS

My academic pursuit for this doctoral degree would never have been successful without the love, support and inspiration from so many people it is impossible to properly thank them all. I would like to begin by thanking my lovely wife Amanda for all the love and support she provided me through this endeavor. I am also equally grateful for my parents Roy and Wanda. In addition, I greatly appreciate all the teachers and professors I have had through the years. In particular, I would like to thank both my official advisor Kwok-Wai Ng and my “adopted” advisor Joseph Brill for opening their laboratories, enabling me to perform the experiments presented in this thesis and for all the discussions and direction I have obtained from them. In addition, I would like to thank Gene Baber for all the help he provided. I am thankful for Jim Morris, Charles Tipton and Steve Maynard for machining the new pieces required for this work. I would also like to thank Greg Porter, Bill Fuqua and Rick Carr for their help building and maintaining the electronics utilized. I am appreciative of Gang Cao for providing the high-quality  $\text{Sr}_2\text{IrO}_4$  samples and for Robert Throne of Cornell University for providing the high-quality  $\text{TaS}_3$  samples. Also I would like to thank my entire Ph.D. committee. I would also like to thank the numerous graduate students who have aided me. This work was supported with the following grants from the National Science Foundation: DMR-0800367 and EPS-0814194.

# TABLE OF CONTENTS

Acknowledgments . . . . .	iii
Table of Contents . . . . .	iv
List of Figures . . . . .	vi
List of Tables . . . . .	xii
Chapter 1 Introduction . . . . .	1
I Determination of the electronic properties of $\text{Sr}_2\text{IrO}_4$ with a scanning tunneling microscope . . . . .	3
Chapter 2 Tunneling . . . . .	4
2.1 Square Barrier . . . . .	5
2.2 Trapezoid Barrier . . . . .	7
2.3 Density of States . . . . .	8
2.4 Bardeen Transfer Hamiltonian . . . . .	9
Chapter 3 Scanning Tunneling Microscopy . . . . .	16
3.1 Introduction . . . . .	16
3.2 STM Scanner . . . . .	16
3.3 Coarse Approach . . . . .	18
3.4 STM Assembly . . . . .	20
3.5 Imaging . . . . .	22
3.6 Spectroscopy . . . . .	25
Chapter 4 Background of $\text{Sr}_2\text{IrO}_4$ . . . . .	28
4.1 Spin-orbit Coupling . . . . .	28
4.2 Crystal Field Splitting . . . . .	29
4.3 Crystal Structure . . . . .	29
4.4 Electronic Structure . . . . .	31
4.5 Magnetic Ordering . . . . .	36
4.6 Determination of Mott gap in $\text{Sr}_2\text{IrO}_4$ . . . . .	40
4.7 Magnon excitations in $\text{Sr}_2\text{IrO}_4$ . . . . .	40
4.8 Mott Insulator . . . . .	41
4.9 Hubbard Model . . . . .	42
Chapter 5 Tunneling in $\text{Sr}_2\text{IrO}_4$ . . . . .	44
5.1 Sample Preparation . . . . .	44
5.2 STM Setup . . . . .	49

5.3	Experimental Results and Analysis . . . . .	53
II	Development of a scanning tunneling microscope with long range lateral motion . . . . .	63
Chapter 6	Scanning tunneling microscope with long range lateral motion . .	64
6.1	Design . . . . .	65
6.2	Experiment . . . . .	73
III	Investigations of voltage induced torsional strain in TaS <sub>3</sub> . . . . .	77
Chapter 7	Background of TaS <sub>3</sub> . . . . .	78
7.1	Resistance . . . . .	82
7.2	Elastic Properties . . . . .	83
7.3	Voltage Induced Length Changes . . . . .	85
Chapter 8	Experimental Setup . . . . .	87
8.1	Sample Configuration . . . . .	87
8.2	RF Cavity . . . . .	89
8.3	PM Technique . . . . .	93
8.3.1	Phase Modulation . . . . .	93
8.3.2	Shear Compliance . . . . .	94
8.3.3	Square Wave Response . . . . .	95
8.3.4	Induced EMF . . . . .	96
8.4	Hysteresis Loops . . . . .	96
8.4.1	Frequency Modulation . . . . .	96
8.4.2	Static technique . . . . .	97
8.4.3	Dynamic technique . . . . .	98
Chapter 9	Voltage Induced Torsional Strain in TaS <sub>3</sub> . . . . .	99
Chapter 10	Temperature and External Toque dependence of VITS . . . . .	114
10.1	Torque Dependence . . . . .	114
10.2	Temperature Dependence . . . . .	122
Chapter 11	Modeling of VITS . . . . .	128
11.0.1	Qualitative Modeling . . . . .	128
11.0.2	Quantitative Modeling . . . . .	129
Chapter 12	Conclusions . . . . .	136
	Bibliography . . . . .	138
	Vita . . . . .	146

## LIST OF FIGURES

2.1	a) An electron traveling in the $+z$ -direction incident upon a square potential barrier. Upon interacting with the barrier the electron will either be b) reflected traveling in the $-z$ -direction or c) transmitted continuing in the $+z$ -direction. . . . .	7
2.2	When $V_{\text{bias}}$ is applied it enables electrons with energy between $E$ and $E + eV_{\text{bias}}$ to tunnel across the gap. The solid regions are filled states, the striped region is the energy window allowing electron tunneling and the arrow indicates the direction of the tunneling electrons. . . . .	8
2.3	An arbitrary potential barrier ( $V(r)$ ) with wave functions for $H_1$ and $H_2$ represented as solid and dotted lines respectively. . . . .	11
2.4	Plots of $f(E_F - eV + \epsilon) - f(E_F + \epsilon)$ where $E = E_F + \epsilon$ for several temperatures. . . . .	14
3.1	Illustration of STM with 1) the Macor body, 2) one of six walker legs, 3) the sapphire prism, 4) the scanner and 5) the STM tip, 6) the beryllium copper plate, 7) the sapphire ball and 8) the nylon screws. . . . .	19
3.2	First stage amplifier with output $V_{\text{out}} = -(10 \text{ M}\Omega)I_{\text{tunnel}}$ . . . . .	22
3.3	Constant current image with atomic resolution of HOPG surface obtained with $V_{\text{bias}} = 1.0 \text{ V}$ and $I_{\text{set}} = 100 \text{ pA}$ . The yellow hexagon displays a single honeycomb cell of its crystal structure. . . . .	25
3.4	Three illustrations of the flow of electrons between tip and sample with arbitrary sample LDOS and constant tip LDOS. (left) $V_{\text{bias}} = 0$ so no electrons will tunnel. (middle) $V_{\text{bias}} > 0$ so electrons in the tip will tunnel into empty states in the sample. (right) $V_{\text{bias}} < 0$ so electrons in the sample will tunnel into empty states in the tip. . . . .	27
4.1	Effects of octahedral crystal field splitting on the d-orbital. . . . .	29
4.2	The crystal structure of $\text{Sr}_2\text{IrO}_4$ . (upper left) and (right) The Sr, Ir and O atoms are white, green and red respectively. The $\text{IrO}_6$ octahedra are colored blue. (upper left) View along c-axis clearly illustrates rotation of $\text{IrO}_6$ octahedra. (lower left) The Sr, Ir and O atoms are grey, red and black respectively. The three layers labeled I, II and III are the same as those labeled in Figure 5.5. . . . .	30
4.3	Temperature dependence of the electrical transport properties in $\text{Sr}_2\text{IrO}_4$ measured along the a-axis (blue) and the c-axis (red). [26] . . . . .	32
4.4	a) Band structure of a simple metal. b) Mott gap generated by unrealistically large $U$ . c) Band splitting due to only SOC results in metallic state. d) Modest $U$ in presence of SOC results in insulating state. [27] . . . . .	33
4.5	a) The effects of the $5d$ band in $\text{Sr}_2\text{IrO}_4$ due to crystal field splitting and spin-orbit coupling. b) The effects due to SOC and the on-site Coulomb interaction on the $t_{2g}$ band. . . . .	34

4.6	The right panel are LDA band structure calculations considering a) no SOC or U b) only SOC c) both SOC and U d) only U. The left panel represents the Fermi surface except for c) which shows the topology of the valence band maxima. [27] . . . . .	36
4.7	Temperature dependence of the magnetization in $\text{Sr}_2\text{IrO}_4$ along the a-axis (red) and c-axis (blue), where $T_C = T_N = 240$ K. (Inset) Low temperature magnetization along the c-axis. [31]. . . . .	38
4.8	Illustration of $J_{\text{eff},1/2}$ moment alignment in four layers of the unit cell for $T < T_N$ with $H = 0$ (left) and $H > H_C = 0.2$ T (right) [32]. . . . .	39
5.1	Contact mode AFM images of $3 \times 3 \mu\text{m}^2$ area of $\text{Sr}_2\text{IrO}_4$ surface taken with $F_N = 1.16$ nN. The images were obtained on the same sample a) $\sim 20$ minutes after cleaving and b) $\sim 4$ weeks after cleaving. . . . .	47
5.2	The sample mounting configuration of $\text{Sr}_2\text{IrO}_4$ for STM experiments. The samples were initially attached with a strong insulating epoxy and then electrical contact to the crystal was made with silver paint. . . . .	48
5.3	The design of the probe used for cryogenic STM experiments. The image on right is magnification of the end of the probe which rests inside the vacuum chamber. . . . .	51
5.4	Scanning electron microscope images of an electrochemically etched tungsten tip with a magnification of a) $\times 500,000$ and b) $\times 80$ . . . . .	52
5.5	(top) A constant current image of $109 \times 109 \text{ nm}^2$ area of $\text{Sr}_2\text{IrO}_4$ surface taken with $V_{\text{bias}} = 300$ mV and $I_{\text{set}} = 200$ pA. The three layers labeled I, II and III are three different atomic layers as indicated in Figure 4.2. (bottom) A line profile of the image represented as a white line in the image. . . . .	59
5.6	A constant current image of $11.2 \times 11.2 \text{ nm}^2$ area of Layer II of the same $\text{Sr}_2\text{IrO}_4$ surface illustrated in Figure 5.5. It was obtained with $V_{\text{bias}} = 300$ mV and $I_{\text{set}} = 200$ pA. . . . .	60
5.7	The red curve is the differential tunneling conductance of $\text{Sr}_2\text{IrO}_4$ at $T = 77$ K. It was acquired from a lock-in amplifier with $V_{\text{mod}} = 4$ mV and $f_{\text{mod}} = 703.4$ Hz. The dashed lines are fits to Equation 5.1. Inset: The orange curve is the derivative of the even component of the differential tunneling conductance. . . . .	61
5.8	a) The differential tunneling conductance of $\text{Sr}_2\text{IrO}_4$ at $T = 4.2$ K. It was acquired from a lock-in amplifier with $V_{\text{mod}} = 10$ mV and $f_{\text{mod}} = 704.2$ Hz. b) The voltage derivative of the differential tunneling conductance ( $d^2I/dV^2$ ) at $T = 4.2$ K (blue) and $T = 77$ K (red). The data was obtained by taking a numerical derivative of the differential conductance presented above. The dashed line is a guide for the eye. . . . .	62
6.1	Illustration of the walker assembly: 1) piezoelectric tube, 2) sapphire disk and 3) central Macor piece. . . . .	66

6.2	(top left) The walker assembly in the relaxed state with all electrodes held at ground potential. (top middle) The walker assembly with legs elongated and contracted for motion in the z-direction. (top right) The walker assembly with legs bent for motion in the x-direction. (Bottom) Diagram of how individual pulses are orchestrated to obtain net motion in all four directions. . . . .	67
6.3	STM Assembly: 1) stainless steel screws, 2) top Macor piece, 3) top alumina plate, 4) walker assembly, 5) stiff springs, 6) bottom alumina plate, 7) bottom Macor piece, 8) soft springs, 9) stainless steel bars and 10) scanner with tip. . . . .	69
6.4	The twelve bipolar voltage pulses generated by the new electronics necessary to drive the STM at cryogenic temperatures. Pulses of appropriate polarity and timing are applied to the electrodes of the walker legs to obtain motion in a given direction. . . . .	71
6.5	Voltage dependence of the step size in all four directions with a normal force of 2.5 N applied to the walker. (Inset) The force dependence of the the step size with $V_{pp} = 100$ V. The dashed curves are guides for the eye. . . . .	72
6.6	(Top left) An atomic resolution image of HOPG obtained with $V_{bias} = 200$ mV and $I_{set} = 1.0$ nA. (Top right) The sample configuration which consists of a substrate of HOPG with 60 nm thick gold layer on half of it. (Bottom right) An STM image of an $109 \times 109$ nm <sup>2</sup> area of the gold side of the sample taken with $V_{bias} = 1.0$ V and $I_{set} = 1.0$ nA. (Bottom left) An STM image of an $109 \times 109$ nm <sup>2</sup> area of the HOPG side of the sample taken with $V_{bias} = 1.0$ V and $I_{set} = 1.0$ nA. It has been adjusted to have the same false color scale as the gold image on the bottom right. . . . .	74
6.7	All images represent data obtained from a $109 \times 109$ nm <sup>2</sup> area of the sample near the gold-graphite interface obtained with $V_{bias} = 1.0$ V and $I_{set} = 1.0$ nA. (Top left) A three-dimensional image with the flat HOPG region nearest to the viewer. (Right) A two-dimensional image with a non-linear false color scale to emphasize the interface. (Bottom left) Two line profiles taken from the data with line 1 represented by unfilled circles and line 2 by filled circles. . . . .	75
7.1	a) Atomic structure (top) and energy dispersion (bottom) for a one-dimensional system for $T > T_P$ . b) Atomic structure and energy dispersion for $T < T_P$ [61]. . . . .	79
7.2	a) Crystal structure of NbSe <sub>3</sub> . The Nb and Se atoms are represented by filled and unfilled circles respectively [72]. . . . .	80
7.3	Temperature dependence of the resistance of TaS <sub>3</sub> (Sample E). The line in b) is a fit to Equation 7.2. . . . .	83
7.4	Voltage dependence of a) shear compliance ( $J=1/G$ ) and b) internal friction ( $\tan \delta$ ) for sample E. The depinning threshold is marked with vertical arrows. . . . .	84
7.5	Voltage dependence of the change in overall length of the TaS <sub>3</sub> crystal (top) and relative change in resistance (bottom) [81]. . . . .	85

7.6	The position dependence the CDW phase ( $\phi = \frac{dq}{dz}$ ) and the change in the CDW wave vector ( $\Delta q$ ) [82]. . . . .	86
8.1	a) Original sample mounting method with a TaS <sub>3</sub> and NbSe <sub>3</sub> crystal connected at a steel wire. b) More robust configuration with a thin gold film on a single TaS <sub>3</sub> crystal with a steel wire attached at its center [84]. . . .	90
8.2	Configuration of sample relative to the helix. Both sample types are mounted this way. . . . .	91
8.3	Block diagram of the experimental setup including the electronics and RF cavity. [85] . . . . .	92
9.1	(left) Sample setup with several BSCCO wires which serve as mirrors and electrical contact to mechanically free end. (bottom middle) Magnification of BSCCO mirrors. (top middle) Diagram of experimental setup. (bottom right) Electrical resistance versus applied current. (top right) Twist angle versus applied current acquired simultaneously with the resistance. (inset of top right) Another sample from same parent sample mounted in opposite configuration [74]. . . . .	100
9.2	a) Twist angle of the sample versus applied sample voltage for samples A (open circles) and B (filled circles) in arbitrary units. Inset of a) twist angle versus voltage for a third sample. b) Normalized electrical resistance and normalized shear compliance versus applied sample voltage. The unfilled (filled) circles and triangles respectively represent $R/R_0$ and $J/J_0$ for sample A (B). Inset of b) phase shifts of VITS (unfilled triangle) and J (filled triangle) response versus applied voltage for 3 Hz and 10 Hz. . . .	102
9.3	Dynamic VITS response to square wave voltage applied to sample A (a) and B (b) for several different frequencies. The in-phase and quadrature response are on top and bottom respectively. Inset of a) The in-phase response for small voltages. . . . .	104
9.4	Inducted AC voltage for samples A and B with 10 Hz oscillating torque applied to the sample. . . . .	106
9.5	Hysteresis loops at several different frequencies for samples C and D. Each curve is a numerical average of several cycles. The appropriate depinning thresholds are shown on the bottom of each graph. There is an arbitrary vertical offset for clarity. . . . .	107
9.6	Time dependence of the VITS response due to square wave potentials of $V = 1.5V_T$ and $V = 3V_T$ . This response with periods of $T = 0.1$ s, 1 s and 10 s is normalized to its period. The lower right panel shows the phase of the applied square wave. . . . .	109
9.7	Frequency dependence of VITS response due to square waves applied to sample C for $V = 1.05V_T$ , $V = 2.25V_T$ and $V = 3V_T$ . The inset shows the voltage dependence of the square wave response for 5 Hz (triangles) and 0.2 Hz (circles). The in-phase and quadrature response is represented by filled and unfilled symbols respectively. The curves represent fits to Equation 9.1. . . . .	110



9.8	Frequency dependence of VITS response due to square waves applied to sample C for $V = 1.2V_T$ , $V = 2.1V_T$ and $V = 3V_T$ . The inset shows the voltage dependence of the square wave response for 5 Hz (triangles) and 0.2 Hz (circles). The in-phase and quadrature response is represented by filled and unfilled symbols respectively. The curves represent fits to Equation 9.3. . . . .	111
9.9	The voltage dependence of the parameters from Equation 9.1 (Sample C) and 9.3 (Sample D). Sample C is represented by filled symbols and sample D by unfilled. The width of the distribution of relaxations times for sample D is shown in the bottom panel. The curves are guides for the eye. . . .	112
10.1	Voltage dependence of resistance and shear compliance at $T = 77$ K for sample E. Values for applied magnetic currents of $I_B = 0.9$ A (upward pointing triangles) and $I_B = 0.3$ A (downward pointing triangles) are presented. Inset $1/V_{J_0}$ dependence on $I_B$ used to obtain twist amplitude of $\partial\phi/\partial V_T \sim 12^\circ/\text{A}$ . . . . .	118
10.2	a) Voltage dependence of the VITS ( $\epsilon_\omega$ ) at $T = 77$ K due to a 10 Hz square wave voltage applied to sample. The in-phase symbols are filled and the quadrature symbols are unfilled. Data is presented for $I_B = + 0.3$ A and $I_B = - 0.6$ A. b) Frequency dependence of $\epsilon_\omega$ for $I_B = + 0.3$ A and $I_B = + 0.9$ A at $V_{\text{square}} = 400$ mV and $V_{\text{square}} = 700$ mV respectively. The curves are fits to Equation 9.3. The twist angle is $\partial\phi/\partial I_B \sim 12^\circ/\text{A}$ . . . . .	119
10.3	The dependence of parameters to fits to Equation 9.3 on $I_B$ for sample E with 700 mV (closed symbols) and 400 mV (open symbols). Note that some error bars are smaller than the points. The twist angle is $\partial\phi/\partial I_B \sim 12^\circ/\text{A}$ . . . . .	120
10.4	Hysteresis loops for several different values of $I_B$ for sample F. They were obtained with 0.75 V, 0.3 Hz triangle wave at $T = 77$ K. There is a vertical offset for clarity and arrows mark direction of each loop. The twist angle is $\partial\phi/\partial I_B \sim 5^\circ/\text{A}$ . . . . .	121
10.5	a) Voltage dependence of resistance and shear compliance for temperatures of 90 K, 100 K, 110 K and 120 K of sample G. b) Voltage dependence of the VITS response due to a 10 Hz square wave applied to the sample for the same temperatures as in a). . . . .	124
10.6	Frequency dependence due to $V = V_{\text{on}} + 100$ mV = 170 mV square wave applied to the sample at $T = 90$ K and 110 K for sample G. The filled and open symbols represent the in-phase and quadrature responses respectively. The curves are fits to Equation 9.3. . . . .	125
10.7	The temperature dependence for sample G of a) parameters of fits to Equation 9.3 b) square-wave and CDW onset voltages and c) the CDW current and $I_{\text{CDW}}\tau_0$ . When not visible, the error bars are smaller than the symbols. . . . .	126
11.1	Simulated hysteresis loops from Equation 11.1 for four different periods. . . . .	129

11.2	The alignment of the CDW wavefronts in an untwisted crystal due to applied voltage for a) sample with CDWs that have never been depinned, b) samples that have been above positive threshold and c) samples that have been below negative threshold. d) The general voltage dependence of $\Delta q_0(z)$ . . . . .	130
11.3	Voltage dependence of relaxation time constants associated with VITS (sample D), changes in the longitudinal wave vector ( $\Delta q_z$ ) [92] and changes in the shear modulus ( $\Delta G = 1/J$ ) [87]. The length and temperature of each sample is presented. . . . .	134

## LIST OF TABLES

2.1	Energy resolution $\Delta\epsilon$ for common temperatures. . . . .	15
3.1	Names of piezoelectric materials used with $d_{31}$ values. . . . .	18
4.1	Comparison of typical values for spin-orbit coupling and Coulomb interactions for $3d$ and $5d$ transition metals [29]. . . . .	33
5.1	Measured values of the Mott gap ( $2\Delta$ ) in $\text{Sr}_2\text{IrO}_4$ with various experimental probes. . . . .	57
8.1	Physical properties of the seven $\text{TaS}_3$ samples used, where $l$ , $w$ and $t$ are the length, width and thickness of the crystal respectively. . . . .	89

## Chapter 1 Introduction

This thesis consists of three parts involving exhaustive work in two laboratories. In the first part of this thesis (Chapters 2 – 5) I will discuss our measurements on  $\text{Sr}_2\text{IrO}_4$  with a scanning tunneling microscope.  $\text{Sr}_2\text{IrO}_4$  is a  $5d$  transition metal oxide which was predicted to be a good metal based on a smaller on-site Coulomb interaction compared to its  $3d$  and  $4d$  counterparts. Surprisingly,  $\text{Sr}_2\text{IrO}_4$  has an insulating ground state due to an appreciable spin-orbit coupling interaction. Even with the insulating behavior, the competition between electron-electron coupling and spin-orbit coupling results in a finite electrical resistance in typical samples even at cryogenic temperatures. This enables the unique electronic properties of  $\text{Sr}_2\text{IrO}_4$  to be investigated with a scanning tunneling microscope (STM). In this thesis I will present our work on the single layered Mott insulator  $\text{Sr}_2\text{IrO}_4$  with an STM. We have obtained high resolution STM images of the sample surface which include single atomic steps and differential tunneling conductance at cryogenic temperatures. We have measured the insulating gap through differential tunneling spectroscopy to be consistent with similar results from optical conductivity, angle-resolved photoemission spectroscopy and resonant inelastic x-ray (RIXS) experiments. We have also observed a single magnon excitation comparable to the values obtained through RIXS and Raman scattering experiments. At low temperatures, additional low energy features were observed which suggests additional magnetic ordering is present which is consistent with the magnetization data.

In the second part of this thesis (Chapter 6) I will discuss our work designing and constructing a new STM. This STM is capable of translating the tip macroscopic distances in two-dimensions while maintaining high enough resolution to observe periodic atomic structure on highly oriented pyrolytic graphite. The extra degree of

freedom is necessary for experiments such as studying the position dependence of electronic properties of charge density wave conductors and studying the proximity effect near a normal metal-superconducting interface. This device is compact enough to fit inside our cryogenic probe and is made entirely out of non-magnetic materials for potential experiments inside a magnetic field. In this thesis I will discuss in detail the design, operation and present some results illustrating the capabilities of this newly constructed STM.

In the final part of this thesis (Chapters 7 – 11) I will discuss our results observing a torsional piezo-like response in the charge density wave conductor TaS<sub>3</sub> called voltage induced torsional strain (VITS). This phenomenon, which was first discovered in 2007 by Pokrovskii *et. al.*, consists of the ribbon shaped crystals of TaS<sub>3</sub> twisting when a large enough potential difference is applied along its length. This response is associated with the depinning of the CDW from the underlying crystal lattice. We have shown that this response has a magnitude of  $\sim 0.1^\circ$ , has a hysteretic dependence on voltage and is very slow with relaxational time constants in excess of 1 s near threshold. In addition, I will discuss the dependence of VITS on applied torque and temperature and a model which we suggest is the mechanism of this unique effect.

## PART I

Determination of the electronic properties of  $\text{Sr}_2\text{IrO}_4$  with a scanning  
tunneling microscope

## Chapter 2 Tunneling

In 1981, Swiss scientist Heinrich Rohrer and German scientist Gerd Binnig made an enormous impact on the field of nano science with their discovery of the scanning tunneling microscope (STM). Their work was conducted at the IBM research facility in Zurich, Switzerland. Their work was so influential toward the field of science that Rohrer and Binnig were awarded the Nobel Prize in Physics in 1986, a short five years after the instrument's initial development. Since its discovery, the STM has proven to be a powerful tool for studying conducting materials such as superconductors [1, 2, 3], semi-conductors [4] and charge density wave conductors [5, 6].

An STM works by placing an atomically sharp tip microscopically close to the sample of interest. If the tip is close enough to the sample and a voltage bias is applied between the two, electrons will be able to jump or “tunnel” between the tip and sample. Since the tunneling current has a dependence on physical parameters such as tip-sample separation, bias voltage, temperature, the work function of the materials and the density of states of the tip and sample, numerous experiments on the atomic scale can be performed with an STM. The powerful abilities of an STM include being able to produce topographic images with ultra high sensitivity of sample surfaces. For many materials, atomic structure can be viewed in real space images. It also can probe the position dependence of the electronic structure of a material. This includes measurements of the density of states which provides the number of states per unit energy and a measurement of the work function of the sample. In addition, surfaces can be modified by migrating atoms from the sample to the tip and vice versa. This enables lithography on the nano-scale to be performed.

There has been a surprising new class of materials which are insulating in nature but retain a finite electrical resistance even at cryogenic temperatures [7, 8, 9]. Among

these materials is  $\text{Sr}_2\text{IrO}_4$ , which is the prototype of magnetic insulators driven by spin-orbit coupling. The transport properties of this material makes an STM, which requires electrically conducting samples, the ideal tool to investigate its complex electronic properties.

## 2.1 Square Barrier

Tunneling is a phenomenon in which a particle on one side of a potential barrier actually penetrates through the barrier and appears on the other side. To give a classical analogy, consider a baseball pitcher who is attempting to throw a pitch to his catcher. Now suppose that a potential barrier in the form of a brick wall is placed between the two baseball players and the pitcher begins to throw the ball. Our intuition tells us that the baseball will just bounce off the wall no matter how many pitches are thrown. Whether there are hundreds, thousands or even millions of pitches thrown, we would never expect the baseball to penetrate through the brick wall arriving in the catcher's mitt leaving the wall intact. This intuition does not contradict the tunneling phenomenon due to the macroscopic mass of the baseball and thickness of the brick wall. These values will produce a probability of the baseball tunneling through the brick wall that is effectively zero. However, if we enter into the microscopic world by replacing the baseball and brick wall with an electron and a small vacuum gap, the tunneling probability will be small but finite.

Now consider the one dimensional case of an electron with energy  $E$  traveling in the  $+z$  direction incident upon a square potential barrier with a height of  $V_0$  and a width of  $d$  as described by Equation 2.1 and shown in Figure 2.1 a). Upon interacting with the barrier, the electron will either reflect off the barrier and travel in the  $-z$  direction or it will continue traveling in  $+z$  direction by tunneling through the barrier illustrated in Figures 2.1 b) and c) respectively. Even though the majority of electrons will not tunnel through the barrier, there is a finite probability that the



electron will tunnel through the barrier resulting in a tunneling current governed by Eqn. 2.2 [10]. In this equation  $m$  and  $\hbar$  are the mass of the electron and reduced Planck's constant respectively. Even though this is an overly simplified expression for the tunneling current, it does illustrate how the tunneling current has an exponential dependence on the width of the potential barrier. This dependence allows for small changes in the width of the barrier to produce large changes in the tunneling current. For example, changing the barrier width by a factor of two will roughly change the tunneling current by an order of magnitude. This creates a very sensitive technique for measuring microscopic changes in distance between the two tunneling electrodes. Therefore tunneling experiments can be used to acquire topographic images of sample surfaces with ultra high sensitivity. This technique will be discussed in greater detail later.

$$V(z) = \begin{cases} 0 & z < 0 \\ V_0 & 0 \leq z \leq d \\ 0 & z > d \end{cases} \quad (2.1)$$

$$I_{\text{tunnel}} \propto e^{-2d\sqrt{\frac{2m}{\hbar^2}(V_0-E)}} \quad (2.2)$$

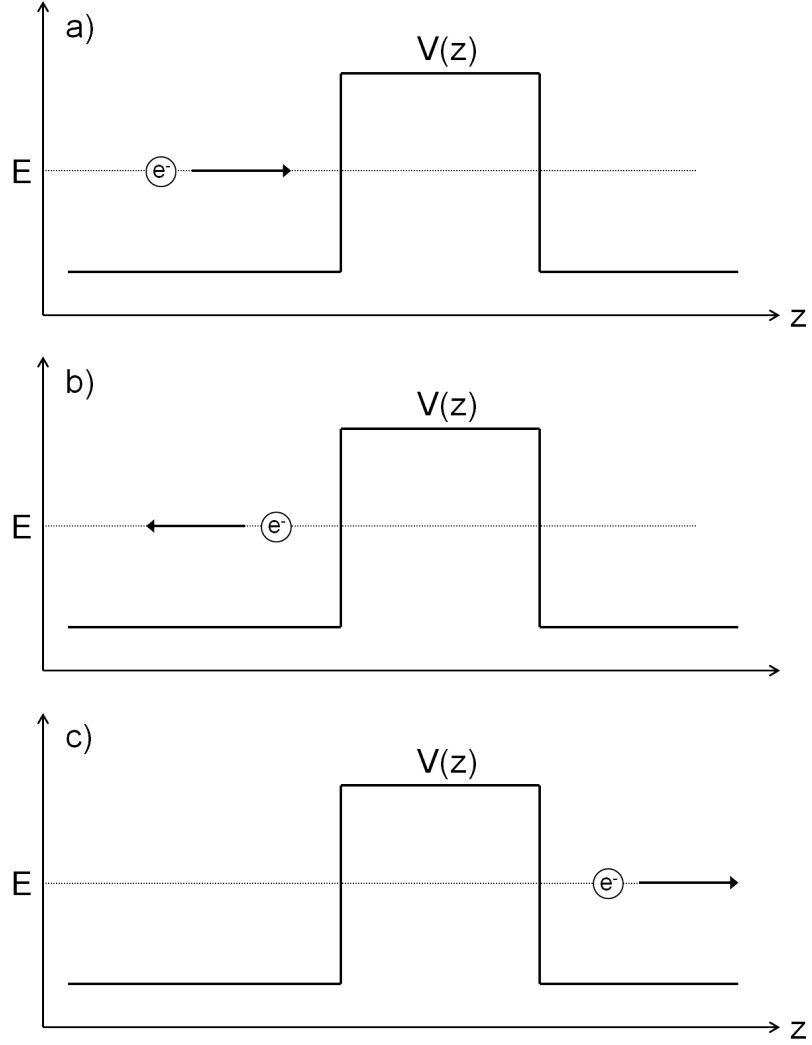


Figure 2.1: a) An electron traveling in the  $+z$ -direction incident upon a square potential barrier. Upon interacting with the barrier the electron will either be b) reflected traveling in the  $-z$ -direction or c) transmitted continuing in the  $+z$ -direction.

## 2.2 Trapezoid Barrier

For real systems, the tunneling barrier will only be square if the work functions of the two tunneling electrodes are identical and there is no bias voltage applied across the tunnel junction. Regardless of the relative magnitudes of the work function of each electrode, when there is no voltage bias across the junction, there will not only be electrons tunneling from left to right as illustrated in Figure 2.1 c), but there will also

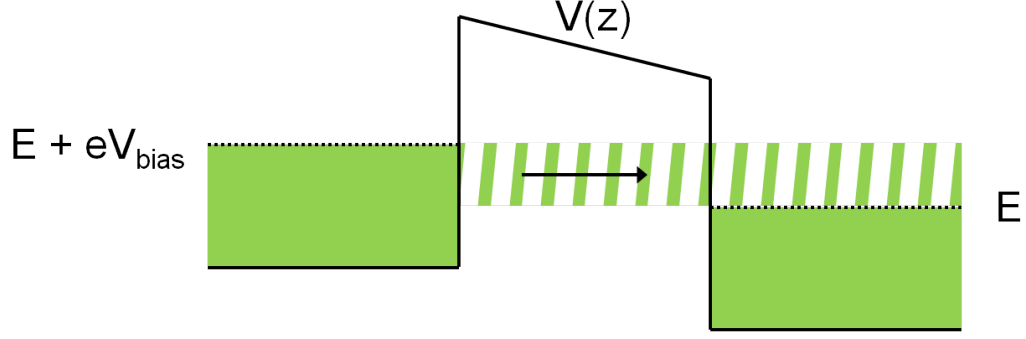


Figure 2.2: When  $V_{\text{bias}}$  is applied it enables electrons with energy between  $E$  and  $E + eV_{\text{bias}}$  to tunnel across the gap. The solid regions are filled states, the striped region is the energy window allowing electron tunneling and the arrow indicates the direction of the tunneling electrons.

be an equal probability that electrons will tunnel from right to left. The competing effects will result in a net tunneling current of zero. In order to obtain a net tunneling current, it is necessary to shift the energy of one of the electrodes by  $eV_{\text{bias}}$ , where  $e$  is the elementary charge constant and  $V_{\text{bias}}$  is the bias voltage applied across the junction. This in turn changes the shape of the potential barrier from a square to a trapezoid as shown in Figure 2.2. This shift raises the energy of all electrons on the left by the same amount now making it energetically favorable for electrons with an energy between  $E$  and  $E + eV_{\text{bias}}$  to collectively tunnel across the barrier. This energy region is represented as stripes in Figure 2.2. It is important to note that  $V_{\text{bias}}$  can be positive allowing electrons to flow from the left filling holes on the right or negative with electrons initially on the right tunneling into holes on the left.

### 2.3 Density of States

The density of states of a material is an expression that relates the number of states present in a given material per unit energy. When a tunnel junction is created with two conducting materials, each side of the junction will have a density of states associated with it. The resulting tunnel current will be related to the density of

states. Since only electrons with an energy between  $E$  and  $E + eV_{\text{bias}}$  will contribute to the measured tunneling current, this current must depend on how many electrons are present in the electrode with the larger energy and the number of holes available in the other electrode in this energy region. Consider the case where one of the tunneling electrodes is a material with an energy gap ( $2\Delta$ ) such as a superconductor. Inside this gap the density of states will vanish. Since there will be neither electrons nor holes to contribute to the tunneling, there will only be a finite tunneling current in the region  $|eV_{\text{bias}}| \gtrsim \Delta$ .

## 2.4 Bardeen Transfer Hamiltonian

Bardeen developed this formalism to explain the results obtained from planar tunnel junctions created by separating superconductors with a thin oxide layer [11]. The shape of the tunnel barrier typically has a shape more complex than the square and trapezoid barriers described above. The power of Bardeen's formalism is it produces an algebraic expression for the tunneling current without knowing the shape of the barrier. Now consider a potential barrier that is an arbitrary function in the region  $r_1 \leq r \leq r_2$  and vanishes elsewhere as shown in Figure 2.3. Bardeen solved this problem by separating it into two regions  $R_1 : r \leq r_2$  and  $R_2 : r \geq r_1$ . Note that both regions include the barrier. Regions 1 and 2 will be governed by the Hamiltonians  $H_1$  and  $H_2$ , respectively. Region 1 will have an eigenstate of  $\phi_0$  and an eigenvalue of  $E_{1,0}$  while region 2 will have an eigenstate of  $\psi_\mu$  and an eigenvalue of  $E_{2,\mu}$ . The Hamiltonians  $H_1$  and  $H_2$  will have the following form [11, 12, 13]:

$$H_1 = -\frac{\hbar^2}{2m}\nabla^2 + V_1(r) \quad ; \quad H_1\phi_0 = E_{1,0}\phi_0 \quad r \in R_1 \quad (2.3)$$

$$H_2 = -\frac{\hbar^2}{2m}\nabla^2 + V_2(r) \quad ; \quad H_2\psi_\mu = E_{2,\mu}\psi_\mu \quad r \in R_2 \quad (2.4)$$

where  $V_1(r)$  and  $V_2(r)$  are the potential  $V(r)$  for the appropriate region. The solutions

$\phi_0$  and  $\psi_\mu$  are well understood to have an oscillatory nature outside the barrier and undergo an exponential decay when inside as illustrated in Figure 2.3. Now the full Hamiltonian ( $H$ ) will be:

$$H = H_1 + H_2 + H_T \quad (2.5)$$

where the first two terms  $H_1$  and  $H_2$  are known and described above. However the third term  $H_T$  is the Bardeen Transfer Hamiltonian and is not known. Therefore it is assumed that the width of the barrier is relatively large allowing for the following approximation:

$$H \sim H' = \begin{cases} H_1 & r \in R_1 \\ H_2 & r \in R_2 \end{cases} \quad (2.6)$$

To illustrate the validity of this assumption, the wave functions  $\phi_0$  and  $\psi_\mu$  were extended into the regions where they are not valid in Figure 2.3. In these regions the two wave functions are approximately zero minimizing their contribution to the total Hamiltonian.

Using time-dependent perturbation theory the total wave function will be.

$$\Psi(r, t) = a_0(t)\phi_0(r)e^{-iE_{1,0}t/\hbar} + \sum_{\mu} b_{\mu}(t)\psi_{\mu}(r)e^{-iE_{2,\mu}t/\hbar} \quad (2.7)$$

Fermi's Golden Rule can be implemented in order to calculate the probability of an electron tunneling through the barrier.

$$P = \frac{2\pi}{\hbar} \sum_{\mu} |M|^2 \delta(E_{2,\mu} - E_{1,0}) \quad (2.8)$$

where the transition or tunneling probability matrix ( $M$ ) is:

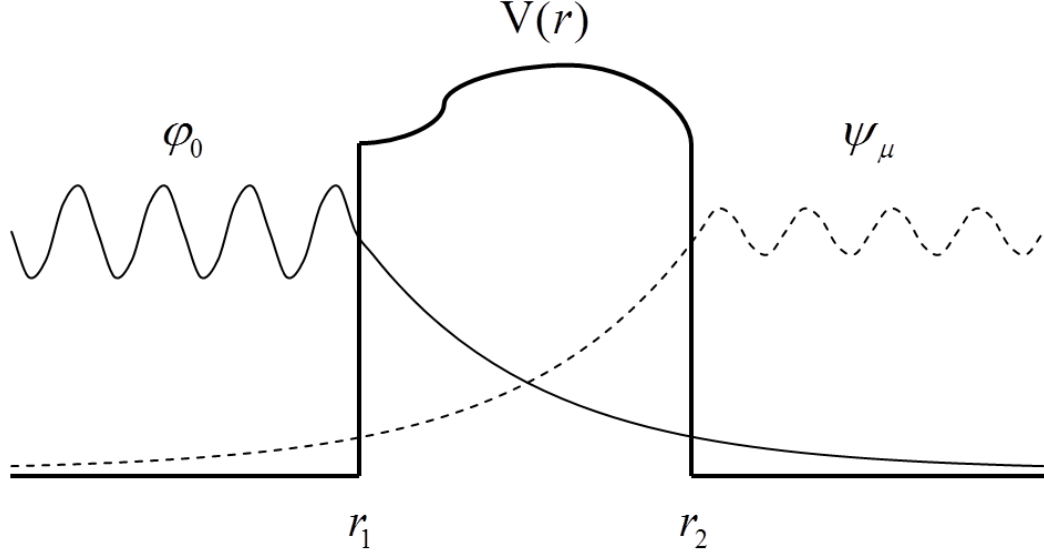


Figure 2.3: An arbitrary potential barrier ( $V(r)$ ) with wave functions for  $H_1$  and  $H_2$  represented as solid and dotted lines respectively.

$$M = \langle \psi_\mu | H_2 + H_T | \phi_0 \rangle \quad (2.9)$$

$$= \langle \psi_\mu | H - H_1 | \phi_0 \rangle \quad (2.10)$$

$$= \int_{-\infty}^{\infty} \psi_\mu^* (H - H_1) \phi_0 dV \quad (2.11)$$

$$\approx \int_{-\infty}^{\infty} \psi_\mu^* (H' - H_1) \phi_0 dV \quad (2.12)$$

$$= \int_{R_2} \psi_\mu^* (H' - H_1) \phi_0 dV \quad (2.13)$$

In the region  $R_2$ ,  $H' - H_2 = 0$  allowing for  $M$  to be expressed symmetrically as follows:

$$M = \int_{R_2} \psi_\mu^* (H' - H_1) \phi_0 - \phi_0 (H' - H_2) \psi_\mu^* dV \quad (2.14)$$

$$= \int_{R_2} \psi_\mu^* H' \phi_0 - \psi_\mu^* H_1 \phi_0 - \phi_0 H' \psi_\mu^* + \phi_0 H_2 \psi_\mu^* dV \quad (2.15)$$

$$= \int_{R_2} \psi_\mu^* H' \phi_0 - \psi_\mu^* E_{1,0} \phi_0 - \phi_0 H' \psi_\mu^* + \phi_0 E_{2,\mu} \psi_\mu^* dV \quad (2.16)$$

Now we will as assume elastic tunneling which implies that  $E_{1,0} = E_{2,\mu}$ . Utilizing Equations 2.3 and 2.6, the tunneling probability matrix will reduce to:

$$\begin{aligned} M &= \int_{R_2} \psi_\mu^* H' \phi_0 - \phi_0 H' \psi_\mu^* dV \\ &= \int_{R_2} \psi_\mu^* H_2 \phi_0 - \phi_0 H_2 \psi_\mu^* dV \end{aligned} \quad (2.17)$$

$$= \int_{R_2} \psi_\mu^* \left( -\frac{\hbar^2}{2m} \nabla^2 + V_2(r) \right) \phi_0 - \phi_0 \left( -\frac{\hbar^2}{2m} \nabla^2 + V_2(r) \right) \psi_\mu^* dV \quad (2.18)$$

$$= \frac{\hbar^2}{2m} \int_{R_2} \phi_0 \nabla^2 \psi_\mu^* - \psi_\mu^* \nabla^2 \phi_0 dV \quad (2.19)$$

Recall Green's second theorem:

$$\int_S (f \nabla g - g \nabla f) dS = \int_V (f \nabla^2 g - g \nabla^2 f) dV \quad (2.20)$$

Utilizing this, the transfer matrix will become:

$$M = \frac{\hbar^2}{2m} \int_{S_{R_2}} (\phi_0 \nabla \psi_\mu^* - \psi_\mu^* \nabla \phi_0) dS \quad (2.21)$$

Inserting this into Equation 2.8 and summing over all allowed states will result in the following expression for the tunneling current:

$$I = \frac{4\pi e}{\hbar} \int_{-\infty}^{\infty} [f(E_F - eV + \epsilon) - f(E_F + \epsilon)] \rho_S(E_F - eV + \epsilon) \rho_T(E_F + \epsilon) |M|^2 d\epsilon \quad (2.22)$$

where  $f(E)$  is the Fermi distribution function,  $\rho_S(E)$  is the density of states of the sample and  $\rho_T(E)$  is the density of states of the tip. The Fermi distrubution function will have the following form:

$$f(E) = \frac{1}{1 + e^{E/K_B T}} \quad (2.23)$$

The tunneling current's exponential dependence on the tip sample separation expressed in Equation 2.2 can be found in  $M$ . At zero temperature the first term of

the integrand which is a difference of two Fermi distribution functions will be unity for  $0 < \epsilon < eV$  and zero otherwise. This will simplify the expression for the tunneling current to:

$$I = \frac{4\pi e}{\hbar} \int_0^{eV} \rho_S(E_F - eV + \epsilon) \rho_T(E_F + \epsilon) |M|^2 d\epsilon \quad (2.24)$$

The validity of this assumption can be seen in Figure 2.4 where the term  $f(\epsilon - eV) - f(\epsilon)$  is plotted versus energy in electron volts for temperatures of 4.2 K, 77 K, 300 K and 500 K. Notice that the red curve that is simulated for a temperature of  $T = 4.2$  K consists of two very sharp steps at  $E = 0$  and  $E = eV$  making this a good assumption at this temperature. As temperature is increased, the steps become smoothed over. This effect is commonly referred to as thermal smearing. The inset is merely a magnification of one of the shoulders. This dependence of the tunnel current on temperature results in a limiting energy resolution of  $\Delta\epsilon \approx 3.5k_B T$  in tunneling experiments. Values of this limiting resolution for temperatures commonly used for tunneling experiments can be seen in Table 2.1.

In addition, if the density of states of the tip and the tunneling probability are assumed to be independent of the bias voltage, at zero temperature the tunneling current will reduce to:

$$I \propto \int_0^{eV} \rho_S(E_F - eV + \epsilon) d\epsilon \quad (2.25)$$

which will result in:

$$\rho_S(E) \propto \frac{dI}{dV} \quad (2.26)$$

This simple expression relates the density of states of the sample directly to the tunneling current. Assuming that  $M$  is constant may not be a great assumption. However in most cases it varies smoothly with respect to the bias voltage allowing features of the sample density of states to be observed in the tunneling spectroscopy.



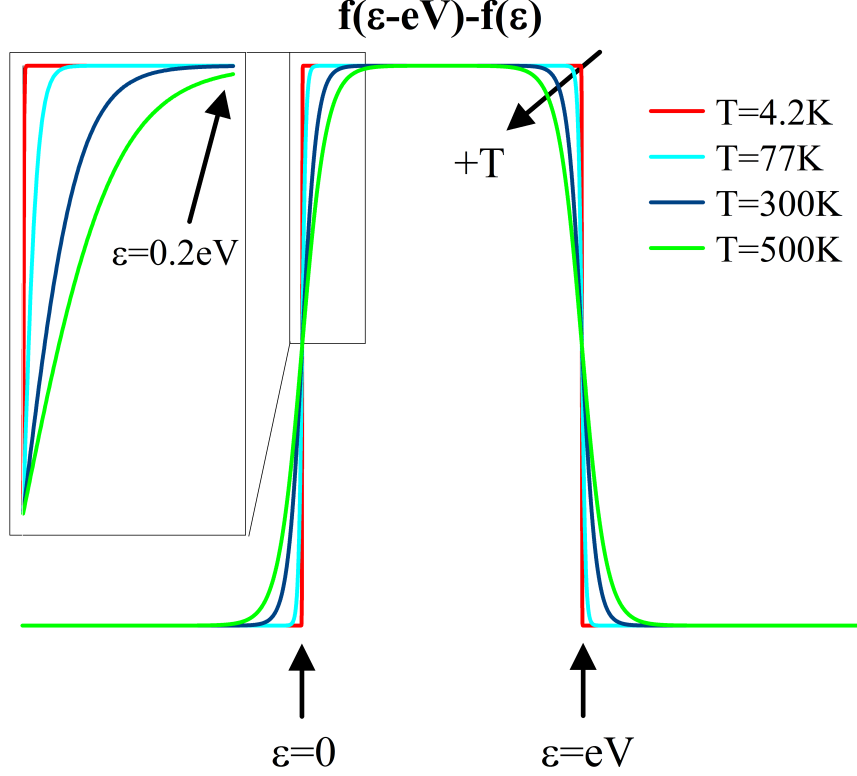


Figure 2.4: Plots of  $f(E_F - eV + \epsilon) - f(E_F + \epsilon)$  where  $E = E_F + \epsilon$  for several temperatures.

The expression for the derivative of the tunneling current found in Equation 2.26 is a zeroth order approximation. In order to account for the thermal effects due to tunneling measurements obtained at finite temperature Equation 2.22 can be differentiated to obtain [14]:

$$\frac{dI}{dV} \propto \int_{-\infty}^{\infty} d\epsilon \frac{\rho_S(\epsilon)}{\rho_S(0)} \left[ -\frac{\partial f(\epsilon + eV)}{\partial eV} \right] \quad (2.27)$$

Even though this expression better represents tunneling, it is inconvenient due to its integral dependence on the density of states. It is very challenging if not impossible to deconvolute the density of states from this expression. Its main function is to obtain parameters when the functional form of the DOS is known. For example, the BCS theory for superconductivity predicts a DOS of the form  $|\epsilon|/\sqrt{\epsilon^2 - \Delta^2}$ . Therefore tunneling data obtained on this class of materials can be fitted to Equation 2.27 in

T (K)	$\Delta\epsilon = 3.5_B T$ (meV)
300	90
77	23
4.2	1.3

Table 2.1: Energy resolution  $\Delta\epsilon$  for common temperatures.

order to determine the gap parameter ( $\Delta$ ).

## Chapter 3 Scanning Tunneling Microscopy

### 3.1 Introduction

Typically tunneling experiments are performed through planar junctions or with a scanning tunneling microscope (STM). Planar junctions consist of a thin insulator sandwiched in between two electrically conducting materials. This type of barrier has great mechanical stability but has no spatial resolution. An STM creates a tunnel junction by placing an ultra-sharp tip atomically close ( $\sim 10 \text{ \AA}$ ) to the sample of interest. In this case, the tip can be displaced microscopic distances in three dimension enabling microscopic images and work function measurements to be acquired. All the tunneling results described below were obtained with a home built STM. Since the tunnel current will depend on the density of states of both the tip and sample, it is often convenient to choose a tip made of a material with a relatively constant density of states. Tips made of good metals such as gold, tungsten, platinum or platinum-iridium typically satisfy this condition.

### 3.2 STM Scanner

In order to achieve microscopic motion of the tip a scanner built with piezoelectric actuators is utilized. To minimize the size of our STMs all scanners are built with a single piezoelectric tube. The tube has nickel electrodes on both the inside and outside. The outer electrode is broken into equal quadrants with four axial cuts. It then has a radial cut near the center of the tube. Four of the electrodes on one side of the radial cut are electrically shorted to each other. This section of the tube will be responsible for fine motion of the STM tip in the z-direction. The z-axis is parallel to the axis of symmetry of the tube and the tip of the STM. Deflections along the z-axis

will be governed by Equation 3.1 where  $V$  is the voltage applied to the electrode,  $L_z$  is the length between the radial cut and the end of the tube responsible for z motion,  $t$  is the wall thickness of the tube and  $d_{31}$  is an element of the piezo strain matrix. The  $d_{31}$  term relates the mechanical deflection of the piezoelectric elements to the applied electric field. The values of  $d_{31}$  for the three types of piezoelectric materials we use can be found in Table 3.1. The negative sign implies that a positive voltage applied to the outer electrode will result in a contraction of the overall length of this section of the tube. The other half of the tube will be responsible for fine motion in the xy-plane, which will be the plane parallel to the sample surface of interest. Whenever a voltage  $V_x$  is applied to one of the four electrodes and a voltage  $-V_x$  is applied to the electrode opposite to it the end of the tube will be displaced along the x-axis by an amount found in Equation 3.2, where  $L_{xy}$  is the length of the portion of the tube responsible for motion in the xy-plane, OD is the outer diameter of the tube and ID is the inner diameter of the tube. Similarly motion in the y-direction can be achieved by applying voltages  $V_y$  and  $-V_y$  to the remaining two electrodes. With an STM scanner with an outer diameter, wall thickness and total length of 3.18 mm, 0.51 mm and 12.7 mm respectively, independent motion in all three dimensions can be achieved with a maximum deflection on the order of a few hundred nanometers.

$$\Delta L_z = \frac{d_{31}VL_z}{t} \quad (3.1)$$

$$\Delta L_{xy} = \frac{1.8d_{31}VL_{xy}^2}{(OD + ID)t} \quad (3.2)$$

EBL	PZT	$d_{31}$ ( $\text{\AA}/\text{V}$ )
2	5A	-1.73
3	5H	-2.62
4	8	-0.95

Table 3.1: Names of piezoelectric materials used with  $d_{31}$  values.

### 3.3 Coarse Approach

Recall that in order to achieve tunneling conditions the STM tip must be  $\sim 10 \text{ \AA}$  from the sample and the scanner is capable of displacing the tip  $\sim 1000 \text{ \AA}$  along the z-axis. Therefore it is necessary to have a mechanism to get the scanner close enough to the sample that electrons can tunnel across the barrier. This rough motion is called the coarse approach and it is also achieved with piezoelectric actuation. Our STMs utilize slip-stick motion based upon the design of Shuheng Pan [15, 16]. The piezoelectric materials are plates with a shear mode polarization. This implies that the piezoelectric crystals were polarized in a direction that is orthogonal to the direction of the applied electric field. These materials are oriented so that the shear motion is in the z-direction. Since the amount of deflection of a piezoelectric material is proportional to the applied electric field, the deflection of these shear mode plates will be independent of the thickness of the plate. Therefore the amplitude of the deflection will be proportional to the applied voltage. So in order to achieve larger displacements for a given voltage, four plates are stacked together to create a single walker leg. A total of six legs are necessary to achieve this orchestrated coarse motion.

An optically polished alumina oxide plate is attached to the top of each walker leg. The coarse motion consists of these six walker legs translating a triangular sapphire prism along the z-axis. The prism and alumina plates form a hard smooth frictional interface necessary for slip-stick motion. Since this type of motion is coupled to friction, it is necessary to apply an appropriate normal force. If the associated

frictional force is too small, each leg will slip forward and backward yielding no net motion. Similarly if the force is too large, the walker legs will clamp down on the sapphire prism completely constricting motion. However there will be a range of frictional forces ( $\sim 1 - 2$  N) that will allow collective motion along the z-axis [17].

Motion is obtained by rapidly applying a voltage to one of the walker legs. The quick pulse allows the leg to easily break the static friction and move a small distance in the opposite direction of the desired motion. This motion is relative to the sapphire prism and the other walker legs. This is repeated one by one to each of the five remaining walker legs. Once each leg is in this stressed state by application of the high voltage transients, the voltage will be slowly removed from all six walker legs simultaneously. As this occurs the sapphire prism will be displaced a small amount in the desired direction of motion. The scanner is rigidly attached to the sapphire prism as illustrated in Figure 3.1. Therefore displacing the prism towards the sample will bring the STM tip closer to the sample.

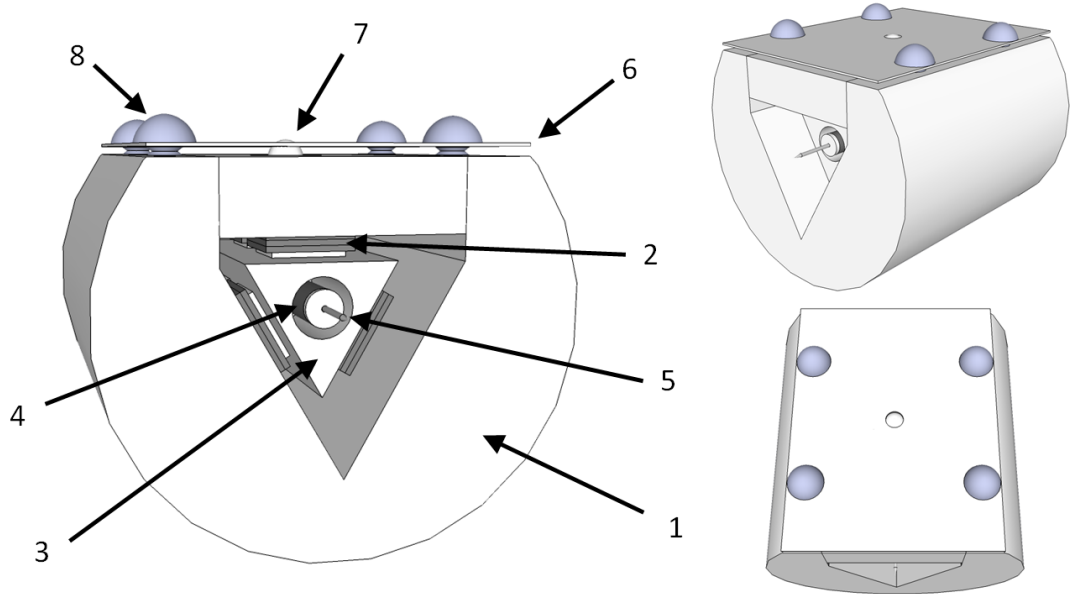


Figure 3.1: Illustration of STM with 1) the Macor body, 2) one of six walker legs, 3) the sapphire prism, 4) the scanner and 5) the STM tip, 6) the beryllium copper plate, 7) the sapphire ball and 8) the nylon screws.

### 3.4 STM Assembly

The stacks are attached to a two-piece body made of Macor. Macor is a machinable ceramic that remains dimensionally stable in a large temperature range including room temperature and cryogenic temperatures. These two pieces are held together with a beryllium copper plate and a sapphire ball as shown in Figure 3.1. The thickness of the copper plate is carefully chosen so that the spring force generated by attaching it to the first Macor piece is applied through the sapphire ball to the other Macor piece resulting in optimal frictional forces between the sapphire prism and the alumina plates. This friction is sufficient for the STM to be operated in either a vertical or horizontal configuration.

In our setup, the tunneling current is measured through the STM tip. This signal is sent to an amplifier with a gain of  $10^7 - 10^9$ . This large gain coupled to the close proximity of the tip to the high voltages necessary for the scanner and walker legs make careful shielding of the signal wire between the tip and the input of this amplifier extremely important. The tip holder consists of two concentric stainless steel cylinders electrically insulated from each other with Torr-Seal brand epoxy. Electrical contact to each stainless steel cylinder is made by soldering a short 250  $\mu\text{m}$  diameter wire to it with an indium doped lead-tin solder. Since the tip must be mechanically free to move, the wire attached directly to the tip must have weak mechanical coupling between the STM tip and the STM body. Most commercially available coaxial wires are too stiff to satisfy this condition. This makes it necessary to create one by using 75  $\mu\text{m}$  diameter wire. This wire is used to make a helix with inner diameter of 500  $\mu\text{m}$  which will be the shielding. A similar wire is inserted into the helix to serve as the center conductor. One end of this wire is soldered to the tip holder with indium and the other is conventionally soldered to pins attached to the STM body with lead/tin solder. The signal can then be run from the STM body to

the first stage amplifier with a commercially available coaxial cable.

The amplifier is a current-to-voltage converter as illustrated in Figure 3.2. This results in the STM tip being held at a virtual ground. In this circuit the output voltage will be proportional to the input current as shown in Equation 3.3. If  $R_{\text{sense}} = 10 \text{ M}\Omega$ , the output of the circuit will be  $-10 \frac{\text{mV}}{\text{nA}}$ . The small capacitor in parallel with the sense resistor is to eliminate transients in the output voltage. If the sense resistor is changed, this capacitor must also be changed such that the RC time constant remains constant. The two  $0.01 \text{ }\mu\text{F}$  capacitors are in place to eliminate 60 Hz noise in the voltage supplies. Care must be taken to choose an amplifier with an input bias current that is much smaller than the desired tunneling current. Otherwise the tunnel current will pass through the input of the amplifier and will not be measured. The output signal of this amplifier is then fed to another amplifier with a gain of 10 and then into our commercial STM electronics (RHK STM-100). These electronics are automated with a computer enabling high speed acquisition of microscopic and spectroscopic data. The sample will then be mounted in front of the STM such that the STM tip is aligned with the sample. The bias voltage will be applied to the sample. With this configuration, a positive bias will enable electrons in the tip to tunnel into empty states in the sample. So once the coarse approach and the scanner get the tip close enough to the sample so that tunneling is allowed, the tunneling current will be measured with this circuit.

$$V_{\text{out}} = -R_{\text{sense}} \times I_{\text{tunnel}} \quad (3.3)$$



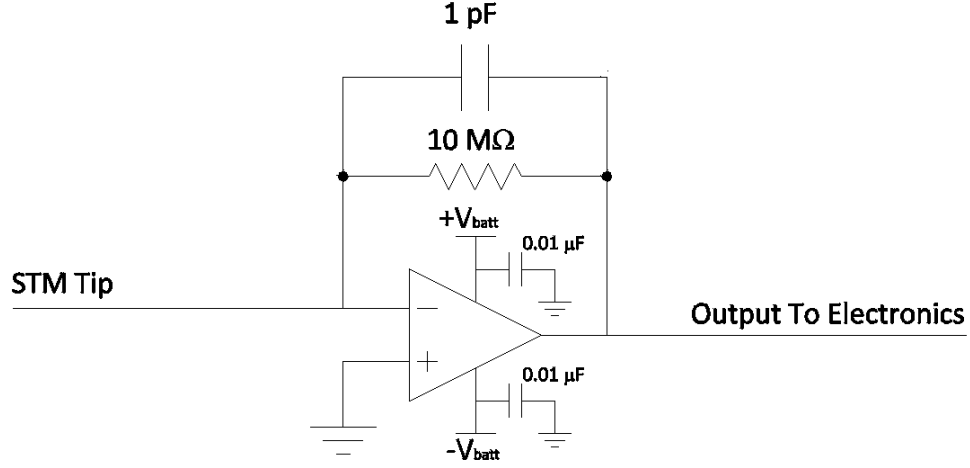


Figure 3.2: First stage amplifier with output  $V_{\text{out}} = -(10 \text{ M}\Omega)I_{\text{tunnel}}$ .

### 3.5 Imaging

Scanning tunneling microscopy is a technique which requires the tip to be within tunneling range. The tip will then undergo a raster scan of the sample surface allowing microscopic images of the sample surface to be obtained. This can be accomplished by applying a fast triangle waveform ( $T = 0.1 - 5 \text{ s}$ ) to the electrodes which provide motion in the x-direction while simultaneously applying a slow triangle waveform ( $T = 2 - 30 \text{ min}$ ) to the electrodes which provide motion in the y-direction, where  $T$  is the period of the waveform. Note that it only takes half a period of the slow triangle waveform to acquire a full image. The scan direction can be flipped by applying the fast waveform to the y-axis electrodes and the slow waveform to the x-axis electrodes. Applying these waveforms to the scanner, translates the tip over an approximately rectangular area of the sample. Equation 3.2 shows that the size of the scan area will be set by the amplitude of the applied triangle waveforms. Often the amplitudes are identical which results in a square scan area. The commercial

electronics allow for different types of data to be collected. The position dependence of different combinations of the tunneling current, voltage applied to the z-piezo, the input from external lock-in amplifier or an arbitrary analog voltage can be acquired and presented as an image.

There are two common imaging modes that can be utilized: constant height and constant current. In constant height mode, the apex of the tip moves in a plane above the sample surface. As it undergoes a raster scan of this surface, the position dependence of the tunneling current is recorded. Since the tunneling current has an exponential dependence on tip-sample separation as seen in Equation 2.2, the regions in the image with a larger tunneling current will be closer to the tip than regions with a smaller current. Since STM images are given a false color grey scale, the convention used is the light regions represent features that are closer to the viewer and the dark regions are further from the viewer. Constant height images can typically be acquired in  $\sim 1 - 3$  minutes. The main limitation of this mode is that it can only be utilized on very smooth surfaces. For example the typical tip-sample separation is  $\sim 10$  Å. If the average surface roughness of the sample is of this order or larger, the probability of the STM tip crashing into to sample surface is high. A crash occurs when there are strong mechanical interactions between the tip and sample. This typically makes the STM tip more blunt and destroys that portion of the sample. Even though there are *in situ* tip treatment techniques that can restore the integrity of a crashed tip [12], they are often unsuccessful. Since crashing an STM tip into the sample is often catastrophic to the experiment, this technique is typically not utilized until the sample surface of interest has proven to be atomically smooth.

To allow for relatively rougher samples to be measured, the constant current technique must be utilized. A control loop must be implemented that maintains the tunneling current at a user defined setpoint. The output of this control loop changes the voltage applied to the z-piezo so that the tunneling current remains equal to the

setpoint. If the actual tunneling current is smaller than the setpoint, the feedback loop will drive the STM tip closer to the sample until it is equivalent to the setpoint. Similarly if the current is too large, the control loop will withdraw the tip from the sample. Typically in this mode of operation the voltage applied to the z-piezo is recorded and since the displacement in the z-direction is proportional to this voltage (Equation 3.1), it will represent the surface topography. The main disadvantage of this method is it takes a finite amount of time for the control loop to respond, resulting in longer image acquisition times of  $\sim 10 - 15$  minutes.

To this point the emphasis of scanning tunneling microscopy was producing high resolution topographical images of the sample surface. However some materials have a position dependent local density of states (LDOS). Typically this position dependence is commensurate with the underlying atomic lattice. For such materials, the acquired STM images will not purely represent the surface topography. Recall from Equation 2.24 that the tunneling current is a convolution of the surface topography and the LDOS. An example of such behavior can be viewed in Figure 3.3. This image represents a  $0.92 \times 0.92 \text{ nm}^2$  area of a freshly cleaved surface of highly oriented pyrolytic graphite (HOPG) obtained with an electrically etched tungsten tip. The image is a constant current image obtained with a bias voltage of  $V_{\text{bias}} = 1.0 \text{ V}$  and a setpoint tunneling current of  $I_{\text{set}} = 100 \text{ pA}$ . Each white circle in the image represents a single carbon atom on the surface in an apparent trigonal structure. The distance between two adjacent dots in the image is  $2.56 \text{ \AA}$ . However the crystal structure of HOPG has been reported to be a layered honeycomb lattice with a lattice spacing of  $1.42 \text{ \AA}$  [18]. A honeycomb lattice has a hexagonal shape with no atoms in the center of each hexagon. A single yellow hexagonal cell with the appropriate spacing is placed in Figure 3.3. Notice that three points of the hexagon align with the structure of the image while the remaining corners do not. The reason for this behavior is due to the bulk crystal structure which consists of identical layers of carbon atoms in a honey-

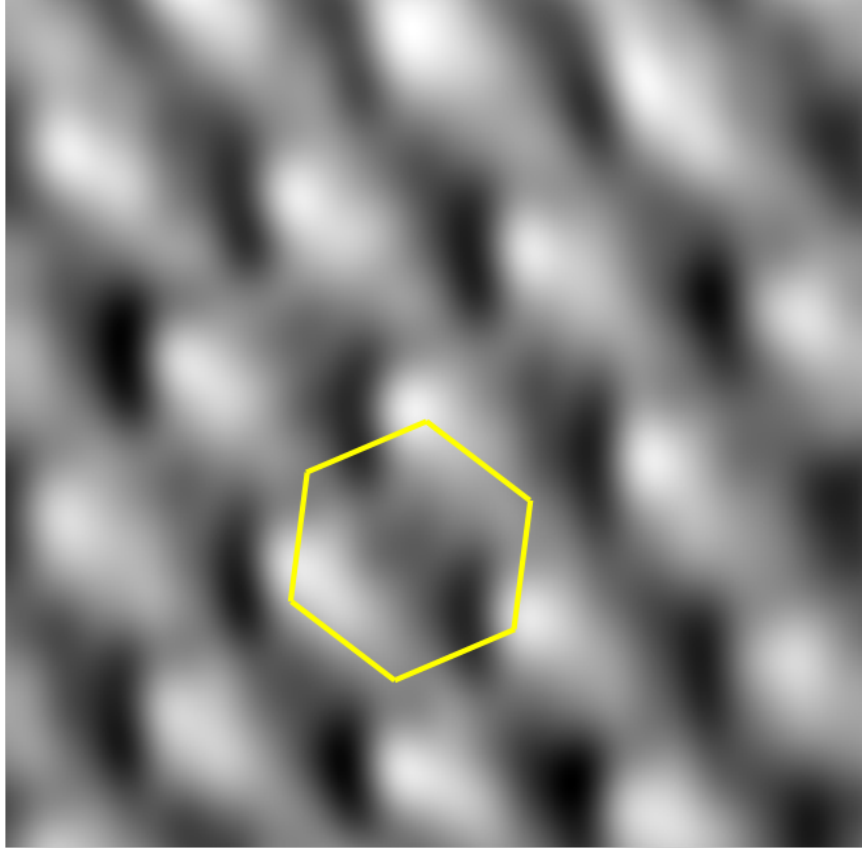


Figure 3.3: Constant current image with atomic resolution of HOPG surface obtained with  $V_{\text{bias}} = 1.0$  V and  $I_{\text{set}} = 100$  pA. The yellow hexagon displays a single honeycomb cell of its crystal structure.

comb lattice. Adjacent layers are staggered such that half the atoms on the surface have a carbon atom from the second layer directly underneath it and the remaining surface atoms do not. This causes the electron density to be much larger near the atoms with an adjacent atom from the second layer. Therefore the periodic atomic structure observed in Figure 3.3 is better described as the position dependence of the density of states rather than the topography.

### 3.6 Spectroscopy

One of the most powerful features of an STM is its ability to directly probe the electronic properties of a material. This type of measurement is more specifically

referred to as scanning tunneling spectroscopy (STS). Even though it is impossible to acquire STM images that are independent of the LDOS, it is possible to acquire spectroscopic data that is independent of tip-sample separation. Equation 2.26 shows to a zeroth order approximation that the LDOS of the sample in an STM experiment will be proportional to the voltage derivative of the tunneling current ( $dI/dV$ ). This term is commonly referred to as the differential tunneling conductance and can be obtained by sweeping the bias voltage through some voltage window. As the bias voltage is swept, the corresponding tunneling current will also be recorded. The differential conductance can be obtained either by numerical differentiation afterwards or simultaneously through modulation techniques. Typically the latter is used because it generally has a better signal to noise ratio and no data processing is necessary to acquire it. For this method, a small ac-voltage ( $\delta V \ll V_{\text{bias}}$ ) is summed with the bias voltage ( $V_{\text{bias}} \rightarrow V_{\text{bias}} + \delta V$ ). This modulation in the bias voltage will in turn modulate the tunneling current by  $\delta I$ . By the mathematical definition of the derivative and Equation 2.26 the LDOS of the sample can be found by keeping the independent variable  $\delta V$  constant and measuring the amplitude of  $\delta I$  with a lock-in amplifier. Therefore, Equations 3.4 and 3.5 show that the output of the lock-in amplifier ( $\delta I$ ) will be proportional to the LDOS of the sample. The lock-in amplifier used is a Model SR830 from Stanford Research Systems.

$$\frac{\delta I}{\delta V} = \frac{dI}{dV} = \rho_S(E) \quad (3.4)$$

$$\rho_S(E) \propto \delta I \quad (3.5)$$

To help illustrate how the tunneling current depends on the density of states, consider Figure 3.4. In it there is an arbitrary sample LDOS with a small gap near the Fermi energy and a constant tip DOS for three different bias voltages. The shaded regions represent filled states in the system. The picture on the left has  $V_{\text{bias}} = 0$ .

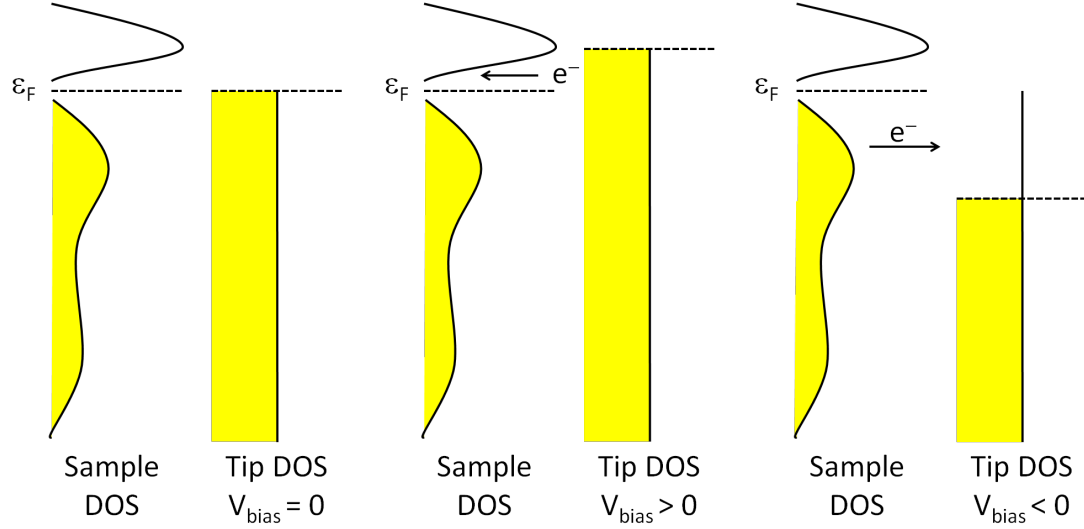


Figure 3.4: Three illustrations of the flow of electrons between tip and sample with arbitrary sample LDOS and constant tip LDOS. (left)  $V_{\text{bias}} = 0$  so no electrons will tunnel. (middle)  $V_{\text{bias}} > 0$  so electrons in the tip will tunnel into empty states in the sample. (right)  $V_{\text{bias}} < 0$  so electrons in the sample will tunnel into empty states in the tip.

This results in the tip and sample having the same Fermi energy resulting in no collective tunneling. Assuming the gap has a full width  $2\Delta$  centered at the Fermi energy, there will continue to be no tunneling current so long as  $|V_{\text{bias}}| < \Delta$ . If  $V_{\text{bias}}$  is increased to a positive value greater than  $\Delta$ , it will become energetically favorable for electrons in the tip to tunnel into empty states in the sample. Therefore as  $V_{\text{bias}}$  increases, the number of electrons tunneling across the barrier must either increase or remain constant. Similarly one can see in the image on the right that electrons will flow from the sample into empty states in the tip if  $V_{\text{bias}} < -\Delta$ .

## Chapter 4 Background of $\text{Sr}_2\text{IrO}_4$

Transition metal oxides (TMOs) have proven to be incredibly interesting due to their exotic properties such as magnetic ordering, high- $T_C$  superconductivity, charge and spin density waves, metal-to-insulator transitions and colossal magnetoresistance. A material that has proven to be exceptionally interesting is  $\text{Sr}_2\text{IrO}_4$ . It is a  $5d$  TMO which was expected to be metallic due a smaller on-site Coulomb interaction compared to its  $3d$  and  $4d$  counterparts. However  $\text{Sr}_2\text{IrO}_4$  and several other  $5d$  TMOs actually have an insulating ground state. This unexpected behavior is due to an appreciable spin-orbit coupling (SOC) interaction and the prototype of this SOC induced Mott insulator is the single layered magnetic insulator  $\text{Sr}_2\text{IrO}_4$ .

### 4.1 Spin-orbit Coupling

Spin-orbit coupling (SOC) is due to the interactions between an electrons spin and the magnetic field generated from its motion. Generally the strength of the SOC interaction scales with atomic number and the effect is often negligible in the lighter elements [19]. SOC will have an interaction strength related to  $\vec{\mu} \cdot \vec{B}$  where  $\vec{\mu}$  is the magnetic moment and  $\vec{B}$  is the magnetic field. A consequence of SOC is it removes degeneracy by splitting electron orbitals and is a mechanism for the fine structure observed in the hydrogen atom [20]. For example, the  $n = 2$  orbital of the hydrogen atom in the absence of SOC and relativistic effects will have a three fold degeneracy of the  $^2P_{3/2}$ ,  $^2P_{1/2}$  and  $^2S_{1/2}$  states. However, SOC will remove this degeneracy making the  $^2P_{3/2}$  state the most highly energetic and the  $^2P_{1/2}$  the least energetic [10]. The effects of SOC on  $\text{Sr}_2\text{IrO}_4$  is illustrated in Figure 4.4.

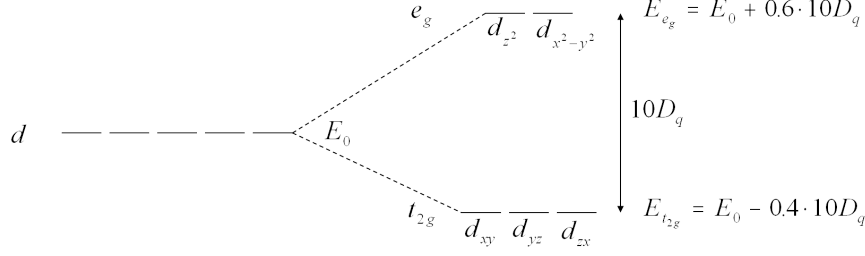


Figure 4.1: Effects of octahedral crystal field splitting on the d-orbital.

## 4.2 Crystal Field Splitting

Crystal field splitting is a phenomenon in which the electron shells experience a large inhomogeneous electric field due to the neighboring ions. This results in a splitting of the orbitals. The inhomogeneity of the electric field is strongly coupled to the crystal lattice of the material. Since  $\text{Sr}_2\text{IrO}_4$  undergoes octahedral crystal field splitting, I will focus on this geometry. The effects due to crystal fields on the d-orbital is illustrated in Figure 4.1. The  $d_{z^2}$  and  $d_{x^2-y^2}$  bands are closer to the neighboring ions than the other  $d$  bands resulting in stronger interactions due to the field. This leads to splitting of the d-orbital with these two bands forming the  $e_g$  band which is higher in energy. Conversely, the  $d_{xy}$ ,  $d_{yz}$  and  $d_{zx}$  bands form the  $t_{2g}$  band which is lower in energy. These two bands are separated by an energy of  $10D_q$ . Assuming the d-orbital originally had an energy of  $E_0$ , the  $t_{2g}$  and  $e_g$  bands will have energies of  $E_0 - 0.4 \cdot 10D_q$  and  $E_0 + 0.6 \cdot 10D_q$  respectively [21].

## 4.3 Crystal Structure

$\text{Sr}_2\text{IrO}_4$  is a member of the Ruddlesden-Popper series ( $\text{Sr}_{n+1}\text{Ir}_n\text{O}_{3n+1}$ ) with  $n = 1$  making it a single layered iridate. This material has a perovskite crystal structure similar to that of  $\text{K}_2\text{NiF}_4$  [22] as illustrated in Figure 4.2. A single layer of this material consists of three atomic layers: an  $\text{IrO}_2$  layer sandwiched between two identical  $\text{SrO}$  layers. Each iridium atom and the six adjacent oxygen atoms form an  $\text{IrO}_6$  oc-



tahedra. These octahedra are rotated around the  $c$ -axis by  $\sim 11^\circ$ . This results in a reduced tetragonal structure (space group  $I4_1/acd$ ). A consequence of this rotation is the unit cell is enlarged. The lattice parameters of  $\text{Sr}_2\text{IrO}_4$  measured by neutron scattering are  $a = 5.498 \text{ \AA}$  and  $c = 25.798 \text{ \AA}$  [23].

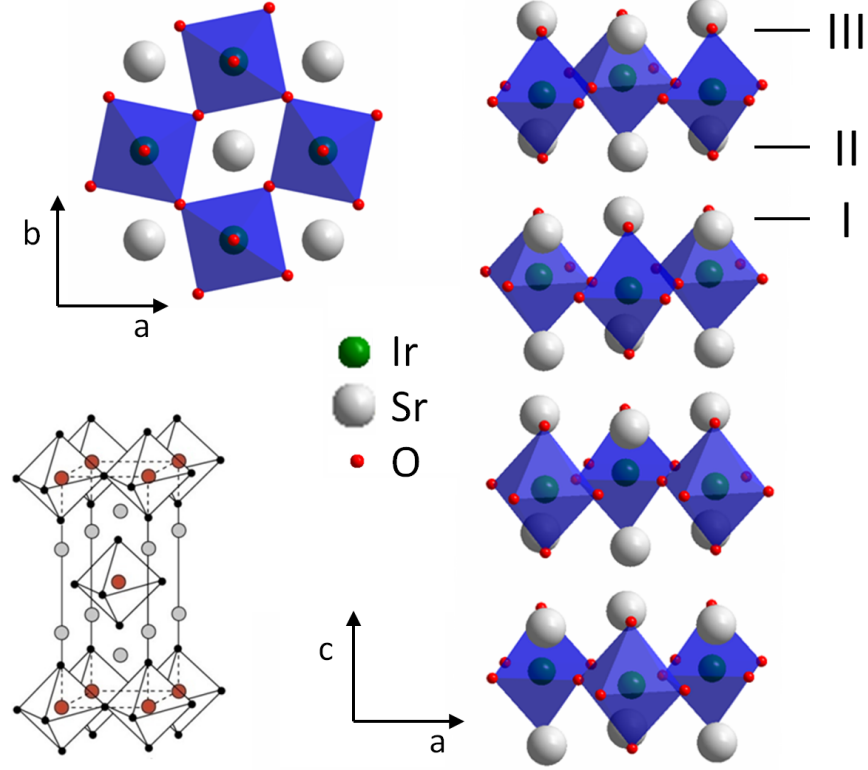


Figure 4.2: The crystal structure of  $\text{Sr}_2\text{IrO}_4$ . (upper left) and (right) The Sr, Ir and O atoms are white, green and red respectively. The  $\text{IrO}_6$  octahedra are colored blue. (upper left) View along  $c$ -axis clearly illustrates rotation of  $\text{IrO}_6$  octahedra. (lower left) The Sr, Ir and O atoms are grey, red and black respectively. The three layers labeled I, II and III are the same as those labeled in Figure 5.5.

The  $\text{IrO}_6$  octahedra coupled to the strontium atoms form a single layer. The octahedra in adjacent layers will be shifted such that the Sr in adjacent layers do not align on top of one another. Both the Ir and Sr atoms in their respective atomic layer form a square lattice. The iridium atoms in adjacent atomic layers will align in the  $ab$ -plane such that they are in the center of the square grid. Also the  $\text{IrO}_6$  octahedra in every second layer will be rotated in the opposite direction. In other words, if the

octahedra in the first two layers are rotated by  $11^\circ$ , then the octahedra in the next two layers will be rotated by  $-11^\circ$ . Note that the distance between two adjacent layers is  $c/4 \sim 7 \text{ \AA}$  and the distance between two adjacent Sr atoms the same atomic layer is  $a/2 \sim 2.5 \text{ \AA}$ .

#### 4.4 Electronic Structure

As one transitions from  $3d$  to  $4d$  and  $5d$  transition metals oxides, the outer electrons become more spatially extended. This results in a smaller on-site Coulomb interaction ( $U$ ) and a larger bandwidth ( $W$ ). This should result in a more metallic behavior. Consider the two material  $\text{Sr}_2\text{CoO}_4$  and  $\text{Sr}_2\text{RhO}_4$  which are respectively the  $3d$  and  $4d$  counterparts of  $\text{Sr}_2\text{IrO}_4$ .  $\text{Sr}_2\text{CoO}_4$  is a ferromagnetic metal [24] while  $\text{Sr}_2\text{RhO}_4$  is an even better metal [25]. Since  $\text{Sr}_2\text{IrO}_4$  has a similar crystal structure and a smaller Coulomb interaction than  $\text{Sr}_2\text{CoO}_4$  and  $\text{Sr}_2\text{RhO}_4$ , it was believed that this single layered iridate would have a simple metallic ground state. It can be clearly seen in Figure 4.3 that this material has an insulating ground state and remains in this state for temperatures as high as 600 K.

As the transition is made from  $3d$  to  $5d$  TMOs, the Coulomb interaction decreases as anticipated. However, the interaction strength of SOC increases to a point where it is no longer negligible relative to  $U$ . Typical values for the on-site Coulomb interaction and the SOC coefficient are displayed in Table 4.1. For typical  $3d$  TMOs, the SOC interaction strength is over an order of magnitude smaller than  $U$ . Therefore the effects in the ground state of  $3d$  TMOs due to SOC are negligible. Since the interaction strengths of  $U$  and SOC are comparable for  $5d$  TMOs such as  $\text{Sr}_2\text{IrO}_4$ , both interactions have appreciable influence on the system.

To illustrate how SOC drives this material into the insulating state consider Figure 4.4. In panel a), there is a single partially filled  $t_{2g}$  band of a good metal whose bands are only split due to crystal fields. Note that the higher energy  $e_g$  band is empty. If a

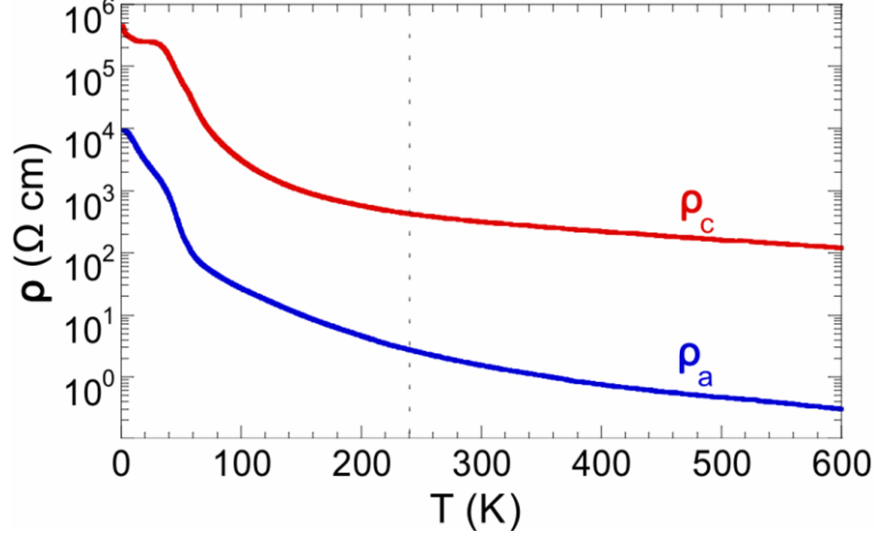


Figure 4.3: Temperature dependence of the electrical transport properties in  $\text{Sr}_2\text{IrO}_4$  measured along the a-axis (blue) and the c-axis (red). [26]

large  $U$  is applied to this material, it will open a Mott gap in the material splitting the valence band into a Lower Hubbard Band (LHB) and an Upper Hubbard Band (UHB) as shown in panel b). This will result in an insulating state, however the value for  $U$  necessary to accomplish this in  $\text{Sr}_2\text{IrO}_4$  is much larger than the  $U$  of approximately 2.0 eV that is observed in this material [28]. Therefore the Coulomb interaction cannot solely be responsible for the insulating behavior observed in  $\text{Sr}_2\text{IrO}_4$ . Panel c) illustrates the metal in the presence of SOC with a negligible  $U$ . The band is split into a  $J_{\text{eff},3/2}$  band which can hold four electrons and a more energetic  $J_{\text{eff},1/2}$  band capable of holding two electrons. Regardless of whether a gap is actually opened, there will be a partially filled valence band resulting in a metallic ground state. However the coexistence of both a realistic  $U$  and SOC can be seen in panel d). Even though  $U$  is not large enough to open a Mott gap in the full  $t_{2g}$  band, it is large enough open one in the  $J_{\text{eff},1/2}$  band. Therefore the  $J_{\text{eff},1/2}$  band is split into a filled LHB and an empty UHB. The opening of this Mott gap in the  $J_{\text{eff},1/2}$  band drives this system into the insulating state. This makes  $\text{Sr}_2\text{IrO}_4$  a SOC driven Mott insulator.

The effects of crystal field splitting and SOC on the electronic bands of  $\text{Sr}_2\text{IrO}_4$

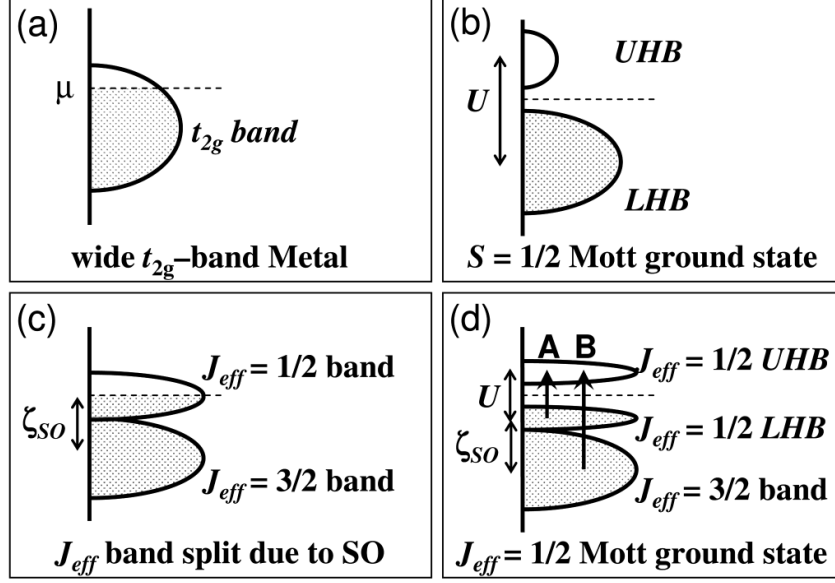


Figure 4.4: a) Band structure of a simple metal. b) Mott gap generated by unrealistically large  $U$ . c) Band splitting due to only SOC results in metallic state. d) Modest  $U$  in presence of SOC results in insulating state. [27]

	$3d$	$5d$
$U$	5-7 eV	1-3 eV
SOC	0.01-0.1 eV	0.1-1 eV

Table 4.1: Comparison of typical values for spin-orbit coupling and Coulomb interactions for  $3d$  and  $5d$  transition metals [29].

can be seen in Figure 4.5. Panel a) illustrates the effects of crystal field splitting and SOC on the  $5d$  band. Crystals fields will open a gap with a full width of  $10Dq$ . The two bands generated by this splitting are the  $t_{2g}$  band and the more energetic  $e_g$  band. Since the the  $t_{2g}$  can hold six electrons and  $Sr_2IrO_4$  has only five valence electrons, its ground state will have an empty  $e_g$  band. The addition of SOC will produce an additional splitting of the  $t_{2g}$  band into a less energetic  $J_{eff,3/2}$  band and a more energetic  $J_{eff,1/2}$  band. Panel b) displays the effects of SOC and the Coulomb interaction on the  $t_{2g}$  band. Notice how the addition of a realistic value of  $U$  will provide an additional splitting of the  $J_{eff,1/2}$  band opening a Mott gap with a full width of  $2\Delta$ . The two bands split from the  $J_{eff,1/2}$  state are the LHB and the more

energetic UHB. The filling of the five valence electrons in the ground state of this system is shown in Figure 4.5 b). Since the Mott gap is opened in the  $J_{\text{eff},1/2}$  band which can hold two electrons both the LHB and the UHB only have the capacity for one electron. Therefore the LHB will be full with the UHB empty producing an insulating ground state. This explains how  $\text{Sr}_2\text{IrO}_4$  can be insulating with an odd number of valence electrons. Note that the Fermi energy will be located between the LHB and the UHB and that the tunneling spectrum presented in Chapter 5 are relative to this energy.

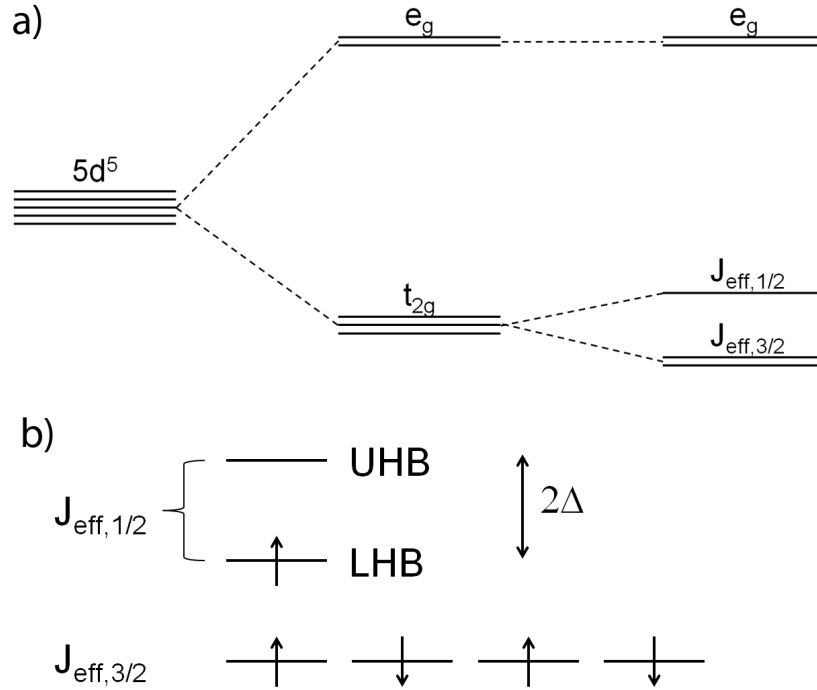


Figure 4.5: a) The effects of the  $5d$  band in  $\text{Sr}_2\text{IrO}_4$  due to crystal field splitting and spin-orbit coupling. b) The effects due to SOC and the on-site Coulomb interaction on the  $t_{2g}$  band.

Spin-orbit coupling inducing an insulating ground state in  $\text{Sr}_2\text{IrO}_4$  has been theoretically confirmed by band structure calculations within the local-density approximation (LDA) of density functional theory [27]. The results of these calculations are

shown in Figure 4.6. Each panel displays the LDA calculations with appropriate interactions on the right with the Fermi surface on the left. Panel a) displays the LDA calculations with no additional interactions which results in a metallic state. Similarly, panel b) which accounts for only SOC and panel d) which accounts for only U also result in a metallic state. However the LDA calculation which accounts for both SOC and U has a gap open near the Fermi energy creating an insulating state. Even though the gap from this calculation is smaller than measured with experimental probes, the main point is that a combination of U and SOC in this system can yield an insulating state. Note that the figure on the left of panel c) is the topology of the valence band maximum rather than the Fermi surface.

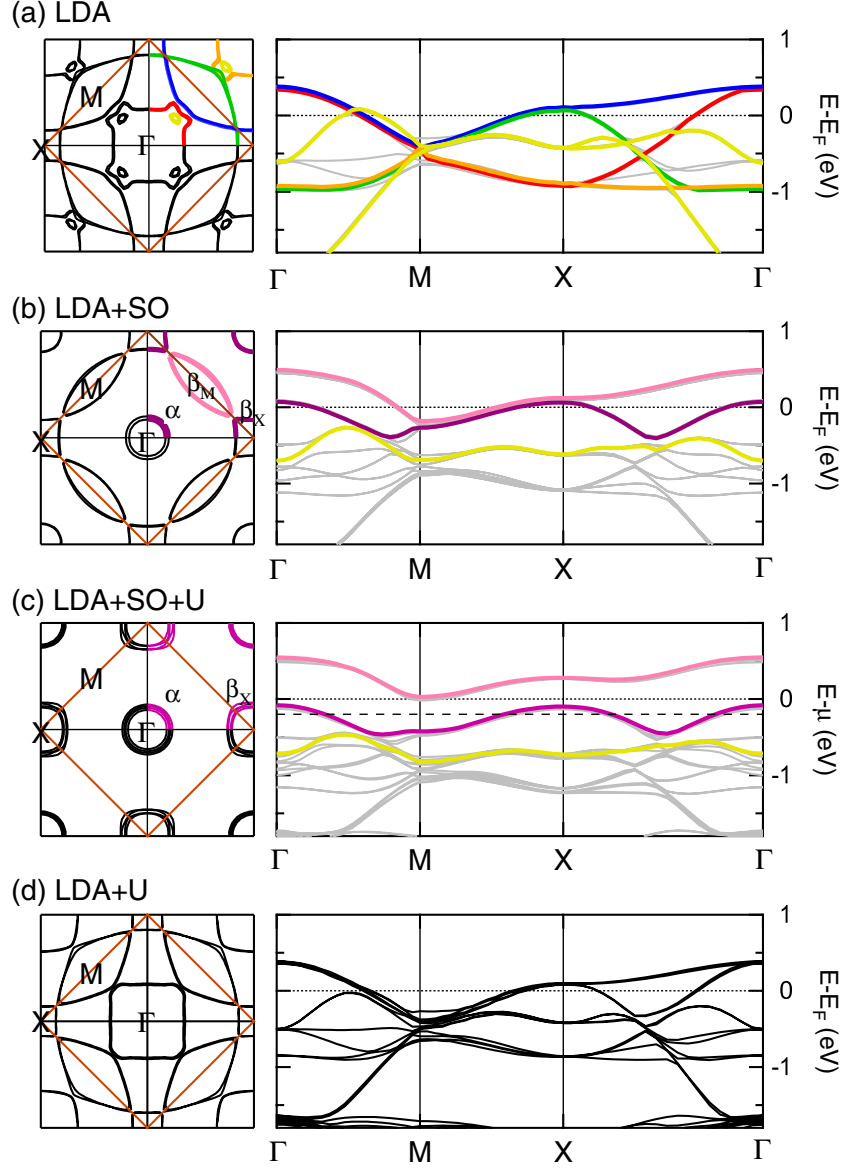


Figure 4.6: The right panel are LDA band structure calculations considering a) no SOC or U b) only SOC c) both SOC and U d) only U. The left panel represents the Fermi surface except for c) which shows the topology of the valence band maxima. [27]

## 4.5 Magnetic Ordering

This system was originally shown to be a weak ferromagnetic insulator with a critical temperature of  $T_N = 240$  K with the easy axis being the a-axis, which is the axis with a larger magnetic response [30]. This ordering can be seen in the temperature

dependence of the magnetization presented in Figure 4.7 obtained with a field of 0.1 T [31]. This weak moment was later shown by B. J. Kim *et. al.* (Reference [32]) through resonant x-ray scattering experiments to be due to canted antiferromagnetic ordering. The ordering of the moments of the  $J_{\text{eff},1/2}$  state can be seen as red arrows in Figure 4.8. In this figure the view is along the c-axis and all four unique layers necessary to construct a unit cell are illustrated. The blue squares represent the  $\text{IrO}_6$  octahedra and the green squares are for horizontal alignment. The individual and net moments are represented by red and blue arrows, respectively. The individual moments align in the ab-plane with the  $\text{IrO}_6$  octahedra. Since these octahedra are rotated about the c-axis by  $\sim 11^\circ$ , the moments are rotated by the same amount, creating the canted antiferromagnetic ordering. Note that for fields larger than  $H_c \approx 0.2$  T there is a realignment of these moments. This behavior is consistent with the field dependence of the magnetization where there is saturation for fields larger than 0.5 T and anomalies in the hysteresis loops at roughly 0.2 T. In addition to this, other anomalies appear in the temperature dependent magnetization at  $T_{M1} \sim 100$  K and  $T_{M2} \sim 25$  K. These features are likely due to additional magnetic ordering in  $\text{Sr}_2\text{IrO}_4$ .



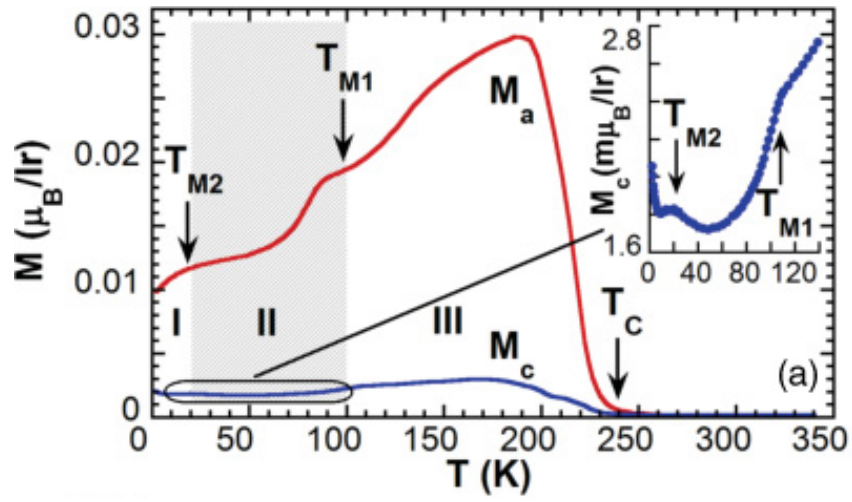


Figure 4.7: Temperature dependence of the magnetization in  $\text{Sr}_2\text{IrO}_4$  along the  $a$ -axis (red) and  $c$ -axis (blue), where  $T_C = T_N = 240$  K. (Inset) Low temperature magnetization along the  $c$ -axis. [31].

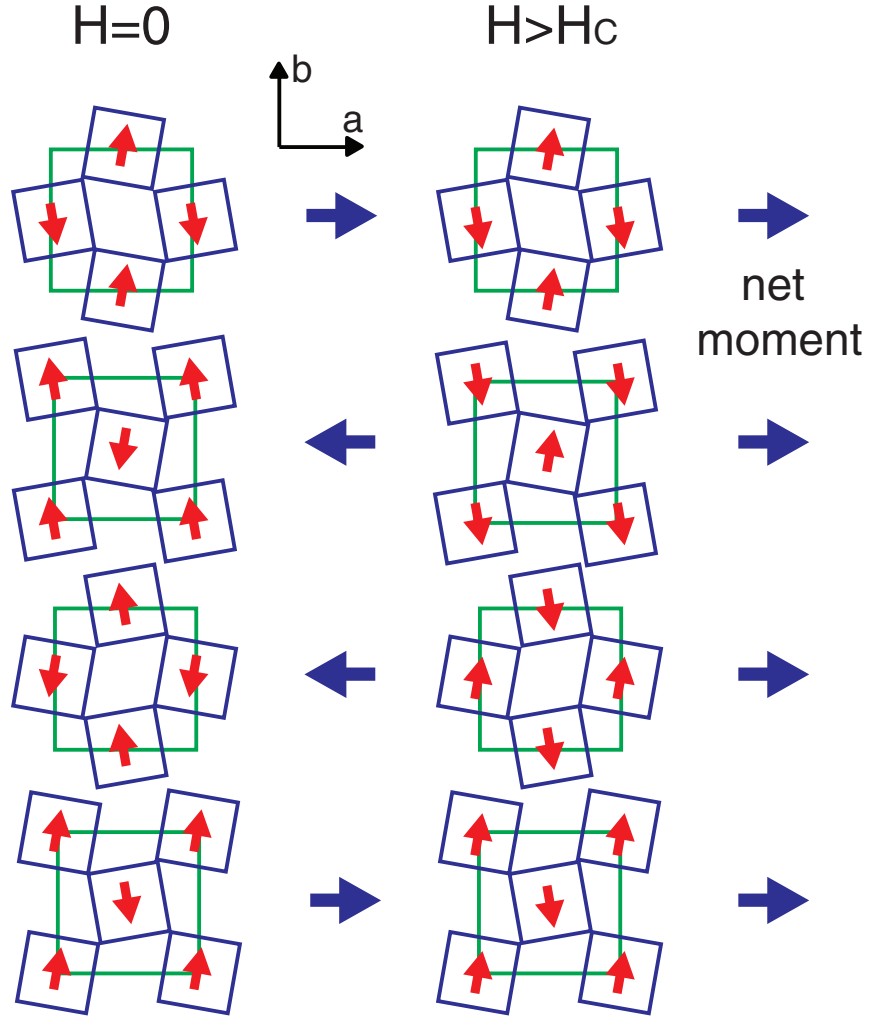


Figure 4.8: Illustration of  $J_{\text{eff},1/2}$  moment alignment in four layers of the unit cell for  $T < T_N$  with  $H = 0$  (left) and  $H > H_C = 0.2$  T (right) [32].

#### 4.6 Determination of Mott gap in $\text{Sr}_2\text{IrO}_4$

Energy gaps that appear in different materials can be observed and measured through various probes. The insulating gap in  $\text{Sr}_2\text{IrO}_4$  was first observed through optical conductivity experiments [33]. There is a peak labeled  $\alpha$  in Ref. [33] at roughly 500 meV which is due to electron excitations from the LHB to the UHB. The size of the gap is interpreted to be the onset energy associated with this absorption peak. Thus the gap measured through optical conductivity is  $2\Delta_{\text{OC}} \approx 400$  meV. The Mott gap has also been observed through resonant inelastic x-ray scattering (RIXS) measurements [34]. In RIXS experiments, the photons incident to the sample of interest have an energy carefully chosen to be at an atomic resonance of the sample. This results in a much larger cross section compared to inelastic x-ray scattering. The gap observed in RIXS was shown to be  $2\Delta_{\text{RIXS}} \approx 400$  meV which is consistent with the result from optical conductivity. It is important to note that both these measurements likely have an appreciable but unreported uncertainty associated with these values. The energy gap has also been observed in angle resolved photoemission spectroscopy (ARPES) measurements [35]. ARPES experiments measure the energy and trajectory of electrons ejected from a sample of interest due to incident light striking it. This can be used to experimentally produce band structure and the Fermi surface similar to the theoretical calculations presented in Figure 4.6. The Mott gap measured by ARPES techniques is  $2\Delta_{\text{ARPES}} \approx 580$  meV.

#### 4.7 Magnon excitations in $\text{Sr}_2\text{IrO}_4$

A phonon is a collective excitation of the positions of atoms in a solid. For example, if the atoms in some solid are collectively oscillating, this motion constitutes a phonon. A magnon is similar to a phonon except it is a collective excitation of the spin orientation rather than lattice vibrations. In other words a magnon will be present

if there is a collective modulation of the electron spin direction in a material. A magnon is also the quantized unit of energy associated with the spin waves [36]. Magnons have been observed in  $\text{Sr}_2\text{IrO}_4$  through Raman scattering [37] and RIXS [34] experiments. The Raman scattering spectrum had a peak that vanished with increasing temperature at an energy of 230 meV. This peak is attributed to a double magnon excitation. Therefore a single magnon should occur at half this value 115 meV. In addition, a single magnon at an energy of 120 meV has been observed through RIXS measurements which is consistent with the result from Raman scattering.

#### 4.8 Mott Insulator

In 1937 a new class of TMOs was discovered that have an insulating nature but were predicted to be metallic by band theory [39]. These materials include  $\text{MnO}$ ,  $\text{CoO}$ ,  $\text{Mn}_3\text{O}_4$ ,  $\text{Fe}_2\text{O}_3$ ,  $\text{CuO}$  and  $\text{NiO}$ . Later in the same year it was predicted that this insulating ground state was due to interactions between electrons which was ignored in the band theory model [40]. Roughly a decade later it was shown by N. F. Mott that for  $\text{NiO}$  in particular the insulating behavior was due to interactions between electrons and in general the electrical transport properties would be governed by the relative strengths of the Coulomb interaction and the transfer integral ( $t$ ) [41]. In addition Mott proposed that whether a material would be electrically conducting or insulating could be determined by a single variable: lattice spacing [36]. If the atoms in a material are infinitely far apart the material will be insulating and if they are infinitesimally close to one another it will be metallic. Therefore there must be some critical lattice spacing that will separate the metallic state from the insulating state. The magnitude of this critical value can be determined from the Mott criterion, which for  $1s$  states in Hydrogen is [36]:

$$2.77n_0^{1/3} < a_0^{-1} \quad (4.1)$$

where  $n_0$  is the electron density and  $a_0$  is the Bohr radius.

#### 4.9 Hubbard Model

A model which successfully accounts for the transport properties in Mott insulators was not developed until 1963 when J. Hubbard developed the Hubbard model named in his honor [42, 43, 44]. This model accounts for the on-site Coulomb interaction ( $U$ ) and the hopping integral ( $t$ ). The one band Hubbard model for a square lattice has been shown to successfully model the electronic properties of  $\text{Sr}_2\text{IrO}_4$  [28]. The Hamiltonian of this model has the following form [45]:

$$H = -t \sum_{\langle \vec{r}, \vec{r}' \rangle, \sigma} (c_{\sigma}^{\dagger}(\vec{r})c_{\sigma}(\vec{r}') + \text{h.c.}) + U \sum_{\vec{r}} n_{\uparrow}(\vec{r})n_{\downarrow}(\vec{r}) \quad (4.2)$$

where  $\vec{r}$  labels each lattice site,  $\langle \vec{r}, \vec{r}' \rangle$  are nearest neighbors,  $\sigma = \uparrow, \downarrow$  is the spin index,  $c_{\sigma}^{\dagger}$  is the annihilation operator that removes an electron from the  $J_{\text{eff},1/2}$  band,  $c_{\sigma}$  is the creation operator that places an electron in the  $J_{\text{eff},1/2}$  band and  $n_{\sigma}(\vec{r}) = c_{\sigma}^{\dagger}(\vec{r})c_{\sigma}(\vec{r})$  is the density operator. The first term is the kinetic energy term which deals with electron hopping between nearest neighbors. The second term accounts for the interactions between electrons. At each site there are four possible configurations of the  $J_{\text{eff},1/2}$  band: there will be no electrons, there will be one electron with either up-spin or down-spin or two electrons with opposite spin.

The Hubbard model is not exactly solvable for two or three dimensional systems. Therefore to model the electronic properties of  $\text{Sr}_2\text{IrO}_4$  with the Hubbard model requires an approximation technique. Since this system has canted antiferromagnetic ordering below its Neel temperature of  $T_N = 240$  K it is logical to use the Slater approximation which accounts for spin fluctuations in the lattice [46]. Within this

limit the Hamiltonian will reduce to [47]:

$$H_S = -t \sum_{\langle \vec{r}, \vec{r}' \rangle, \sigma} (c_\sigma^\dagger(\vec{r})c_\sigma(\vec{r}') + \text{h.c.}) + \frac{2U}{3} \sum_{\vec{r}} \langle \vec{S}(\vec{r}) \rangle^2 - \frac{4U}{3} \sum_{\vec{r}} \langle \vec{S}(\vec{r}) \rangle \cdot \vec{S}(\vec{r}) \quad (4.3)$$

where the spin operator is:

$$\vec{S}(\vec{r}) = \frac{1}{2} c_\sigma^\dagger(\vec{r}) \vec{\tau}_{\sigma, \sigma'} c_\sigma(\vec{r}') \quad (4.4)$$

where the operators  $\vec{\tau}$  are the spin-1/2 Pauli matrices.

The Slater approximation of the two-dimensional Hubbard model for a square lattice predicts a single particle excitation gap in  $\text{Sr}_2\text{IrO}_4$  with a magnitude of:

$$2\Delta_S = \frac{4}{3} |\vec{S}_0| U \quad (4.5)$$

Note that the effective hopping energy, the Coulomb energy and the staggered magnetic moment have been reported to be  $t = 0.26$  eV,  $U = 2.0$  eV and  $|\vec{S}_0| = 0.31$ , respectively [28]. Therefore within this approximation the full width of the gap is predicted to be  $2\Delta_S \approx 0.8$  eV, which is slightly larger than the value measured through experiments. This model predicts a density of states that is suppressed at the Fermi energy and will take the following form for  $|\epsilon| > \Delta$ :

$$\frac{\rho_S(\epsilon)}{\rho_S(0)} = \frac{|\epsilon|}{\sqrt{\epsilon^2 - \Delta^2}} \quad (4.6)$$

This result is coincidentally similar to the density of states for s-wave superconductors [14].

## Chapter 5 Tunneling in $\text{Sr}_2\text{IrO}_4$

### 5.1 Sample Preparation

A unique property of  $\text{Sr}_2\text{IrO}_4$  is that even though it remains insulating, it maintains a finite resistance even at cryogenic temperatures. From Figure 4.3 the resistivity along the c-axis at low temperatures is  $\sim 10^6 \Omega\cdot\text{cm}$ . Typical sample dimensions are  $2.5 \text{ mm} \times 2.5 \text{ mm} \times 1 \text{ mm}$  which will produce a maximum overall resistance along the c-axis of  $\sim 1 \text{ M}\Omega$ . This allows tunneling experiments, which require electrical conduction, to be conducted on this system which has an insulating ground state. The samples used in these experiments were created using the flux method and are different samples from the same batch as the samples used in the optical conductivity [33] and ARPES [35] measurements.

Since STM experiments measure the properties of a material's surface, it is critical to ensure that the surface is clean. The susceptibility of the surface quality of  $\text{Sr}_2\text{IrO}_4$  deteriorating when exposed to ambient conditions was investigated with an atomic force microscope (AFM). An AFM works in a similar manner as an STM however mechanical interactions are measured instead of a tunneling current. Typically an AFM has less spacial sensitivity than an STM but is able to investigate larger areas of the sample.

A  $\text{Sr}_2\text{IrO}_4$  crystal was cleaved and then immediately placed in the AFM for measurements. Since the AFM operates in ambient conditions, the sample surface had been exposed for approximately 20 minutes at the completion of the image acquisition. This image can be seen in Figure 5.1 a) and represents a  $3 \times 3 \mu\text{m}^2$  area of the sample surface. It was acquired using contact mode with a setpoint of  $F_N = 1.16 \text{ nN}$ . This acquisition method is similar to constant current STM, but the setpoint is a force instead of a current. So the AFM tip was swept across the sample surface

and the change in voltages applied the the z-piezo in order to maintain this setpoint is plotted. Notice that this image has a relatively flat grey background that is the underlying crystal. In addition there are several black pits and white mounds on the surface which are believed to be due to a deteriorating surface. The pits and mounds are most probably the formation of strontium oxide ( $\text{SrO}_2$ ) on the surface. This formation of oxide continues with time as illustrated in Figure 5.1 b) which displays the surface of the same  $\text{Sr}_2\text{IrO}_4$  crystal roughly one month after it was cleaved. Now the entire surface consists of the oxide layer. Notice that the full range of the false color scale is approximately 4 times larger implying that these features are much larger the ones observed shortly after cleaving. Also note that this is a relative scale. This means that since the underlying crystal cannot be viewed in the image, the absolute thickness of the oxide layer cannot be determined. However it can be concluded that the surface roughness is  $\sim 8$  nm and that the oxide layer is at least this thick.

This proves that in order to do STM measurements on  $\text{Sr}_2\text{IrO}_4$ , the surface must never be exposed to ambient conditions. This can be accomplished by cleaving the sample *in situ*. This means that the sample is broken while under vacuum and then mounted to the STM for measurements without breaking the vacuum. This is done by gluing a thin rod to the end of the sample and then knocking the bar off the crystal while in vacuum and potentially at cryogenic temperatures. Ideally this will result in the crystal breaking and exposing a clean surface. Typically, in our laboratory samples are mounted to the STM sample holder with a conducting epoxy (Epoxy Technology E4110). This naturally provides the electrical contact to the sample necessary for STM experiments. This proved to be problematic with  $\text{Sr}_2\text{IrO}_4$  due to the strength of the crystal. When attempting to cleave these crystals using the conducting epoxy, the most common occurrence was either the entire sample remained on the sample holder or the cleave rod. Therefore the samples and cleave rods were attached with a stronger epoxy (Stycast 2850FT) which is insulating in nature. The



electrical contact with the sample was then made by placing silver paint over the insulating epoxy bridging the sample and sample holder. The configuration for how  $\text{Sr}_2\text{IrO}_4$  crystals were mounted in order to cleave the crystals *in situ* is illustrated in Figure 5.2.

Our STM experiments were conducted in a cryogenic probe that is evacuated and then submerged in a cryogenic liquid. This allows the pressure of the probe to be improved by cryogenic pumping. So if the sample is cleaved at lower temperatures, the sample surface will be more pure due to the improved base pressure. All results presented in this thesis obtained from STM experiments on  $\text{Sr}_2\text{IrO}_4$  were conducted on samples that were cleaved *in situ* at  $T = 77$  K. Samples were cleaved along the ab-plane and mounted in the STM such that the tunneling was into the c-axis. In other words, the STM tip was parallel to the c-axis.

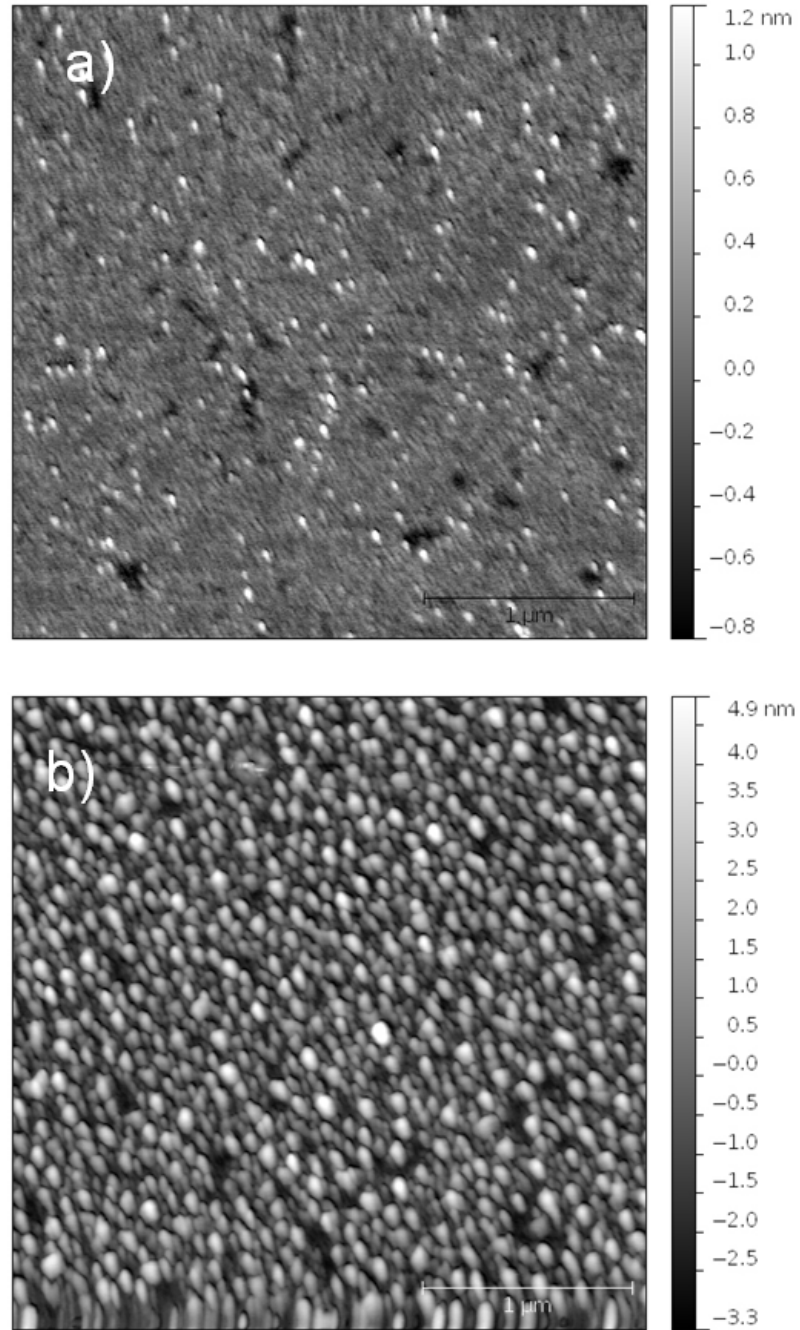


Figure 5.1: Contact mode AFM images of  $3 \times 3 \mu\text{m}^2$  area of  $\text{Sr}_2\text{IrO}_4$  surface taken with  $F_N = 1.16 \text{ nN}$ . The images were obtained on the same sample a)  $\sim 20$  minutes after cleaving and b)  $\sim 4$  weeks after cleaving.

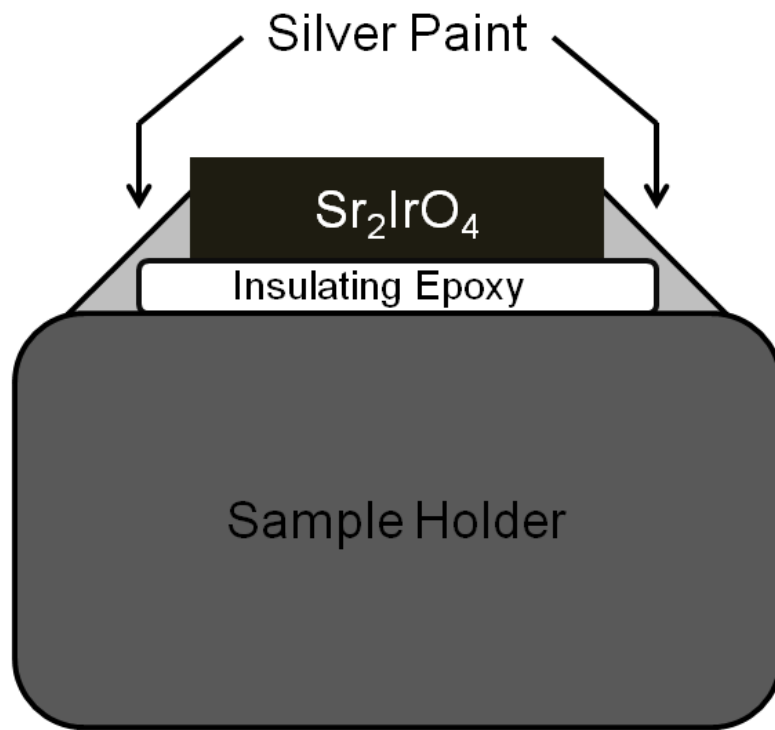


Figure 5.2: The sample mounting configuration of  $\text{Sr}_2\text{IrO}_4$  for STM experiments. The samples were initially attached with a strong insulating epoxy and then electrical contact to the crystal was made with silver paint.

## 5.2 STM Setup

Since an STM has a very large spatial sensitivity, it is essential to isolate it from external mechanical vibrations. Thus in order to accomplish STM experiments at cryogenic temperatures care must be taken in the design of the experimental setup. Typically removing mechanical coupling with the surroundings will also remove thermal coupling. Therefore it is necessary to have enough mechanical isolation to successfully perform the measurement while keeping the thermal time constants in changing the STM temperature small enough to be practical. This was accomplished by attaching the STM to the end of the cryogenic probe through a spring isolation stage as illustrated in Figure 5.3 The central pipe serves for vacuum pumping. The remaining pipes are conduits for the many wires required for the STM. Since these tubes are also under vacuum the electrical connectors used must be hermetically sealed. The vacuum chamber is made of brass and connects to the end of the probe. This seal is made vacuum tight by smashing an indium o-ring between the two pieces.

The end of the probe with the STM is shown with magnification to the right of Figure 5.3. Most of the parts are made from brass. Note that the central pipe that goes through the entire probe allows samples to be exchanged. In addition to the spring stage, there is also a movable cap and a cleave bar necessary for *in situ* sample cleaving. In order to accomplish this, a load lock vacuum chamber is placed on top of the probe. A long stainless steel sample transfer rod is attached to the top of load lock with a double o-ring seal. This creates a mechanical feed through that allows for rotational motion as well as motion along the length of the transfer rod. This transfer rod has a gear near its end and a left-handed thread on its end. The sample holders are also made of brass and can be mounted to the STM with a right-handed thread. Similarly the transfer rod can engage and disengage the sample holder *in situ* with the left-handed thread. This allows for samples to be mounted to the STM and

removed with only rotational motion. Samples can be cleaved by gluing a small rod on the end of the sample. If a cleave bar is moved perpendicular to this rod, the rod on the sample should break away with part of the sample still attached to it. This should result in a freshly cleaved sample remaining on the sample holder. Notice that the cleave bar is shown in Figure 5.3 and it has a gear near the top. This enables the gear on the sample exchange rod to engage this gear and rotate the cleave bar. After cleaving, the thin rod that was glued to the sample will fall and remain in the vacuum chamber. To ensure that it does not fall into the STM, the hole in the center must be covered. Therefore a movable cap is placed in the chamber with a similar gear that can be engaged to cover and uncover the central hole.

A single crystal of  $\text{Sr}_2\text{IrO}_4$  was cleaved *in situ* at  $T = 77$  K and then mounted to the STM such that the STM tip was parallel to the c-axis. This fresh surface was then imaged using an electrochemically etched tungsten tip. The tips were etched using a 3 M solution of NaOH. Tungsten wire with a diameter of 0.25 mm is placed through a lamella of the etchant and an AC voltage of  $V_{\text{rms}} = 1.5$  V is applied. The etching continues until the remaining wire is thin enough that the two pieces are separated by the weight of the wire below the lamella. The bottom piece is allowed to fall into a cup that is placed underneath the tungsten wire. This opens the electrical etching circuit and preserves the sharpness of the STM tip. STM tips created this way have been studied with a scanning electron microscope. These studies showed that these tips have a typical radius of curvature of  $\sim 25 - 50$  nm, many of which were capable of producing atomic resolution images of a freshly cleaved HOPG surface. An example of a scanning electron microscope image of an electrochemically etched tungsten tip can be viewed in Figure 5.4. Panel a) displays a high resolution image which illustrates the radius of curvature of the apex of the tip to be  $\sim 40$  nm while panel b) displays a lower resolution image to illustrate the basic shape of an STM tip. A problem with using tungsten STM tips is that tungsten oxide is produced

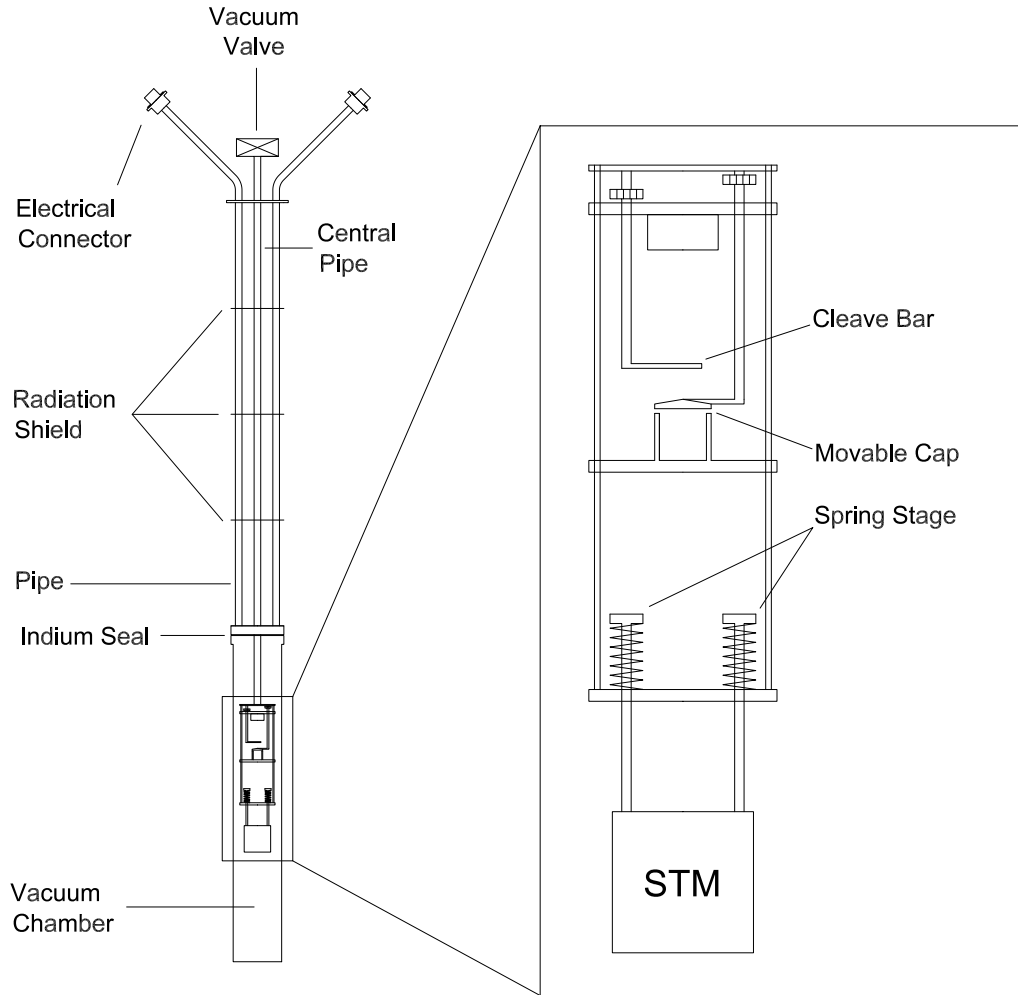


Figure 5.3: The design of the probe used for cryogenic STM experiments. The image on right is magnification of the end of the probe which rests inside the vacuum chamber.

during the etching process and must be completely removed from the apex of the tip. This is accomplished by submerging the tip in deionized water for roughly 5 minutes followed by submerging it in HF for  $\sim 30$  s. The residual HF must then be removed by submerging the tip in deionized water. The tip would then have the water blown off with compressed nitrogen gas and immediately installed in the STM and then put in a vacuum chamber.

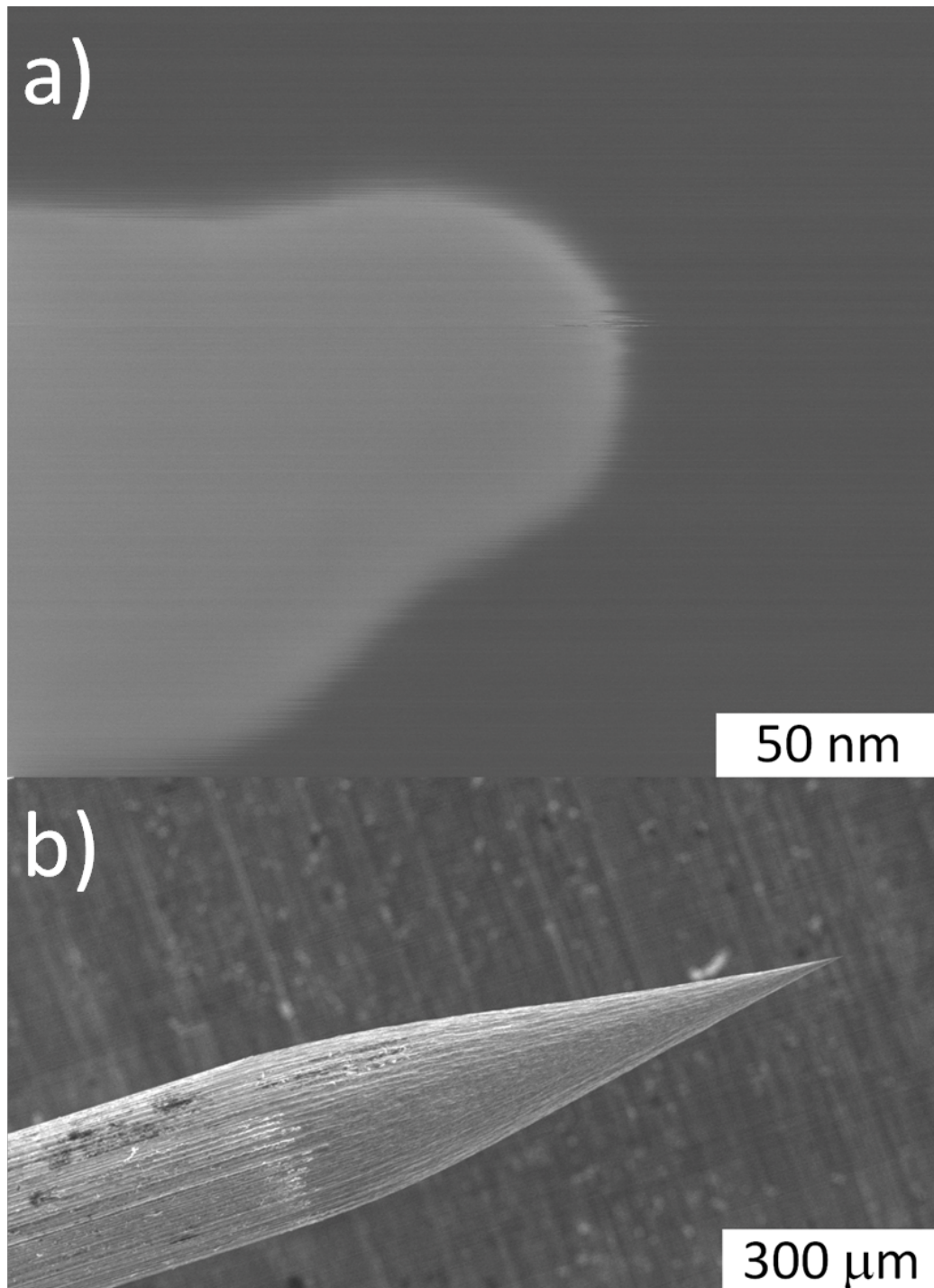


Figure 5.4: Scanning electron microscope images of an electrochemically etched tungsten tip with a magnification of a)  $\times 500,000$  and b)  $\times 80$ .

### 5.3 Experimental Results and Analysis

A typical STM image (top) of  $\text{Sr}_2\text{IrO}_4$  and line profile (bottom) can be seen in Figure 5.5. This image is the raw data constant current image of a  $109 \times 109 \text{ nm}^2$  area of the sample surface. The bias voltage was  $V_{\text{bias}} = 300 \text{ mV}$  and the tunnel current setpoint was  $I_{\text{set}} = 200 \text{ pA}$ . This positive bias enabled electrons in the tip to tunnel into empty states in the sample. There are three primary regions of this figure labeled I, II and III. Layer I is the dark grey region located near the center, while layer II is the light grey region located on either side of layer I and layer III is the white region located on the right of the image. This can be more easily seen in the line profile which is represented as a white line in the image. This line profile shows that two adjacent layers are separated by a sharp step. Recall that the  $c$  lattice parameter in  $\text{Sr}_2\text{IrO}_4$  is  $25.799 \text{ \AA}$  [23]. Since the  $\text{IrO}_6$  octahedra rotate about the  $c$ -axis, the unit cell is quadrupled in this direction. This results in two adjacent layers of  $\text{Sr}_2\text{IrO}_4$  being separated by  $\sim 7 \text{ \AA}$ . This is consistent with the separation between layers I and III. This suggests that these two layers have the same chemical makeup and are in two adjacent layers. Also the distance between layers I and II is roughly one third of this value. This coupled to the fact that the electronic properties of each layer was the same suggests that each exposed layer is an SrO layer and that layers II and III are from the same layer while layer I is from an adjacent one as shown in Fig. 4.2. It was typical to have the electrically insulating SrO layer exposed after cleaving.

In addition, smaller scale images of the sample surface were acquired as illustrated in Figure 5.6. This image represents an  $11.2 \times 11.2 \text{ nm}^2$  area of Layer II from the upper left corner of Figure 5.5. This image was also obtained with  $V_{\text{bias}} = 300 \text{ mV}$  and  $I_{\text{set}} = 200 \text{ pA}$ . Notice that there is structure, however the spacing between features is larger than the  $a$  lattice parameter. For example, two adjacent features are separated by  $\sim 17 \text{ \AA}$  which is roughly seven times larger than the distance between



two adjacent Ir atoms. The inability to achieve periodic atomic structure in this system is attributed to the conducting IrO layer being screened by the exposed SrO<sub>2</sub> layer. The observed structure which is incommensurate with the underlying lattice suggests this material is inhomogeneous. The inhomogeneity of Sr<sub>2</sub>IrO<sub>4</sub> can also be seen in the behavior of the Ir-O-Ir bond angle ( $\theta$ ) for the oxygen depleted system Sr<sub>2</sub>IrO<sub>4- $\delta$</sub>  [48].

It has been shown that sharp STM tips can provide additional features in tunneling spectroscopy [49]. In other words, the shape of the STM tip can create a non-constant density of states in the tip, making Equation 2.26 invalid. This effect is minimized with duller tips. Therefore in order to provide more consistent results an intentionally blunt gold tip was used to acquire the tunneling spectra presented below. These tips were created by melting the end of a 0.25 mm diameter gold wire with a hydrogen torch. This results in the apex of the tip being a sphere with a diameter of 0.5 mm. In addition to providing a constant tip DOS, the blunt tip will spatially average the tunneling spectrum about a small area of the sample surface eliminating effects due to the sample being inhomogeneous.

The electronic structure was investigated through scanning tunneling spectroscopy at two temperatures 77 K and 4.2 K. A typical result obtained at 77 K is presented as a red curve in Figure 5.7. Notice that there is a suppression of the DOS near the Fermi energy. In addition, there is a slight asymmetry between positive and negative bias. This is consistent with the particle-hole asymmetry previously reported in Sr<sub>2</sub>IrO<sub>4</sub> [28]. The two high energy peaks at roughly  $\pm 350$  meV are due to the Mott gap present in this material. Recall from Chapter 4 that the one-band Hubbard model for a square lattice predicts that the density of states will have the form  $|\epsilon|/\sqrt{\epsilon^2 - \Delta^2}$ . Substituting this result into Equation 2.27 will result in the following expression for

the tunneling current:

$$\frac{dI}{dV} \propto \int_{-\infty}^{\infty} d\epsilon \frac{|\epsilon|}{\sqrt{\epsilon^2 - \Delta^2}} \frac{e^{(\epsilon+eV)/k_B T^*}}{k_B T^* (1 + e^{(\epsilon+eV)/k_B T^*})^2} \quad (5.1)$$

Due to particle-hole asymmetry in  $\text{Sr}_2\text{IrO}_4$  the two high energy peaks in the tunneling spectroscopy are separately fit to Equation 5.1. The fits have two parameters  $\Delta$  and  $T^*$  and are represented as dashed lines in Figure 5.7. The parameters to the fit for positive bias voltages are  $\Delta_+ = 303$  meV and  $T_+^* = 519$  K and the parameters to the fit for negative bias voltages are  $\Delta_- = 312$  meV and  $T_-^* = 633$  K. This implies that the full Mott gap measured through tunneling spectroscopy is  $2\Delta \approx 615$  meV. This value is slightly smaller than predicted through the Slater approximation of the one-band Hubbard model of  $2\Delta = \frac{4}{3}U|\vec{S}_0| \approx 800$  meV, where the on-site Coulomb interaction and the staggered magnetic moment are respectively  $U \approx 2.0$  eV and  $\vec{S}_0 = 0.307$  [50, 47]. Conversely our measured result is slightly larger than the gap measured by optical conductivity, angle resolved photoemission spectroscopy (ARPES) and resonant inelastic x-ray (RIXS) experiments. Values for the Mott insulating gap in  $\text{Sr}_2\text{IrO}_4$  from different experimental techniques are presented in Table 5.1.

The Slater approximation does accurately predict the shape of the gap thus allowing the magnitude of the gap to be extrapolated from the experimental data. However this models fails to accurately predict the position or the broad width of these features. The Slater approximation predicts that the peaks should be infinitesimally narrow at  $T = 0$  K and the width at finite temperature should be due solely due to thermal broadening. If this were the case, the parameters  $T_+^*$  and  $T_-^*$  would be equal to  $T = 77$  K, the temperature at which the data was acquired. However, these parameters are several times larger than 77 K suggesting that the Slater approximation does not fully model the electronic properties of  $\text{Sr}_2\text{IrO}_4$ . The one-band Hubbard model for  $\text{Sr}_2\text{IrO}_4$  has also been solved utilizing dynamical mean field the-

ory [50]. They were able to determine a spectral function that predicts the shape of the insulating gap. However it predicts this feature to be much broader than we observed experimentally. This suggests that neither the Slater approximation nor dynamical mean field theory accurately describes this system. Since the Slater approximation ignores the frequency dependence of the self energy and dynamical mean field theory ignores the momentum dependence of the self energy [51], any model that accurately describes this system likely will have to account for both the frequency and momentum dependence of the self energy.

Inside the Mott gap there are two features that appear as shoulders. Since  $\text{Sr}_2\text{IrO}_4$  has magnetic ordering below its Neel temperature of  $T_N = 240$  K and charge effects should be suppressed inside the gap, it is believed that these features are due to inelastic tunneling from a single magnon. Features from inelastic tunneling should appear as features in the voltage derivative of the differential tunneling conductance ( $d^2I/dV^2$ ) [52]. Since inelastic loss features in the differential tunneling conductance should be symmetric the obvious asymmetry in these features is attributed to the particle-hole asymmetry. Therefore we defined a new function  $g$  to be the even part of the differential conductance presented in Figure 5.7. This function was obtained by fitting the data to a Fourier sine series and equating  $g$  to the sum of the even terms in the series. This expression was then differentiated and presented in the inset of Figure 5.7. Notice that there is a peak at 125 meV. This value is consistent with the single magnon observed in RIXS of 120 meV [34] and roughly half the double magnon observed through Raman scattering of 240 meV [37].

A convenient property of this material is the behavior of its electrical transport properties at low temperatures. Instead of the electrical resistance exhibiting an Arrhenius type behavior as expected in more conventional insulators driven by thermal excitations, it approximately flattens out with decreasing temperature (Figure 4.3). Therefore the electrical resistance at  $T = 4.2$  K is comparable to its value at  $T =$

Experiment	$2\Delta$ (meV)	Reference
STM	615	This Study
Optical Conductivity	400	[33]
ARPES	580	[35]
RIXS	400	[34]

Table 5.1: Measured values of the Mott gap ( $2\Delta$ ) in  $\text{Sr}_2\text{IrO}_4$  with various experimental probes.

77 K. This makes  $\text{Sr}_2\text{IrO}_4$  a unique insulator regarding its ability to have tunneling experiments performed on it even at liquid helium temperatures. The differential tunneling conductance taken at  $T = 4.2$  K can be seen in Figure 5.8 a). Notice that the signal at this temperature is about an order of magnitude smaller than at  $T = 77$  K. Also notice that there are features at values comparable to the four features observed at  $T = 77$  K which we feel still represent the insulating gap and the single magnon excitation. This is consistent with the temperature dependence of the optical conductivity which shows the insulating gap to be approximately independent of temperature [33] and the Raman scattering which shows that the double magnon excitation decreases in magnitude with rising temperature but maintains the same value [37].

Surprisingly for energies less than the single magnon observed at  $T = 77$  K, additional features became present. It has been shown that additional magnetic ordering has been observed at temperatures of 100 K and 25 K [31]. This makes it likely for the new features to be inelastic loss features due to this additional ordering. The positions of these features are at energies significantly less than  $\Delta$ . The differential tunneling conductance was differentiated numerically and presented in Figure 5.8 b) where the red and blue curves were taken at 77 K and 4.2 K respectively and the dashed line is a guide for the eye. The  $d^2I/dV^2$  curve represents the density of states of inelastic excitations such as magnons. Note that there is an apparent asymmetry that appears as a systematic shift in the data to the left. Since during data acquisition

the bias voltage was swept from positive to negative voltages this shift is attributed to the time constant of the lock-in amplifier and will be ignored. Notice that there are prominent features in the blue curve at roughly  $\pm 35$  meV. Since there are also subtle features at comparable positions in the red curve suggests that the magnetic ordering that occurs at  $T = 100$  K has a magnon of  $\sim 35$  meV associated with it that is suppressed with increasing temperature. Also note that there are features at energies of approximately  $\pm 12$  meV in the blue curve that are fully suppressed suggesting that the magnetic ordering that occurs at  $T = 25$  K has a magnon associated with it that has an energy of  $\sim 12$  meV.

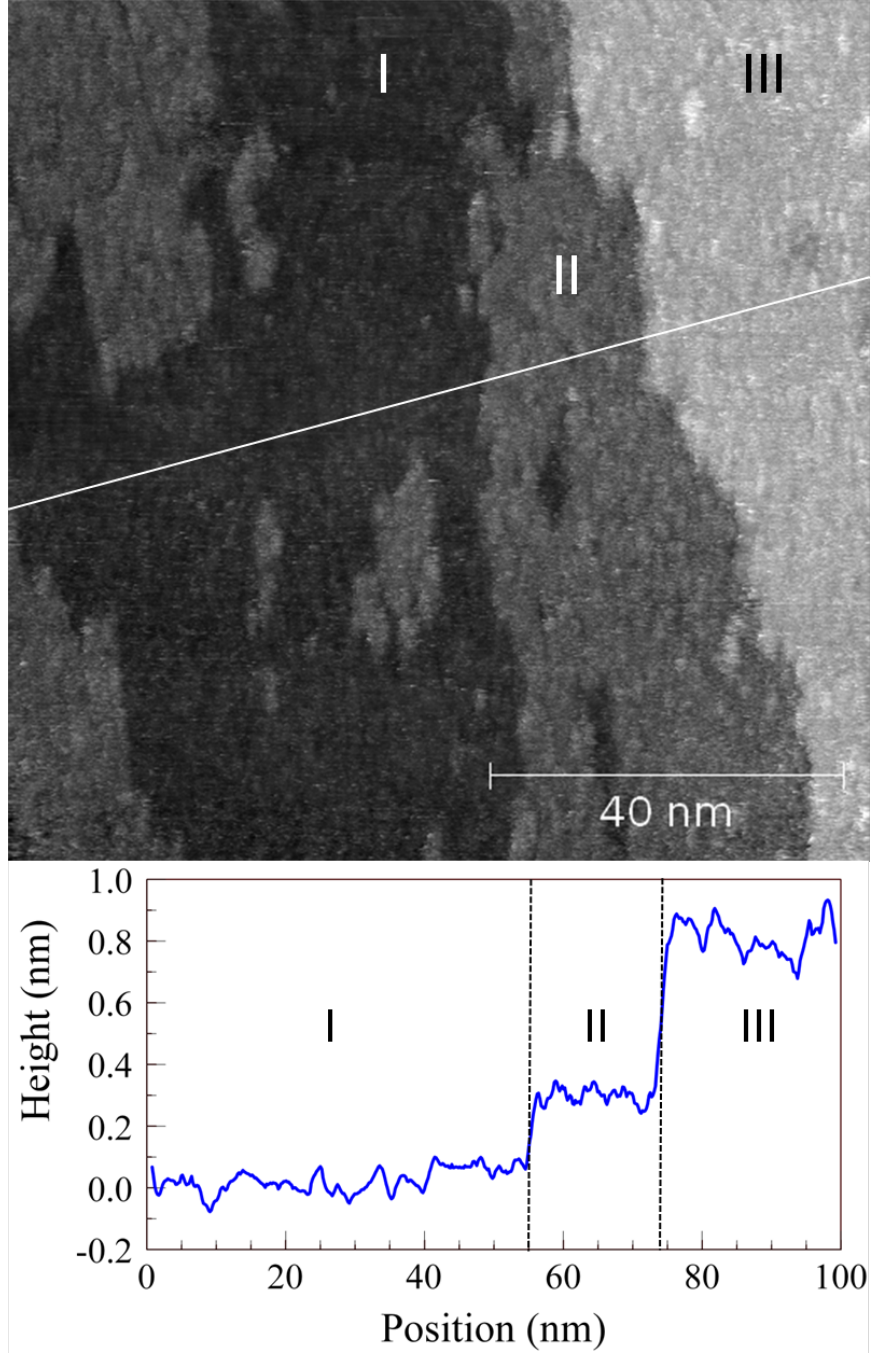


Figure 5.5: (top) A constant current image of  $109 \times 109 \text{ nm}^2$  area of  $\text{Sr}_2\text{IrO}_4$  surface taken with  $V_{\text{bias}} = 300 \text{ mV}$  and  $I_{\text{set}} = 200 \text{ pA}$ . The three layers labeled I, II and III are three different atomic layers as indicated in Figure 4.2. (bottom) A line profile of the image represented as a white line in the image.

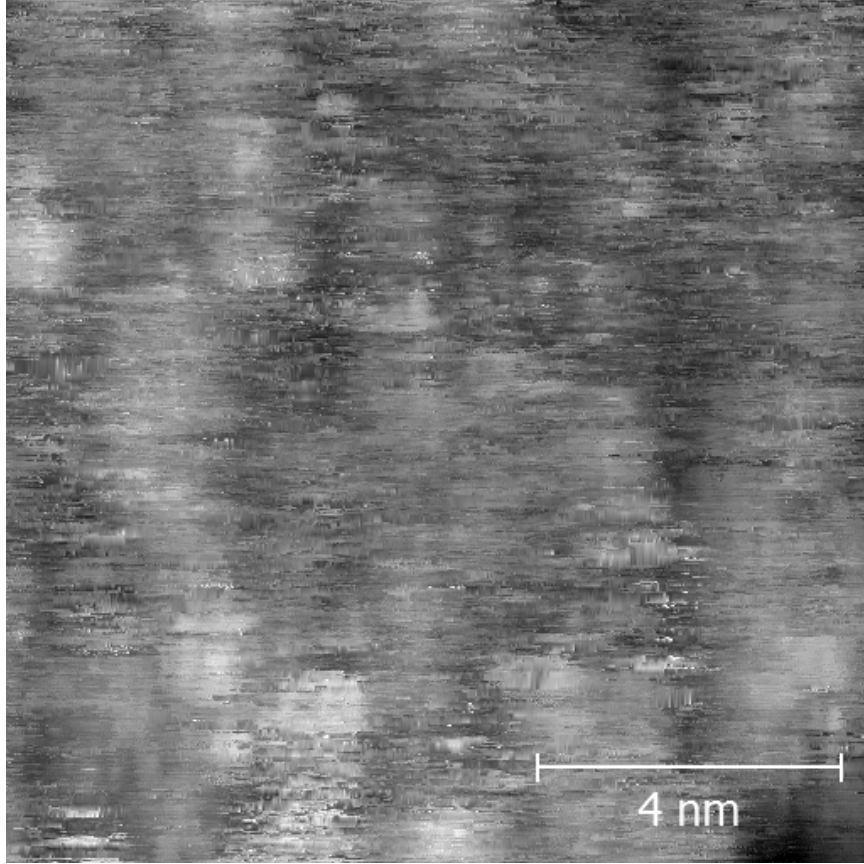


Figure 5.6: A constant current image of  $11.2 \times 11.2 \text{ nm}^2$  area of Layer II of the same  $\text{Sr}_2\text{IrO}_4$  surface illustrated in Figure 5.5. It was obtained with  $V_{\text{bias}} = 300 \text{ mV}$  and  $I_{\text{set}} = 200 \text{ pA}$ .

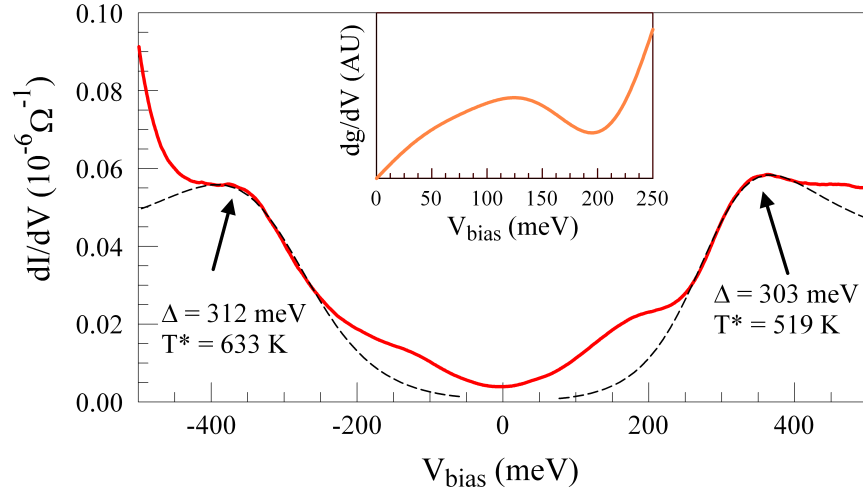


Figure 5.7: The red curve is the differential tunneling conductance of  $\text{Sr}_2\text{IrO}_4$  at  $T = 77$  K. It was acquired from a lock-in amplifier with  $V_{\text{mod}} = 4$  mV and  $f_{\text{mod}} = 703.4$  Hz. The dashed lines are fits to Equation 5.1. Inset: The orange curve is the derivative of the even component of the differential tunneling conductance.



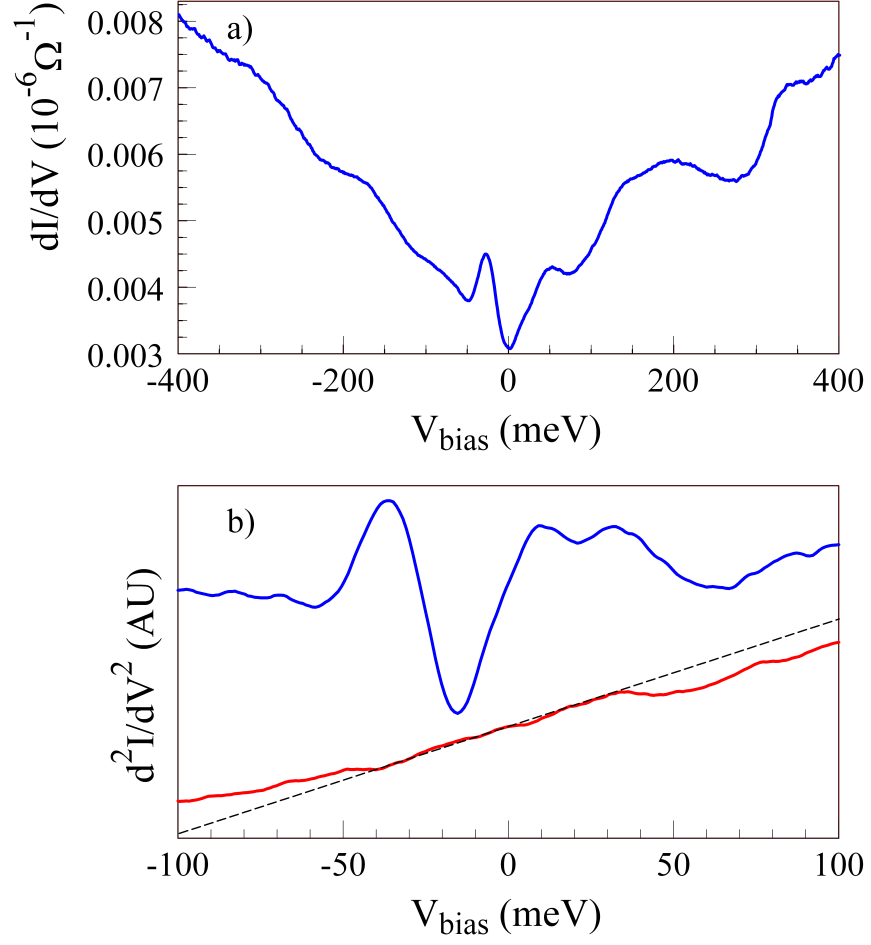


Figure 5.8: a) The differential tunneling conductance of  $\text{Sr}_2\text{IrO}_4$  at  $T = 4.2$  K. It was acquired from a lock-in amplifier with  $V_{\text{mod}} = 10$  mV and  $f_{\text{mod}} = 704.2$  Hz. b) The voltage derivative of the differential tunneling conductance ( $d^2I/dV^2$ ) at  $T = 4.2$  K (blue) and  $T = 77$  K (red). The data was obtained by taking a numerical derivative of the differential conductance presented above. The dashed line is a guide for the eye.

## PART II

Development of a scanning tunneling microscope with long range lateral  
motion

## Chapter 6 Scanning tunneling microscope with long range lateral motion

Ever since the discovery of the scanning tunneling microscope (STM) by Gerg Binnig and Heinrich Rohrer [53], it has proven to be influential to understanding conducting materials such as superconductors [1, 2, 3], charge density waves [5, 6] and Mott “insulators” [7, 8, 9]. The maximum displacements from an STM scanner is typically  $\sim 1\mu\text{m}$  [54]. Therefore all STMs require a coarse motion mechanism in order to achieve tunneling conditions. Typically this coarse motion, which can traverse the STM tip over macroscopic distances, is achieved by piezoelectric actuation in either an inertial slider [55, 56] or slip-stick [15, 57] configuration.

In the first part of this thesis I described the basic functionality of a conventional STM with a slip-stick actuator which was used to investigate the Mott insulating system  $\text{Sr}_2\text{IrO}_4$ . This instrument along with the majority of other STM’s have a major limitation of only being able to investigate microscopically small areas of the sample surface. This is due to the coarse motion of conventional STMs only be capable of translating the STM tip over macroscopic distances ( $\sim 1\text{ mm}$ ) along the z-axis which is parallel to the tip. Many experiments require long range motion in a direction parallel to the sample surface (x and y). For example, it is known that the electrical properties of charge density wave materials vary from one contact to the other. Additional long range motion would enable the evolution of these electrical properties in between the two contacts to be determined. Other examples include studying the proximity effect near a normal metal-superconducting interface or charge transport near a metal-semiconductor interface. The long range lateral motion would enable it to produce numerous tunneling junctions without exchanging the tip or sample. This would make STM experiments on microscopically small samples such as graphene possible. Typically graphene is produced through mechanical exfoliation

and single layers occupy less than 1% of the substrate. This makes it highly probable that no samples of interest would lie inside the microscopically small scan range of a conventional STM. Therefore the probability of finding a single layer of graphene would be drastically improved by investigating different areas of the surface until an acceptable sample is located.

Several STMs that address the need of long range lateral motion have been designed [16, 58, 59]. I will discuss a newly designed STM that we have developed with coarse motion in two dimensions [17, 60]. In addition to being able to translate the tip along the z-axis, as any STM must be capable, it can displace the STM tip macroscopic distances in the x-direction, which is perpendicular to the tip and parallel to the sample surface. This STM was designed to be light and compact making it ultrastable. It is capable of producing atomic resolution images of highly oriented pyrolytic graphite (HOPG). It is compact enough to fit inside our low temperature probe and has been shown to work at cryogenic temperatures. It was constructed entirely out of non-magnetic materials making experiments inside a magnetic field possible.

## 6.1 Design

The coarse approach of this newly constructed long range STM is based on principles similar to the conventional STM described in Part I. It utilizes slip-stick motion with piezoelectric actuators. However instead of using stacks of shear mode piezoelectric plates, it utilizes piezoelectric tubes similar to the tubes used for the scanner. Its coarse approach consists of six piezoelectric tubes made of PZT-8 with nickel electrodes on both the inner and outer walls of the tubes. The outer electrode of each tube is cut in half with two axial cuts as illustrated in Figure 6.1. The walker assembly was constructed by gluing the six piezoelectric tubes to a central Macor piece. The tubes were aligned such that the cuts were on the top and bottom of the assembly. Each

tube has a length, outer diameter and wall thickness of 9.27 mm, 6.35 mm and 0.51 mm, respectively. Small sapphire disks were attached to both the top and bottom of the free end of each tube as shown in Figure 6.1. Each disk has a diameter of 2.5 mm and a thickness of 0.5 mm. Since each tube serves as a microscopic actuator, it was necessary to make an electrical contact to each electrode that has weak mechanical coupling with its surroundings. This was accomplished by soldering a small 0.045 mm diameter wire to both outer electrodes and the inner electrode of all six tubes.

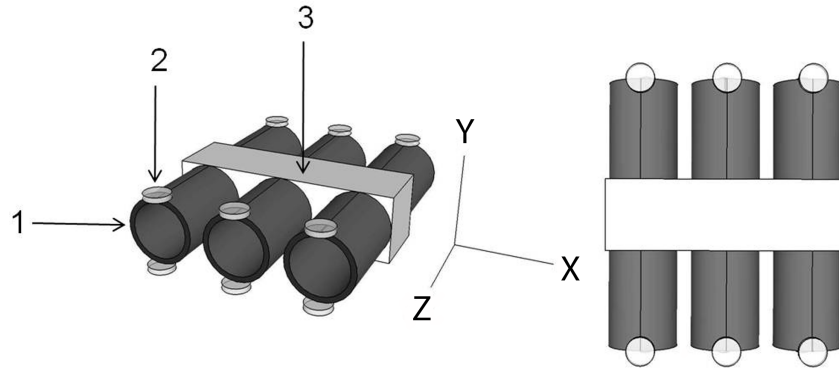


Figure 6.1: Illustration of the walker assembly: 1) piezoelectric tube, 2) sapphire disk and 3) central Macor piece.

The two outer electrodes enable the free end of each tube to move in two dimensions. Identical to the tubes used for the scanner, if the voltages applied to each outer electrode are identical in both magnitude and polarity, the tube will elongate or contract enabling motion along the z-axis. For the polarization convention of the piezoelectric tubes used, a positive applied voltage to both outer electrodes while holding the inner electrode at ground potential will cause the tube to contract. Similarly, the tube will elongate when negative voltages are applied to each outer electrode. The tube will move along the x-axis by applying voltages with equal magnitude and opposite polarity to the two outer electrodes. If the inner electrode is grounded, then the half of the tube with a positive applied voltage will contract while the half with the negative applied voltage will elongate by the same amount. This results in the

free end of each tube moving along the x-axis. An illustration of how voltages of a given polarity will lead to motion in each dimension can be seen in the top of Figure 6.2.

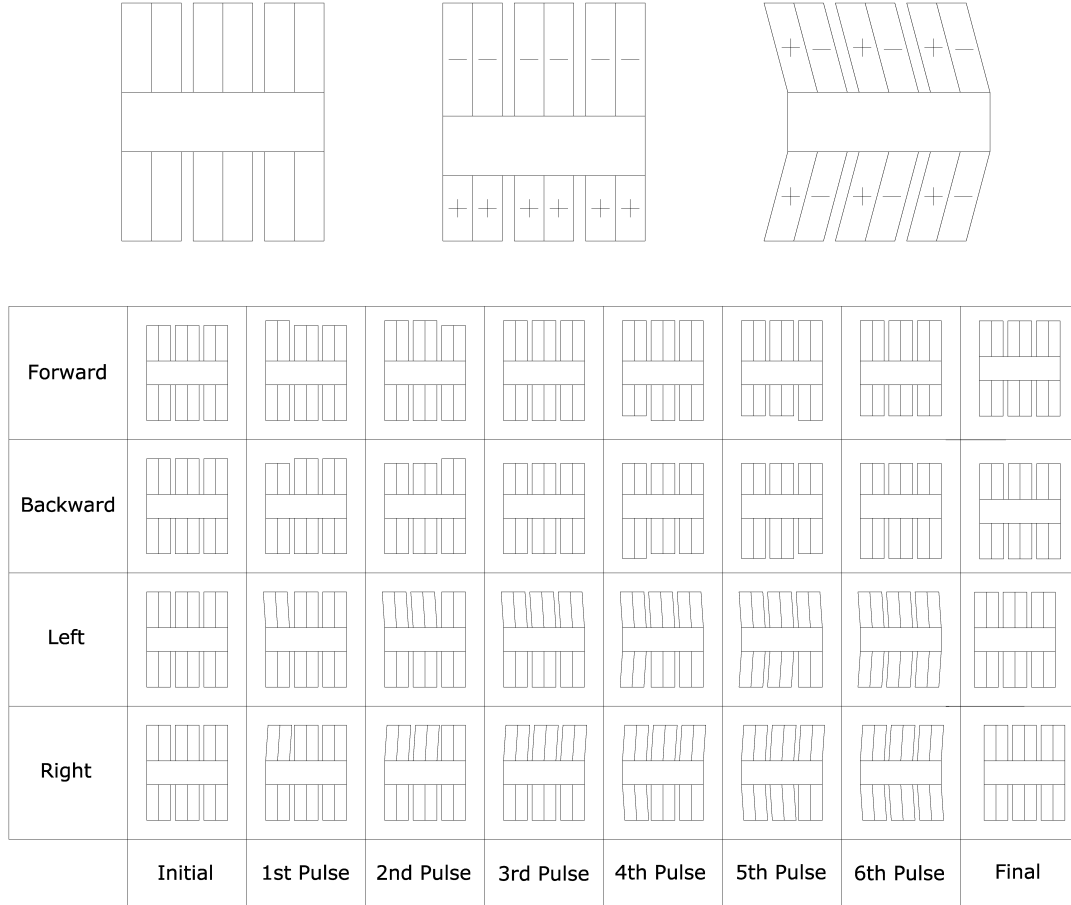


Figure 6.2: (top left) The walker assembly in the relaxed state with all electrodes held at ground potential. (top middle) The walker assembly with legs elongated and contracted for motion in the z-direction. (top right) The walker assembly with legs bent for motion in the x-direction. (Bottom) Diagram of how individual pulses are orchestrated to obtain net motion in all four directions.

An exploded view of the entire long range STM is illustrated in Figure 6.3. In the middle, the walker assembly labeled number 4 can be seen with the scanner and tip concentrically installed into one of the tubes. The scanner is also made of PZT-8 and has a diameter of 3.18 mm, a wall thickness of 0.51 mm and an overall length of 4.57 mm. The effective length of the section of the tube responsible for scanning in the

xy-plane is 1.91 mm. This scanner is roughly half the size of the scanners installed in our conventional STMs making its maximum scan area ( $150 \times 150 \text{ nm}^2$ ) roughly four times smaller. However the long range motion of this STM more than compensates for its limited scan area of a single scan. The main body of the STM is made of two Macor pieces placed above and below the walker assembly. Sandwiched in between each Macor piece and the walker is a thin optically polished alumina oxide plate. These plates and sapphire disks provide the smooth hard interface necessary for slip-stick motion. For this type of motion, the scanner must be held with a frictional force that is large enough to hold the walker assembly stationary and small enough that the piezo tubes can break the static friction and move relative to the STM body. Precise control of the magnitude of the frictional force is achieved by a differential spring system. Four stiff springs are attached to the lower Macor piece in between the two Macor pieces and four soft spring are attached to the lower Macor piece in between it and the stainless steel bars. All eight springs are made of beryllium copper. The four stainless steel screws pass through both Macor pieces and thread into holes in the stainless steel bars. As the screws are tightened the soft springs compress more than the stiff ones yielding great control of the magnitude of the frictional force. With this design of STM care must be taken to ensure that the frictional force is optimal and the two alumina plates are parallel to one another.

Once the STM is assembled with an ideal frictional force, motion can be achieved by applying appropriate voltage pulses to each electrode as illustrated in the bottom of Figure 6.2. For example, for motion in the z direction (forward/backward) identical pulses are applied to both outer electrodes of only one walker leg. The pulse rapidly applies a large voltage to the leg and holds it there. The ramp time of this transition is  $\sim 10 \text{ } \mu\text{s}$ . This pulse causes the leg to rapidly move in the desired direction of motion. The remaining five legs hold the walker assembly stationary while the other legs move relative to the STM body. This process is repeated one by one until all six walker legs

are in the stressed state. Now the voltages are slowly removed simultaneously from all six walker legs allowing them to relax. This process results in the center of mass of the walker assembly translating a microscopic distance along the z-axis. Similarly, motion in the x direction (left/right) can be achieved by going through the same process except the voltage pulses applied to the two outer electrodes of each walker leg will have opposite polarity. Notice how in the bottom of Figure 6.2 each pulse moves one walker leg in the desired direction of motion and then after the voltages are removed the final position of the walker assembly is displaced by a small distance from its initial position.

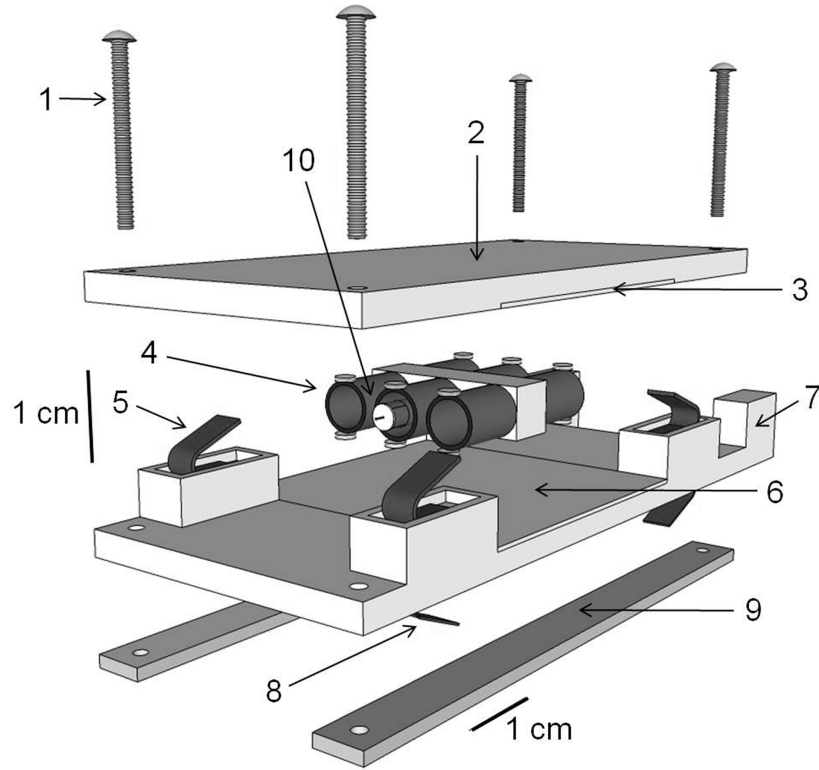


Figure 6.3: STM Assembly: 1) stainless steel screws, 2) top Macor piece, 3) top alumina plate, 4) walker assembly, 5) stiff springs, 6) bottom alumina plate, 7) bottom Macor piece, 8) soft springs, 9) stainless steel bars and 10) scanner with tip.

This STM was intentionally designed to be compact to be compatible with our existing cryogenic probe which has a 50.8 mm diameter opening. As temperature is



lowered both the magnitude of the displacements of a piezoelectric material and its strength decrease. In order to account for this loss of functionality, larger voltages need to be applied at cryogenic temperatures than at room temperature. For piezoelectric actuators to operate they need to be initially polarized by placing them in a large electric field. Therefore, there is a maximum voltage that above which there is risk of depolarizing the piezoelectric material. For the walker legs in this STM the maximum voltage is estimated to be  $V_{\max} \approx 200$  V. Since the voltage necessary to operate this STM at cryogenic temperatures exceeds  $V_{\max}$ , it was necessary to develop new electronics to drive the walker. For the mechanical actuation, it is the change in the magnitude of the applied voltage that is significant rather than the magnitude. For example, a pulse that transitions from  $-150$  V to  $+150$  V will be equivalent to a pulse that transitions from  $0$  to  $+300$  V. However the latter case will be destructive to the STM while the former never exceeds its operational limits. Therefore new electronics were developed that create 12 bipolar pulses as illustrated in Figure 6.4. Two pulses will occur simultaneously, one from  $+V$  to  $-V$  and the other from  $-V$  to  $+V$  and two consecutive pulses are separated by 6 ms. The electronics consists of a microcontroller which controls two digital-to-analog converters (DACs). The two DACs generate the low voltage waveforms necessary to create the pulses. The waveforms need to be amplified with a series of conventional and high voltage amplifiers. The pulses are created and applied to the appropriate walker legs by using a bank of solid-state relays.

As with any new instrument it was convenient to calibrate the coarse motion of this new STM. The step size is the size of the displacement of the walker assembly after one round of pulses is applied to each leg. Both the peak-to-peak voltage and the normal force dependence of the step size can be observed in Figure 6.5 for all four directions. Note that forward is the direction in which the tip will approach the sample and backward is in the opposite direction. Left and right are orthogonal to the other

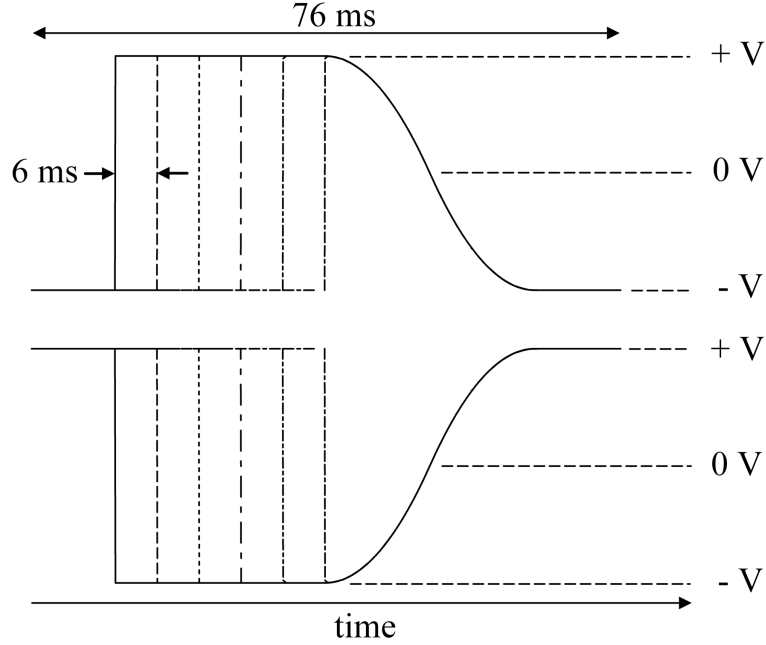


Figure 6.4: The twelve bipolar voltage pulses generated by the new electronics necessary to drive the STM at cryogenic temperatures. Pulses of appropriate polarity and timing are applied to the electrodes of the walker legs to obtain motion in a given direction.

two directions. Motion of the walker was detected by observing the motion of a small wire that was attached to the walker assembly. The wire protruded out of the STM body and could be observed with an optical microscope with a magnification of  $\times 100$ . Since the step size is below the optical limit it was necessary to take multiple steps and present the average step size. During the calibration runs, the walker assembly would traverse distances ranging from 0.25 mm to 1.0 mm in all four directions.

The inset of Figure 6.5 displays the the force dependence of the step size in all four directions: forward (+z), backward (-z), left (+x), and right (-x) represented by circles, empty circles, squares, and empty squares, respectively. The pulses utilized had a peak-to-peak amplitude of  $V_{pp} = 100$  V. The dashed lines are guides for the eyes. For slip-stick motion if the frictional force is too small, the walker legs will slip resulting in no net motion. Similarly, if the frictional force is too large the STM body will clamp down on the walker assembly inhibiting it from moving. However,

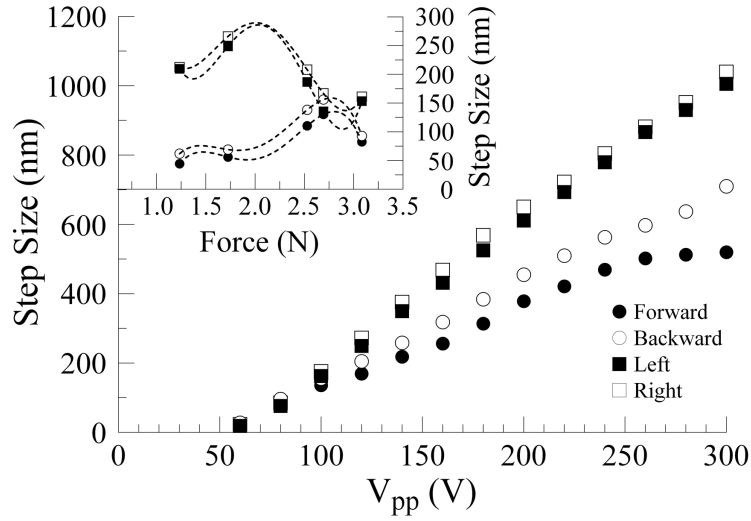


Figure 6.5: Voltage dependence of the step size in all four directions with a normal force of 2.5 N applied to the walker. (Inset) The force dependence of the the step size with  $V_{pp} = 100$  V. The dashed curves are guides for the eye.

for intermediate forces motion will be achieved with a maximum in the step size occurring in this region. Notice from the insert that the dynamics of motion along each axis is quite different. For motion along the z-axis the maximum step size occurs at  $\sim 2.75$  N, while the maximum for motion along the x-axis occurs at  $\sim 2.0$  N. For frictional forces between 1.0 N and 2.0 N the magnitude of step size along the x-axis is 3 – 4 times larger than the step size along the z-axis. Since for a force of  $\sim 2.75$  N there is a maximum in the step size for motion along the x-axis and the magnitude of the step size in all four directions are comparable this was a desirable force to operate at.

The force was then set to 2.5 N and the voltage dependence of the step size was obtained as illustrated in Figure 6.5. Since the frictional force serves as a mechanical load the Equations 3.2 and 3.1 from Part I are not applicable in this situation. Notice that there is a threshold voltage such that for pulses with an amplitude less than this

threshold will result in no motion. For pulses with an amplitude greater than this threshold voltage, the step size will have an approximately linear dependence on the pulse amplitude. Coincidentally, the threshold voltage for all four directions is  $\sim 55$  V. From Figure 6.5 the step size per volt can be determined to be 2.2, 2.8, 4.2 and 4.3 nm/V in the forward, backward, left and right directions, respectively.

## 6.2 Experiment

In order to demonstrate the long range motion of this newly constructed STM, it was used to acquire a high resolution image of an interface on the sample surface. The interface was chosen to be gold-graphite boundary which was created by thermally evaporating a 60 nm thick gold film on a freshly cleaved HOPG crystal as illustrated in the top right of Figure 6.6. This was accomplished by masking half of a HOPG crystal with mica during the evaporation process. The gold film was intentionally never annealed leaving its surface microscopically rough. Conversely, freshly cleaved HOPG forms atomically flat layers. Sample images obtained from the gold and HOPG sides of the sample can be seen in the bottom left and bottom right of Figure 6.6, respectively. Each of them is a constant current image of a  $109 \times 109$  nm<sup>2</sup> area of the sample taken with  $V_{\text{bias}} = 1.0$  V and  $I_{\text{set}} = 1.0$  nA. Both images have been given the same vertical grey scale of 16 nm to emphasize the drastically different surface roughness of each material. This allows a quick and easy determination of which side of the interface the STM tip is at. This STM is capable of producing periodic atomic structure of the HOPG side of the sample as can be seen from the top left corner of Figure 6.6. The image is a constant current image taken with  $V_{\text{bias}} = 200$  mV and  $I_{\text{set}} = 1.0$  nA. It clearly illustrates the trigonal structure expected from an STM image of HOPG. Note that two adjacent white dots are second nearest neighbors separated by 2.56 Å.

Initially an electrochemically etched tungsten tip was placed in the long range

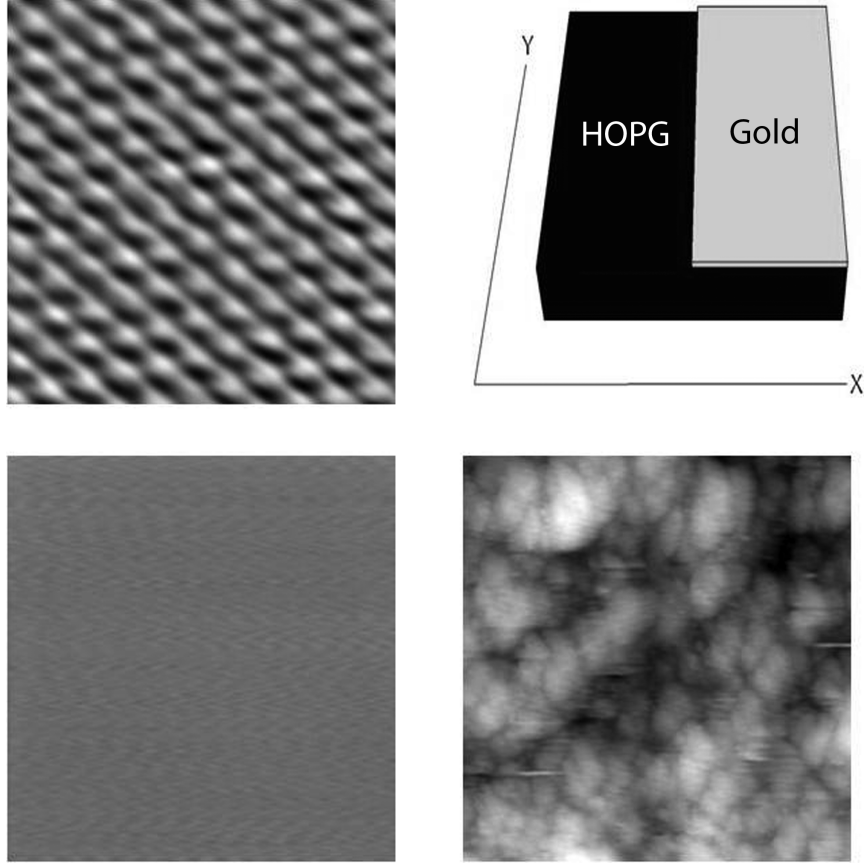


Figure 6.6: (Top left) An atomic resolution image of HOPG obtained with  $V_{\text{bias}} = 200 \text{ mV}$  and  $I_{\text{set}} = 1.0 \text{ nA}$ . (Top right) The sample configuration which consists of a substrate of HOPG with 60 nm thick gold layer on half of it. (Bottom right) An STM image of an  $109 \times 109 \text{ nm}^2$  area of the gold side of the sample taken with  $V_{\text{bias}} = 1.0 \text{ V}$  and  $I_{\text{set}} = 1.0 \text{ nA}$ . (Bottom left) An STM image of an  $109 \times 109 \text{ nm}^2$  area of the HOPG side of the sample taken with  $V_{\text{bias}} = 1.0 \text{ V}$  and  $I_{\text{set}} = 1.0 \text{ nA}$ . It has been adjusted to have the same false color scale as the gold image on the bottom right.

STM which was placed in the low temperature probe described in Part I. The probe was evacuated to a pressure of  $P \sim 10^{-7}$  torr with a turbomolecular pump, but the experiment was conducted at room temperature. Note that the sample had been exposed to ambient conditions, but both gold and HOPG surfaces are fairly inert. Care was taken to ensure that the tip was aligned with the sample, however no care was taken to ensure that it was near the interface. The tip then approached the sample until it was within tunneling range and an image was obtained. It was obvious from the image whether the STM was tunneling on the gold or the graphite side of

the sample. If the image was flat similar to the bottom left of Figure 6.6 it would be the graphite side. Conversely, if the image had a cloud-like structure similar to the bottom right of Figure 6.6 it would be the gold side of the sample. This provided the relative direction to the gold-graphite interface. To preserve the integrity of the tip it would be withdrawn and then translated  $\sim 250\mu\text{m}$  along the x-axis in the direction of the interface. This process was repeated until the interface was crossed. Once the tip traversed over the interface this process continues to be repeated but the tip is moved a smaller horizontal distance. After repeating this process numerous times it is possible to zero in on the gold-graphite interface and produce high-resolution STM images of the boundary.

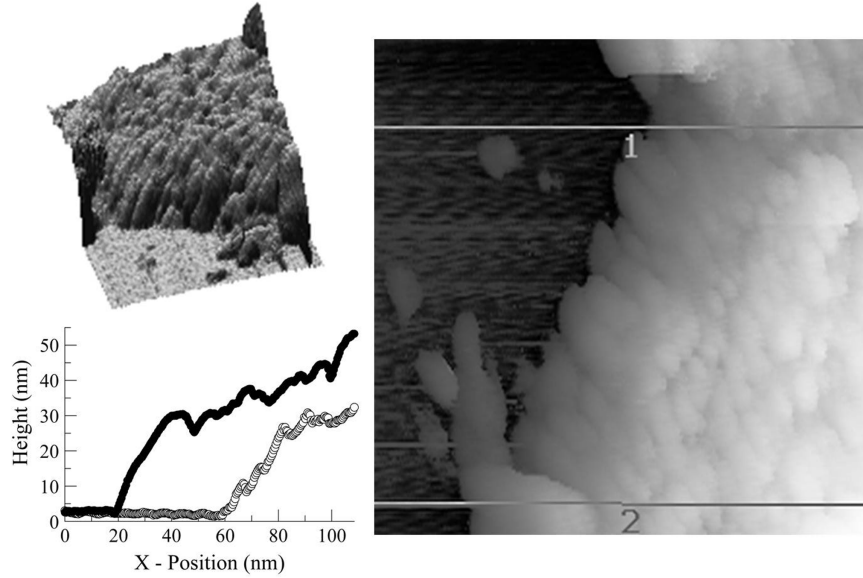


Figure 6.7: All images represent data obtained from a  $109 \times 109 \text{ nm}^2$  area of the sample near the gold-graphite interface obtained with  $V_{\text{bias}} = 1.0 \text{ V}$  and  $I_{\text{set}} = 1.0 \text{ nA}$ . (Top left) A three-dimensional image with the flat HOPG region nearest to the viewer. (Right) A two-dimensional image with a non-linear false color scale to emphasize the interface. (Bottom left) Two line profiles taken from the data with line 1 represented by unfilled circles and line 2 by filled circles.

An example of an image of the gold-graphite interface is presented in Figure 6.7. Note that all three images in the figures were obtained from the same data set and are presented in a slightly different manner. From the two-dimensional picture on the

right side, one can clearly see a large flat region on the left which is the graphite and a region elevated above it on the right side which is the gold. In order to emphasize features on each side of the step, a nonlinear grey scale was used. A consequence of this is it highlights the electrical noise on the graphite side of the sample. However it also emphasizes the cloud-like structure on the right hand side which is characteristic of an unannealed gold surface. The shape of the interface can be more clearly seen in the three-dimensional image in the upper left corner of Figure 6.7. In this image, it is rotated such that the graphite site is closest to the viewer. Notice that the graphite is very smooth and the interface is very sharp. This can also be seen in the two line profiles plotted in the bottom left of Figure 6.7. Line 1 and line 2 from the two-dimensional image is represented by unfilled and filled circles respectively. From this data it is clear that the thickness of the gold film measured with the STM is in good agreement with the actual thickness of the film. For this example, the site where the STM initially approached the sample was  $\sim 520 \mu\text{m}$  from the interface.

## PART III

### Investigations of voltage induced torsional strain in TaS<sub>3</sub>



## Chapter 7 Background of TaS<sub>3</sub>

In the 1950's Rudolf Peierls and Herbert Fröhlich theoretically predicted that a one dimensional electron gas with phonon interactions will be unstable at low temperatures. This instability would be a metal-to-insulator transition (MIT). In other words as the temperature is lowered, the electrical transport properties of the one dimensional system would undergo a sharp transition from a metallic state to an insulating one at a critical temperature ( $T_P$ ). This transition temperature is commonly referred to as the Peierls temperature. This phenomenon is due to distortions in the crystal lattice. This distortion will create a modulation in the electron density called a charge density wave (CDW). A consequence of a CDW is an energy gap is opened near the Fermi energy. Since all states below the gap are filled and the ones above are empty, these materials will be insulators.

This is illustrated in Figure 7.1 where the crystal structure and the energy dispersion for a one-dimensional system is shown. Panel a) displays the system being metallic for  $T > T_P$  while panel b) shows the system being insulating when  $T < T_P$ . Notice that when the system is metallic, all atoms are equally spaced by the lattice parameter  $a$  and the electron density  $\rho(r)$  is constant. However, when the temperature is lowered below  $T_P$  there is a lattice distortion. For this example, atoms shift so they are closer to some nearest neighbors and further from others as shown in Figure 7.1 b). This results in a larger unit cell with a lattice parameter  $2a$ . This distortion in the crystal lattice creates a modulation in the electron density. This leads to a gap opening near the Fermi momentum ( $k_F$ ) which can be clearly seen in the energy dispersion displayed in Figure 7.1 b). A consequence of this gap is the system will be in an insulating state.

Although the theories of Peierls and Fröhlich are interesting and important to

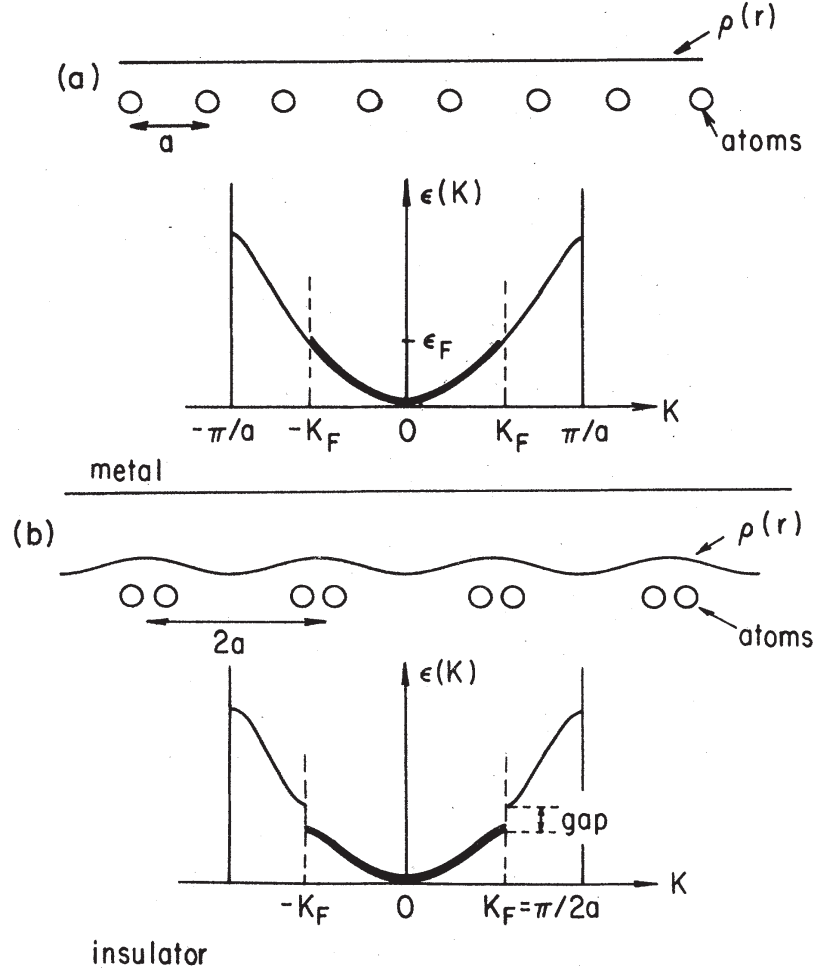


Figure 7.1: a) Atomic structure (top) and energy dispersion (bottom) for a one-dimensional system for  $T > T_P$ . b) Atomic structure and energy dispersion for  $T < T_P$  [61].

fundamental science, it was believed that such materials would never be realized in macroscopic crystals due to all crystals having a three dimensional structure. Remarkably in the 1970's structural deformations due to CDWs were observed through x-ray scattering in the quasi-one dimensional materials  $K_2Pt(CN)_4 \cdot 0.3Br \cdot xH_2O$  (KCP) [62] and TTF-TCNQ [63, 64]. These materials are respectively an inorganic conductor and an organic charge transfer salt. The term "quasi-one dimensional" or "quasi-low dimensional" refers to a three dimensional material which is highly anisotropic. The electrical transport properties for the different spatial dimensions in these ma-

materials can differ by several orders of magnitude making them approximately one-dimensional.

Since CDW conductors were first realized, this phenomenon has been observed in numerous materials including  $\text{NbSe}_3$  [65],  $\text{NbS}_3$  [66],  $\text{TaS}_3$  [67],  $\text{K}_{0.3}\text{MoO}_3$  [68, 69],  $\text{Rb}_{0.3}\text{MoO}_3$  [70] and  $(\text{TaSe}_4)_2\text{I}$  [71]. The high anisotropy of these materials is due to their crystal structures which consists of a series of parallel chains. The electrical conductivity along these chains is very high in comparison to the conductivity between adjacent chains. The chains of  $\text{NbSe}_3$  can be seen in Figure 7.2. In this figure, the Nb and Se atoms are represented by filled and empty circles respectively. In addition to the strong anisotropy, CDWs exhibit some extremely exotic properties such as non-ohmic electrical conductivity, novel elastic properties and huge dielectric constants.

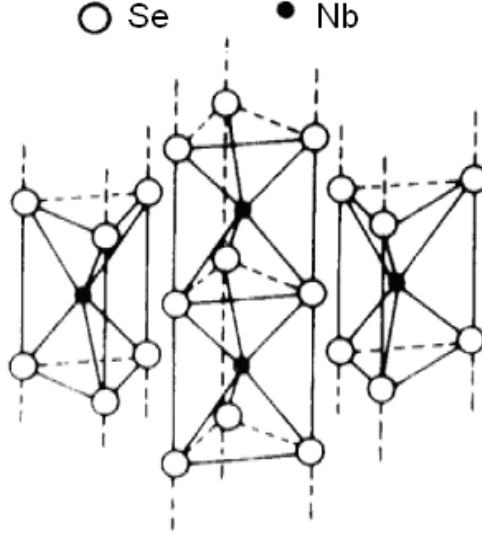


Figure 7.2: a) Crystal structure of  $\text{NbSe}_3$ . The Nb and Se atoms are represented by filled and unfilled circles respectively [72].

The example shown in Figure 7.1 is an over simplified case. In this example the wavelength of the charge modulation  $\lambda_\rho$  is equal two times the lattice parameter  $a$  resulting in a commensurate CDW. In general, if the ratio  $\lambda_\rho/a$  is a rational number the CDW is commensurate. Conversely, the CDW will be incommensurate if the

ratio is irrational. Most CDW systems are commensurate. Incommensurate CDWs occur due to inequivalent chains and inter-chain coupling. All sliding CDWs are incommensurate. Assuming the z-axis is parallel to the crystal chains, the charge density  $\rho(z)$  will be modeled by:

$$\rho(z) = \rho_0 + \rho_1 \cos(qz + \phi(z)) \quad (7.1)$$

where  $\rho_0$ ,  $\rho_1$ ,  $q$  and  $\phi(z)$  are a constant, the amplitude of the CDW modulation, the wavevector and the position dependent phase respectively. Any crystal will have defects and impurities in the lattice. For many CDW systems the phase of the CDW will adjust itself such that a maximum or minimum in the charge density occurs at the defect or impurity. As a result the CDW will be “strongly” pinned to the underlying lattice. Lee and Rice (Ref. [73]) showed that in some systems,  $\phi(z)$  will gradually adjust itself to variations in the impurity concentration of the lattice. This is referred to as “weak” pinning. In 1976 it was shown by Monçeau *et. al.* that if a large enough electric field is applied to crystals of NbSe<sub>3</sub>, the weakly pinned CDW will be depinned from the underlying lattice and slide through the crystal carrying current [65]. The threshold field (voltage) at which the CDW is depinned is labeled  $E_T$  ( $V_T$ ). This sliding CDW phenomenon has since been observed in other systems such as TaS<sub>3</sub> and K<sub>0.3</sub>MoO<sub>3</sub>.

TaS<sub>3</sub> has a Peierls temperature of  $T_P = 220 \text{ K}$  and a crystal structure similar to NbSe<sub>3</sub> which is illustrated in Figure 7.2. It exhibits non-ohmic conductivity and a voltage induced decrease in its Young’s modulus and shear modulus. More recently, in 2007 Pokrovskii *et. al.* discovered an exotic torsional piezo-like response in single crystals of TaS<sub>3</sub> [74]. In this thesis, I present our work observing and investigating the origin this unique phenomenon called voltage induced torsional strain (VITS).

There are two known polytypes of TaS<sub>3</sub>, orthorhombic (o-TaS<sub>3</sub>) and monoclinic (m-TaS<sub>3</sub>) [75]. All the results and discussions below are specifically related to the

physical properties of the orthorhombic polytype. So note that all references to TaS<sub>3</sub> in this thesis directly imply o-TaS<sub>3</sub>.

The exact crystal structure of TaS<sub>3</sub> is yet to be determined due to the large number of defects present [76]. It does have a structure similar to other transition metal trichalcogenides (MX<sub>3</sub>) such as NbSe<sub>3</sub>. It has been proposed that the unit cell will consist of 24 different chains similar to the individual chains of NbSe<sub>3</sub> as shown in Figure 7.2 [77].

## 7.1 Resistance

As the temperature in TaS<sub>3</sub> decreases, it will transition from a metallic to an insulating state. This behavior is clearly illustrated in the temperature dependence of the resistance for sample E shown in Figure 7.3 a). Notice that for temperatures below the Peierls temperature of  $T_P \sim 220$  K, the resistance begins to rapidly rise from a few hundred ohms to several thousand ohms. The thermal excitation gap in the material can be obtained by fitting the resistance data to an Arrhenius model:

$$R(T) = R_0 \exp\left(\frac{\Delta}{k_B T}\right) \quad (7.2)$$

where  $\Delta$  is the excitation gap,  $R_0$  is a constant,  $k_B$  is the Boltzmann constant and  $T$  is the temperature. This is used to fit the low temperature data as displayed in Figure 7.3 b) as a solid black line. For sample E the measured gap is approximately  $2\Delta \sim 1583$  K  $\sim 137$  meV. The values of  $2\Delta$  for all the samples discussed are presented in Table 8.1. The insulating gap in this material should be intrinsic to the material but notice there is a slight sample dependence in the activation energy. This is due to defects in the crystal driving the Fermi energy away from the center of the gap.

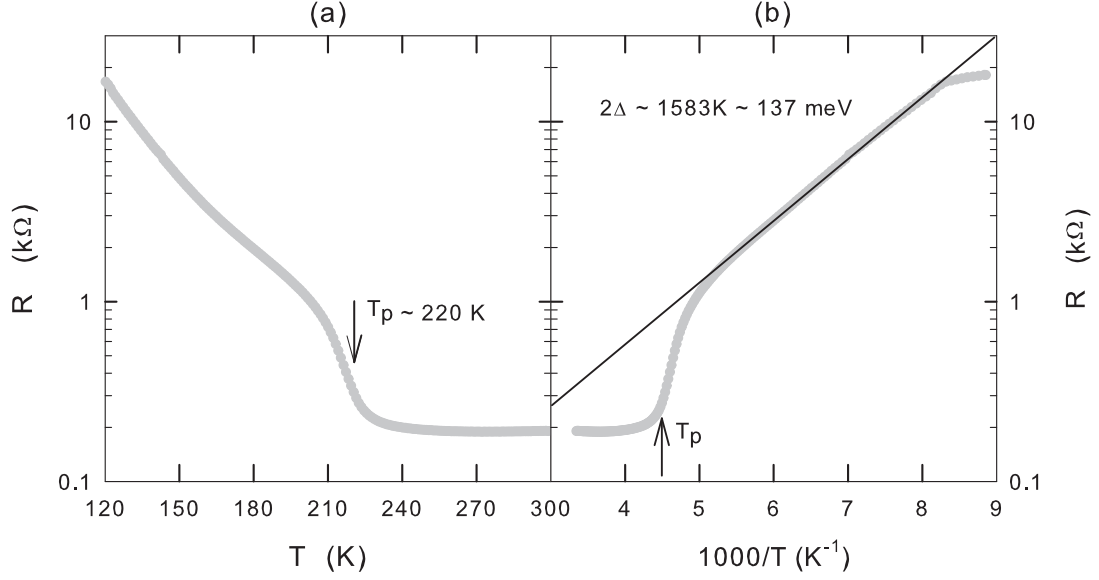


Figure 7.3: Temperature dependence of the resistance of TaS<sub>3</sub> (Sample E). The line in b) is a fit to Equation 7.2.

## 7.2 Elastic Properties

In the mid 1980's, it was shown through vibrating reed measurements that in single crystals of TaS<sub>3</sub> there is a voltage induced decrease in the Young's modulus ( $Y$ ) by  $\sim 2\%$  [78, 79]. This effect was shown to be due to CDW depinning. It was then discovered the the shear modulus ( $G$ ) also decreased when the CDW was depinned [80]. However the change in  $G$  is  $\sim 25\%$ , making it a much larger effect. These elastic anomalies suggest that the pinning of the CDW to the underlying crystal lattice is correlated to interchain coupling. Whenever the CDW is depinned, the interactions between adjacent chains decrease allowing for smaller elastic moduli. For both cases, the anomaly commences at  $V_T$  and as the respective moduli decrease, there is also an increase in the internal friction. The internal friction for the shear compliance ( $J = 1/G$ ) or shear modulus is:

$$(\text{Internal Friction}) = \tan \delta = \frac{\text{Im}(J)}{\text{Re}(J)} = -\frac{\text{Im}(G)}{\text{Re}(G)} \quad (7.3)$$

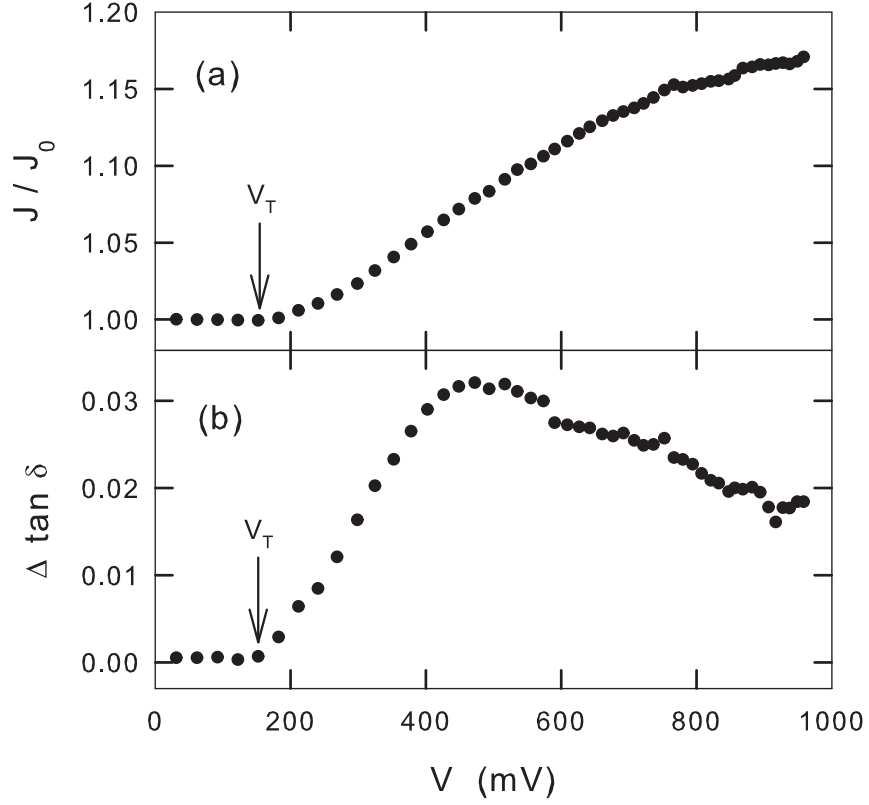


Figure 7.4: Voltage dependence of a) shear compliance ( $J=1/G$ ) and b) internal friction ( $\tan \delta$ ) for sample E. The depinning threshold is marked with vertical arrows.

Note that the Young's modulus will obey the same equation by replacing  $G$  with  $Y$ . The voltage dependence of the shear compliance and the internal friction for sample E is displayed in Figure 7.4. Note that  $J_0$  is defined to be the zero voltage response of the shear compliance response ( $J_0 \equiv J(V = 0)$ ). Notice how both begin to increase at  $V_T \sim 180$  mV, however the shear compliance continues to rise while the internal friction rapidly increases and then slowly decreases for  $V > 470$  mV. The increase in the shear compliance is smaller than 25% due to its mounting configuration which will be discussed below.

### 7.3 Voltage Induced Length Changes

In 1992, Hoen *et. al.* discovered that  $\text{TaS}_3$  crystals would have voltage induced changes in its overall length [81]. Their results are displayed in Figure 7.5. They discovered that this motion has a hysteretic voltage dependence. This response would commence at voltages slightly below threshold and then saturates at voltages slightly above threshold. The relative length change is  $\Delta L/L \sim 10^{-6}$  with relaxational time constants of  $\sim 10$  s. They proposed that these changes were due to changes in the CDW near  $V_T$  coupling to the underlying lattice changing the overall length of the sample.

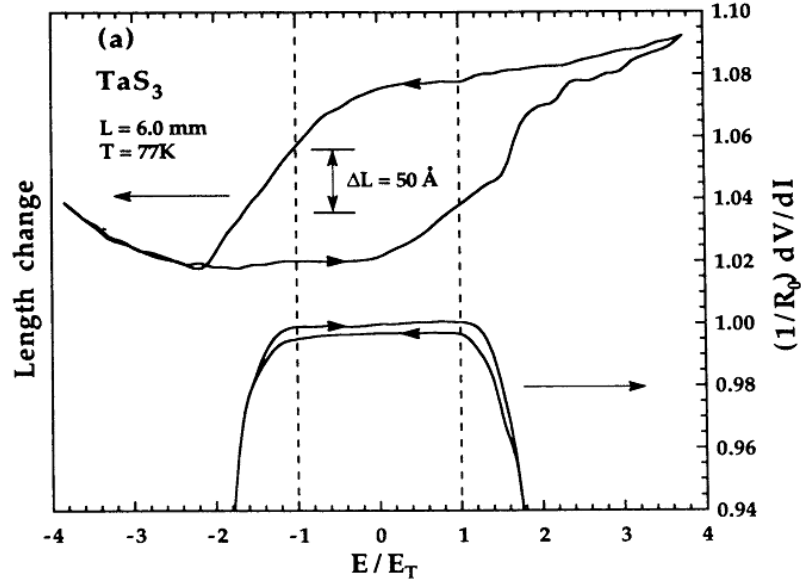


Figure 7.5: Voltage dependence of the change in overall length of the  $\text{TaS}_3$  crystal (top) and relative change in resistance (bottom) [81].

Itkis *et.al.* (Reference [82]) showed that the electrical contacts can affect the CDW. Figure 7.6 presents the position dependence for both the CDW phase ( $\phi = \frac{dq}{dz}$ ) and the change in the CDW wave vector ( $\Delta q$ ) in CDW crystal. Notice that in the center of the sample, there are no changes in either  $\phi$  or  $\Delta q$ . However, near both contacts  $\phi$  increases while  $\Delta q$  increases near the positive contact and decreases near



the negative one. These responses are approximately symmetric about the center of the crystal, but there is a slight asymmetry. The asymmetry can be seen in the response being slightly larger near the negative contact than it is near the positive contact. I will discuss in greater detail below how this asymmetry gives rise to the voltage induced length changes.

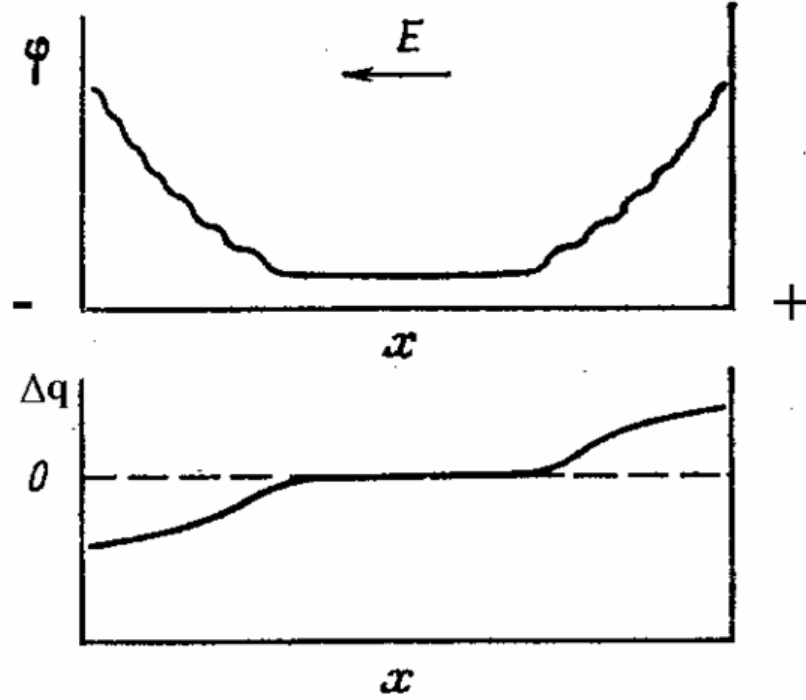


Figure 7.6: The position dependence the CDW phase ( $\phi = \frac{dq}{dz}$ ) and the change in the CDW wave vector ( $\Delta q$ ) [82].

## Chapter 8 Experimental Setup

In order to measure the voltage induced torsional strain (VITS), it is necessary to measure small rotations of  $\sim 1^\circ$  in the narrow ribbon shaped crystals of TaS<sub>3</sub> at cryogenic temperatures. If a steel bar is attached to the crystal such that it is perpendicular to the crystal, linear displacements of the bar can be measured to represent the twist angle. Assuming the steel bar is attached to its center as in Figure 8.1 and the twist angles are small, the linear displacement of the free end of the steel bar ( $\Delta s$ ) will be:

$$\Delta s = \frac{L}{2} \Delta \phi \quad (8.1)$$

where  $L$  is the overall length of the steel bar and  $\Delta \phi$  is the twist angle. For a steel wire with  $L = 1$  mm, the linear displacement per unit angle will be  $\Delta s / \Delta \phi \sim 10 \mu\text{m}/\text{degree}$ . In order to measure displacements of this magnitude, a helical resonator [83] is utilized. Two distinct advantages of a helical resonator is it is very compact enabling it to easily fit inside a cryogenic dewar and the resonant frequency of the RF cavity is extremely sensitive to mechanical changes near the free end of the helix which serves as the transducer. So if the steel wire attached to the sample is placed in close proximity to the transducer, as in Figure 8.2, the resonant frequency of the cavity will be highly sensitive to microscopic changes in changes in the separation between the steel wire and the transducer as the sample twists.

### 8.1 Sample Configuration

To measure the VITS response in TaS<sub>3</sub>, the sample must be mounted with electrical contacts on each end with one end mechanically free to rotate. Two methods of mounting the long narrow TaS<sub>3</sub> crystals has been used and are illustrated in Figure

8.1. The first method shown in a) has the free end of the  $\text{TaS}_3$  crystal connected with silver epoxy to a  $\text{NbSe}_3$  crystal and a magnetized steel wire which are respectively parallel and perpendicular to the  $\text{TaS}_3$  crystal. The two ends of the overall assembly are then rigidly mounted to a sample holder with silver paint and placed such that the steel wire is  $\sim 100 \mu\text{m}$  from the transducer that is the end of the helix in the RF cavity. The steel wire is magnetized in order for applied external magnetic fields to twist the crystal. This enables the electronics to be calibrated and to apply external torques to the sample. Since  $\text{NbSe}_3$  remains metallic at  $T = 77 \text{ K}$ , the voltage drop across it should be negligible at this temperature. A consequence of the  $\text{NbSe}_3$  is it serves as a torsional spring in parallel with the  $\text{TaS}_3$  and will decrease the overall response of the system.  $\text{TaS}_3$  and  $\text{NbSe}_3$  have comparable elastic constants. Therefore the amount of attenuation depends primarily on the relative lengths and cross-sections of the two crystals. Since VITS depends on depinning of the CDW, a more robust mounting technique illustrated in panel b) was developed. For this method a thin film of gold ( $\sim 20 \text{ nm}$ ) was thermally evaporated on half of the crystal [84]. This will hold this half of the crystal at the same electrical potential keeping the CDW pinned on this side. This results in the VITS response being roughly half of its full response. The magnetic wire serves the same purpose in this case but is attached after the  $\text{TaS}_3$  crystal is mounted to the sample holder.

The results from seven different  $\text{TaS}_3$  samples will be presented. These samples are labeled sample A – G. The physical dimensions, electrical resistance and torsional resonant frequency of these samples is displayed in Table 8.1. Samples A and B were assembled with  $\text{NbSe}_3$  and the others with the thin gold film. For samples C – G, the length presented is the length of the crystal without gold (i.e. the length of the crystal responsible for the observed VITS). The total length of the crystal is roughly double this length. The steel wire typically had a diameter of  $25 \mu\text{m}$  and ranged from  $1 - 3 \text{ mm}$  in length. The torsional resonant frequency of the sample would depend

Sample	$l$ (mm)	$w$ ( $\mu\text{m}$ )	$t$ ( $\mu\text{m}$ )	$R$ (k $\Omega$ )	$f_{\text{res}}$ (Hz)	$2\Delta$ (meV)
A	$\sim 2$	$\sim 10$	$\sim 4$	57	100	137
B	$\sim 2$	$\sim 10$	$< 2$	134	$\sim 30$	126
C	$\sim 2.5$	$\sim 15$	$\sim 4$	$\sim 35$	$\sim 560$	135
D	$\sim 2.5$	$\sim 15$	$\sim 4$	$\sim 35$	$\sim 800$	135
E	$\sim 2$	$\sim 10$	$\sim 2$	90	$\sim 100$	137
F	$\sim 2$	$\sim 10$	$\sim 2$	$\sim 66$	$\sim 100$	143
G	$\sim 2$	$\sim 10$	$\sim 2$	$\sim 24$	730	141

Table 8.1: Physical properties of the seven TaS<sub>3</sub> samples used, where  $l$ ,  $w$  and  $t$  are the length, width and thickness of the crystal respectively.

strongly on the length of the steel wire.

## 8.2 RF Cavity

Inside the RF cavity is the helical coil with the steel wire that is attached to the sample in close proximity to it. The helical coil and steel wire can be modeled as an LC circuit. Recall that the electrical impedance of an inductor and capacitor are  $i\omega L$  and  $1/(i\omega C)$ , respectively, where  $\omega$  is the angular frequency and  $L$  is the inductance of the coil. The capacitance will be  $C = C_0 + C_1(d)$ , where  $C_1(d)$  is the capacitance that forms with the steel wire and the transducer being separated by a distance  $d$ , while  $C_0$  is the constant capacitance between the transducer and the remainder of the cavity. There will be an electrical resonance ( $\omega_r$ ) that occurs when the two impedances are equal in magnitude. The value of  $\omega_r$  will be governed by:

$$\omega_r^2 = \frac{1}{LC} \quad (8.2)$$

The dependence of the resonant frequency of the RF cavity on the separation between the transducer and the steel wire will be:

$$\frac{\Delta\omega_r}{\omega_r} = -\frac{1}{2} \frac{d \ln C}{d d} \Delta d \quad (8.3)$$

Therefore if the sample twists such that the steel wire moves away from the transducer,  $\omega_r$  will increase. Similarly, if it moves closer to the transducer,  $\omega_r$  will decrease.

The RF Cavity has a resonant frequency of approximately 430 MHz and a quality factor ( $Q = \omega_r / \Delta\omega$ ) of about 300, where  $\Delta\omega$  is the bandwidth of the resonant peak. A block diagram for the experimental setup can be seen in Figure 8.3. The circuit consists of an RF signal that is either frequency (FM) or phase (PM) modulated, the RF cavity, a demodulation circuit, a lock-in amplifier and a computer to record the data. The demodulated output will be related to the distance between the steel wire and the transducer and thus the twist angle of the crystal. For small twists, the output signal will be approximately proportional to the twist angle.

The RF generator and the low frequency function generator used for the modulated RF signal are both commercially available devices. The demodulation circuit is home built and the lock-in amplifier is also a commercially available instrument. Near resonance the RF cavity will be a quarter wave cavity. [80]

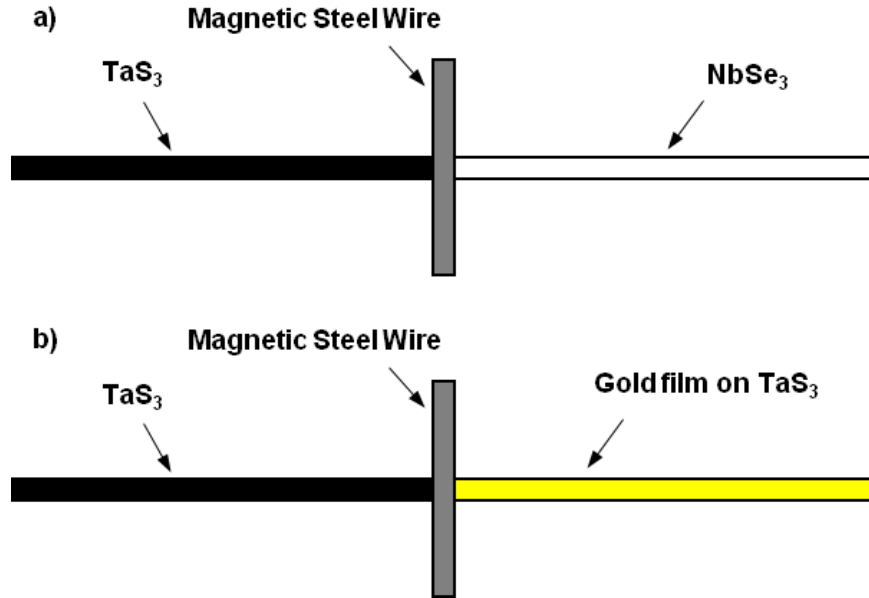


Figure 8.1: a) Original sample mounting method with a TaS<sub>3</sub> and NbSe<sub>3</sub> crystal connected at a steel wire. b) More robust configuration with a thin gold film on a single TaS<sub>3</sub> crystal with a steel wire attached at its center [84].

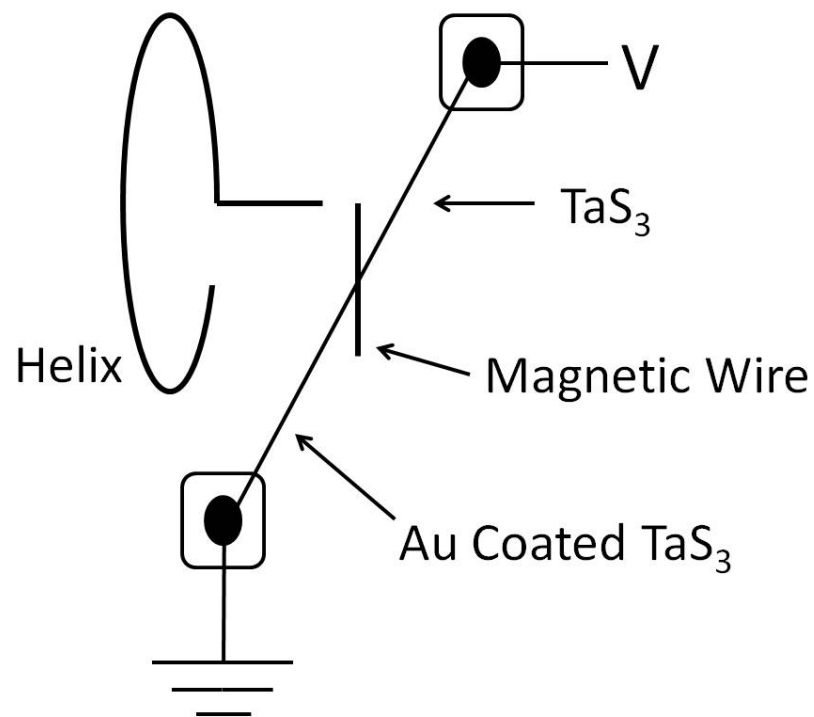


Figure 8.2: Configuration of sample relative to the helix. Both sample types are mounted this way.

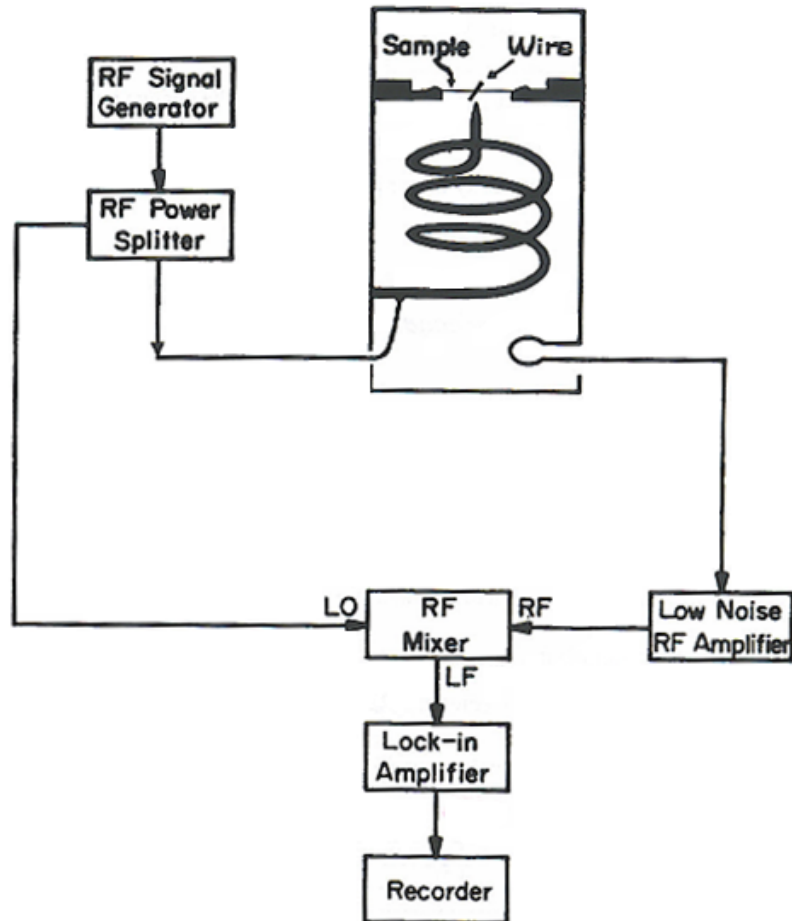


Figure 8.3: Block diagram of the experimental setup including the electronics and RF cavity. [85]

### 8.3 PM Technique

#### 8.3.1 Phase Modulation

For phase modulation (PM) the modulated output of the RF cavity can be represented mathematically by:

$$V_{mod} = \cos(\omega t + \phi) \quad (8.4)$$

where  $\omega$  is the frequency of the RF carrier and  $\phi$  is the phase which is modulated at a frequency of  $\Omega$  and with an amplitude of  $\phi_0$  represented by:

$$\phi = \phi_0 \cos(\Omega t) \quad (8.5)$$

The modulation occurs in the RF cavity and the modulated output is then sent to a mixer. The mixer multiplies  $V_{mod}$  by the unmodulated input  $V_{in} = \cos(\omega t + \frac{\pi}{2})$  and then averages this product over the period  $T_\omega$ . The unaveraged output of the mixer will be:

$$V_{mix} = \cos(\omega t + \phi) \cos(\omega t + \frac{\pi}{2}) \quad (8.6)$$

Utilizing trigonometric identities this expression will reduce to:

$$V_{mix} = [\cos(\omega t) \cos(\phi) - \sin(\omega t) \sin(\phi)][-\sin(\omega t)] \quad (8.7)$$

Since  $\phi_0 \ll 1$ , to first order in  $\phi_0$ ,  $\cos(\phi) \approx 1$  and  $\sin(\phi) \approx \phi$ . Utilizing this assumption  $V_{mix}$  can be further simplified to:

$$V_{mix} = [-\cos(\omega t) \sin(\omega t) + \sin^2(\omega t) \phi] \quad (8.8)$$



The averaging results in the first term vanishing and the  $\sin^2(\omega t)$  term averaging to 1/2. Therefore the output of the mixer will be:

$$V_{mix} = \frac{1}{2} \phi_0 \cos(\Omega t) \quad (8.9)$$

Notice that the demodulated output of the RF cavity will be proportional to  $\phi_0$ , the modulation amplitude. In experiments, the PM is obtained by rocking the sample at a frequency  $\Omega$ . This is accomplished either by applying an external AC magnetic field or by applying a square wave voltage directly to the TaS<sub>3</sub> crystal. Rocking the sample while holding the RF cavity at its electrical resonance will modulate the phase. Therefore  $\phi_0$  will be proportional to the magnitude that the crystals are twisted.

### 8.3.2 Shear Compliance

The shear compliance (J) is the inverse of the shear modulus (1/G). The experiments measuring J were similar to those conducted by Zhan *et. al.* [86, 87, 85]. The main difference is our response is attenuated by the NbSe<sub>3</sub> or the portion of the crystal electrically shorted by the gold film. This measurement is critical because  $V_T$  can be obtained much more cleanly from shear compliance data rather than from the resistance curves. The shear compliance is obtained by applying an AC torque to the sample. This is accomplished by applying a small AC magnetic field with a Helmholtz coil that is attached to the tail of the dewar. The magnetic field is typically driven with a 10 Hz sine wave. The lock-in amplifier will be tuned to the modulation frequency that is driving the magnet. The demodulated output of the lock-in tuned to the fundamental frequency will have an in-phase term that is proportional to the amplitude of the rotation of the steel wire. In addition there is a quadrature term that is related to a time delay in the response due to internal friction in the sample.

### 8.3.3 Square Wave Response

#### Voltage/Frequency Domain

In order to fully understand the VITS response, it is necessary to study its dynamics. In order to accomplish this a bipolar square wave with a peak-to-peak amplitude of  $2V_{\text{square}}$  is applied to the sample. The effect of this is that the sample should yield no response for  $V_{\text{square}} < V_T$  while the sample should rapidly rock from one twist position to another for  $V_{\text{square}} > V_T$ . Similar to the J measurement, the lock-in amplifier is tuned to the fundamental frequency of  $V_{\text{square}}$ . The in-phase signal ( $V_{\text{IP}}$ ) will be related to the amount the sample is twisting while the quadrature ( $V_{\text{quad}}$ ) is related to the time delay in the VITS response. This response can be plotted with respect to  $V_{\text{square}}$  or frequency. The voltage domain is easier to obtain, but the response in the frequency domain can have the dynamics extracted by fitting the data to an appropriate relaxation model.

#### Time Domain

It is also possible to acquire the time dependence of the square wave response. For these experiments,  $V_{\text{square}}$  is still applied to the sample as above, however an FM signal is applied to the cavity, which will be described in greater detail below. The lock-in is tuned to the fundamental frequency of the FM and only  $V_R = \sqrt{V_{\text{IP}}^2 + V_{\text{Quad}}^2}$  is collected [86]. This signal is directly related to the static twist angle of the crystal. The time constant of the lock-in  $\tau_{\text{LI}}$  is chosen such that  $T_{\text{FM}} \ll \tau_{\text{LI}} \ll T_{\text{square}}$ , where  $T_{\text{square}} = 1/f_{\text{square}}$  is the period of the square wave applied to the sample and  $T_{\text{FM}} = 1/f_{\text{FM}}$  is the period of the frequency modulation. This enables the lock-in amplifier to serve as a low pass filter. This data is collected with a digital oscilloscope. Depending on the value of  $\tau_{\text{LI}}$  chosen, there still may be appreciable 60 Hz and RF noise in the signal. This noise can be eliminated by carefully choosing  $f_{\text{square}}$  such

that it is not a sub harmonic of the noise. This allows the response to be numerically averaged by the oscilloscope. Care was always taken to ensure that multiple periods were acquired simultaneously giving confidence in the reproducibility of the VITS signal.

### 8.3.4 Induced EMF

Since VITS is a piezo-like response, it was logical to investigate whether an induced stress would induce an emf. This measurement was similar the the J measurement which rocked the sample with a small AC magnetic field while applying a DC voltage across the sample. The lock-in is still tuned to the fundamental modulation frequency of the magnetic field, however the input is connected directly to the sample instead of the output of the RF cavity. So we investigated whether the stresses applied from the magnetic field would induce a voltage at the same frequency the sample was modulated at.

## 8.4 Hysteresis Loops

### 8.4.1 Frequency Modulation

For frequency modulation (FM) the generated voltage that is fed into the RF cavity can be represented mathematically by:

$$V_{in} = \cos(\omega t + \phi) \quad (8.10)$$

where  $\phi$  is the phase and the frequency  $\omega$  is modulated by an amplitude of  $\alpha$  at a frequency of  $\Omega$  represented by:

$$\omega = \omega_c + \alpha \cos(\Omega t) \quad (8.11)$$

where  $\omega_c$  is the unmodulated frequency of the RF carrier. Using a mathematical progression similar to that associated with PM the output of the mixer from FM can be shown to be:

$$V_{mix} = \frac{1}{2}(\alpha t)\cos(\phi)\cos(\Omega t) \quad (8.12)$$

For FM the demodulated output will depend on both  $\alpha$  and  $\phi$ . In experiment, the static twists of the TaS<sub>3</sub> crystal will change the resonant frequency of the cavity and will in general change both  $\alpha$  and  $\phi$ . In order to maximize the response, it is necessary to work slightly off resonance. The largest change in  $\alpha$  will typically occur at one of the  $-1.5$  dB points [86]. Care can be taken to provide an appropriate phase shift to the output of the cavity that will make the phase dependence of this response negligible. Under these conditions the output of the RF cavity will be proportional to the static twists of the sample. The main advantage of this technique is it does not require the sample to be modulated, however it is more susceptible to external mechanical noise.

#### 8.4.2 Static technique

These static FM experiments were performed by applying a DC voltage to the sample. The static VITS response of TaS<sub>3</sub> will be proportional to the demodulated output of the RF cavity. This allows for the voltage dependence of this response to be acquired. The modulation would typically have a frequency of 40 kHz and an amplitude of 20 kHz. In order to maximize the static FM response, it was necessary to work with the RF cavity slightly off resonance. The maximum FM response typically occurs at a frequency displaced from the resonance by  $\pm(0.5 - 0.7)$  MHz. The DC voltage applied to the sample would be swept in a loop to observe hysteretic dependence of twist angle on applied voltage for TaS<sub>3</sub>. A single measurement typically took approximately 30 – 45 minutes to acquire. The nature of modulation techniques

typically provides results with great relative resolution presented in arbitrary units. Ultimately we were able develop a rough method of normalizing the VITS response to absolute units. However this normalization is only approximate.

### **8.4.3 Dynamic technique**

The static technique is incredibly sensitive to small changes in the resonant frequency of the cavity. These changes are not always due to the VITS response we are investigating. For example, artifacts such as motion of the steel wire not due to VITS or drift in the electronics will also contribute to the FM response. The amount of time necessary to acquire a single static hysteresis loop makes it difficult to acquire loops independent of artifacts. A technique similar to the square wave time domain response described above can be utilized in order to both speed up the acquisition time and to adjust for the small changes in the resonance of the cavity. In this case a triangle waveform is applied to the sample and both the triangle reference signal and the VITS signal need to be collected with the digital oscilloscope. So at each instant in time, we have a torsional response and an applied voltage. These two signals can be plotted with respect to one another creating hysteresis loop similar to the static loops described above. Another advantage of this technique is the frequency dependence of the hysteresis loops can be obtained. The total acquisition time for hysteresis loops acquired with this technique varies with frequency and typically ranges between 30 s and 180 s.

## Chapter 9 Voltage Induced Torsional Strain in TaS<sub>3</sub>

In 2007, Pokrovskii *et. al.* discovered a unique effect in TaS<sub>3</sub> called Voltage Induced Torsional Strain (VITS) [74]. This is a piezo-like effect that when a large potential difference is applied across the two ends of these ribbon shaped crystals, the crystal will rotate about its axis of symmetry. This phenomenon can be seen on the right side of Figure 9.1. The bottom graph displays the electrical resistance along the z-axis of the crystal plotted with respect to the applied current. The importance of this curve is to obtain the threshold current ( $I_T = V_T/R_0$ ) which is the current the CDW becomes depinned, where  $R_0$  is the ohmic resistance. For this sample  $I_T \approx \pm 2 \mu\text{A}$ . The curves above this display the twist angle of the sample also plotted with respect to the applied current. Initially  $I = 0 \mu\text{A}$  and the current is lowered. Once  $I$  is less than  $-2 \mu\text{A}$  the sample will twist and stay approximately in this configuration until the current exceeds  $+2 \mu\text{A}$ . Now the sample twists in the opposite direction and remains in this configuration until once again the current is lowered below  $-2 \mu\text{A}$ . This shows that the VITS in TaS<sub>3</sub> is hysteretic, is coupled to the CDW current and has an amplitude of approximately  $1^\circ$ .

In order to measure the VITS response, the sample must be mounted such that there are electrical contacts on both ends with only one end rigidly mounted allowing the other end to rotate freely. They accomplished this challenge by attaching a small BSCCO wire to the free end of the crystal as shown in the left panel of Figure 9.1. In addition, several small BSCCO wires a few hundred micrometers long were attached to the crystal to serve as mirrors. The rotation of the crystal was measured by measuring changes in a laser which was reflected off these small mirrors.

Initially it was critical to confirm the effects observed by Pokrovskii *et. al.* with the low temperature helical resonator setup. Loops were acquired by sweeping a DC

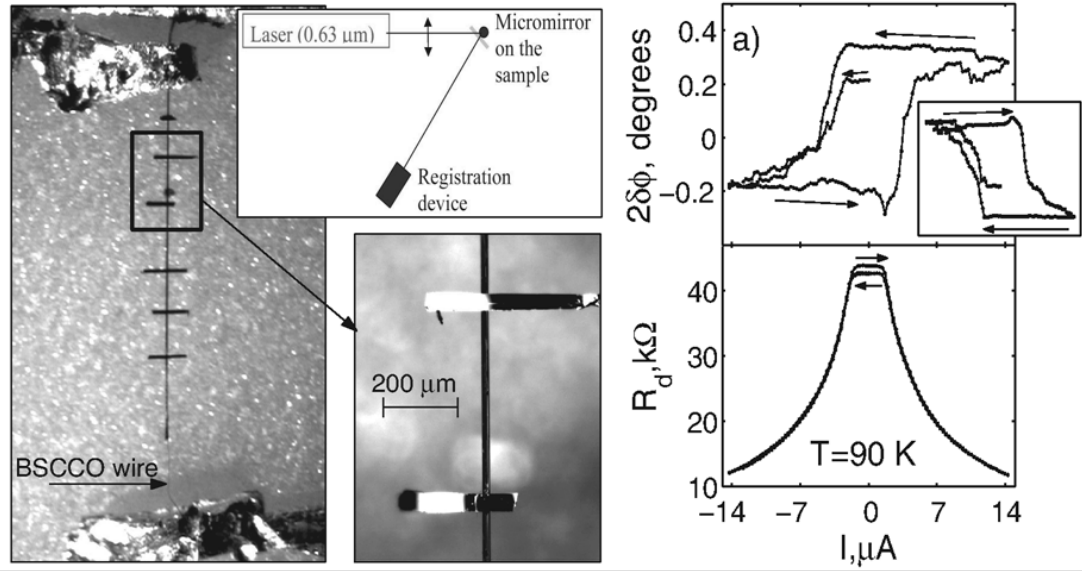


Figure 9.1: (left) Sample setup with several BSCCO wires which serve as mirrors and electrical contact to mechanically free end. (bottom middle) Magnification of BSCCO mirrors. (top middle) Diagram of experimental setup. (bottom right) Electrical resistance versus applied current. (top right) Twist angle versus applied current acquired simultaneously with the resistance. (inset of top right) Another sample from same parent sample mounted in opposite configuration [74].

voltage and measuring the twist angle similar to the results presented in the upper right of Figure 9.1. These loops are referred to as hysteresis loops and will be presented with respect to voltage instead of current. Initially the samples were assembled with NbSe<sub>3</sub> crystals as in Figure 8.1 a). The inset of Figure 9.2 a) illustrates a preliminary measurement of a hysteresis loop while the main image displays a hysteresis loop for samples A and B represented by unfilled and filled circles respectively. These results were obtained using FM techniques at  $T = 77$  K and verify that VITS is a genuine effect. The direction of the hysteresis loops are presented as arrows. The loops also show that the voltage at which the samples begin to twist ( $V_{on}$ ) is slightly smaller than the CDW depinning threshold voltage of  $V_T \sim \pm 50$  mV while the voltage the sample finishes twisting ( $V_{sat}$ ) is slightly larger than  $V_T$ . Notice that the hysteresis loops for samples A and B are slightly asymmetric with  $V_{on} \sim 20$  mV and  $V_{sat} \sim 80$  mV for positive voltages while for negative voltages  $V_{on} \sim -40$  mV and  $V_{sat} \sim$

$-100$  mV. Note that the two hysteresis loops have been normalized such that the VITS response has the same magnitude. The two samples having similar  $V_{\text{on}}$  and  $V_{\text{sat}}$  is coincidental. For example, the inset of Figure 9.2 a) shows a more symmetric hysteresis loop with onset and saturation voltages different from the other two.

Figure 9.2 b) has the dependence of the electrical resistance and the shear compliance on applied sample voltage acquired at  $T = 77$  K. The resistance is normalized to its ohmic resistance. Samples A and B are represented by unfilled and filled circles respectively. When the CDW is depinned it begins sliding creating an additional component to the overall current. This results in a drop in the overall resistance which can be clearly seen for both samples. A common problem in  $\text{TaS}_3$  at low temperatures is that CDW creep can begin at an additional threshold that is smaller than  $V_T$  [88, 89, 90]. In addition, since we are conducting a two-probe measurement we are sensitive to CDW phase-slips [88]. This makes it difficult to accurately obtain  $V_T$  from the resistance data. However the CDW depinning transition can be more clearly seen in the voltage dependence of the shear compliance shown in Figure 9.2 b). Samples A and B are represented by unfilled and filled triangles respectively. The shear compliance is normalized to its value when the applied voltage is zero. A single  $\text{TaS}_3$  crystal will have its lattice soften when the CDW is depinned resulting in an increase in the shear compliance by  $\sim 25\%$  for low frequencies. The torsional resistance of the  $\text{NbSe}_3$  reduces this response by approximately 80% in sample A and by 30% in sample B. This suggests that the  $\text{NbSe}_3$  crystal used to make sample A (B) has a slightly smaller (larger) cross-section than the  $\text{TaS}_3$  crystal.

The VITS response can be more cleanly measured by applying a square-wave potential to the sample with a peak-to-peak amplitude of  $2V_{\text{square}}$ . This will allow for the dynamics of the VITS response to be investigated. It was anticipated that there would be no response for  $V_{\text{square}} < V_{\text{on}}$ . Then as  $V_{\text{square}}$  is increased above  $V_{\text{on}}$  there would be an increasing VITS response as the hysteresis loops begin opening up.



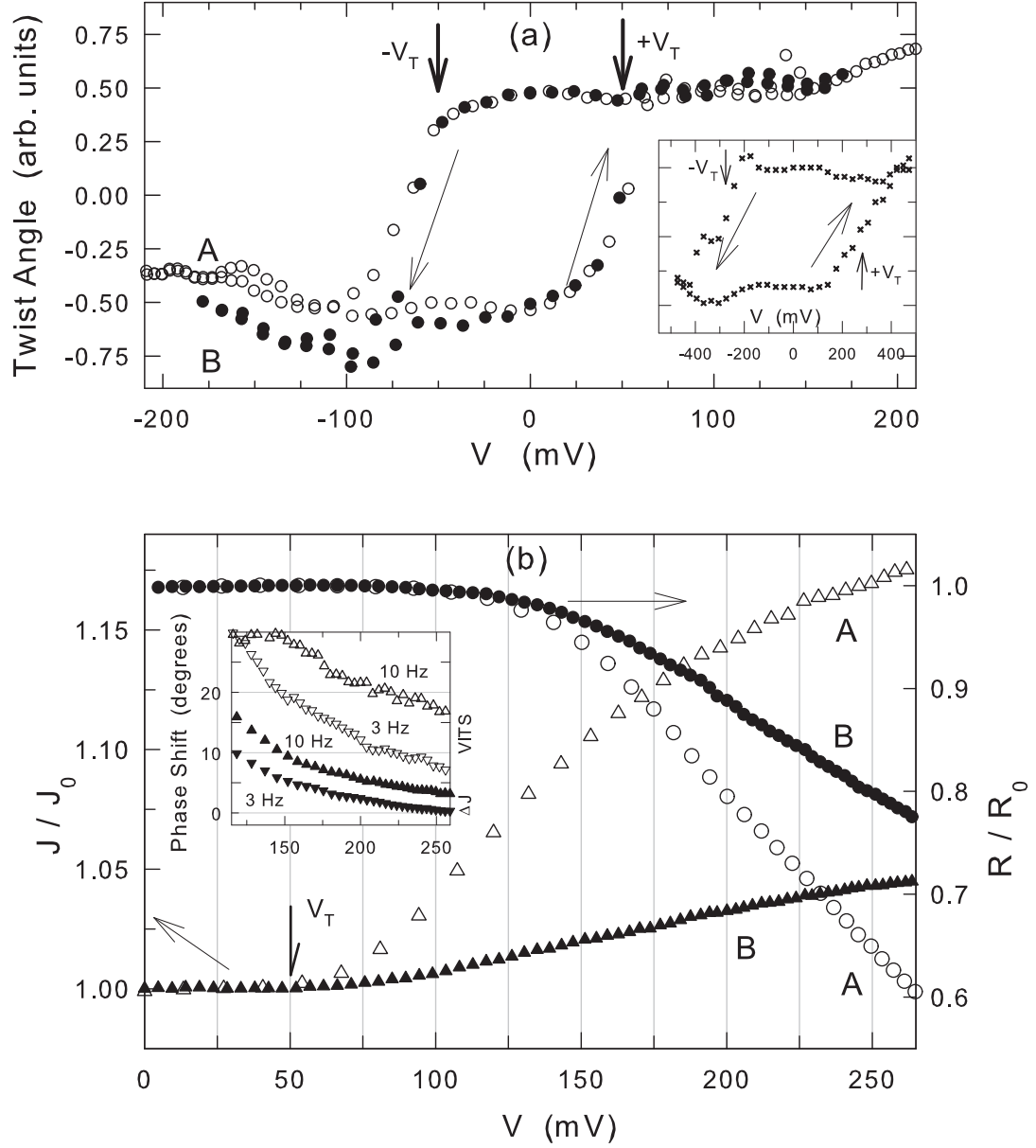


Figure 9.2: a) Twist angle of the sample versus applied sample voltage for samples A (open circles) and B (filled circles) in arbitrary units. Inset of a) twist angle versus voltage for a third sample. b) Normalized electrical resistance and normalized shear compliance versus applied sample voltage. The unfilled (filled) circles and triangles respectively represent  $R/R_0$  and  $J/J_0$  for sample A (B). Inset of b) phase shifts of VITS (unfilled triangle) and  $J$  (filled triangle) response versus applied voltage for 3 Hz and 10 Hz.

Finally the signal would saturate and remain constant for  $V_{\text{square}} > V_{\text{sat}}$  because the voltage is sweeping a complete hysteresis loop. Looking at the square wave responses in Figure 9.3, it is clear that even with the similar looking hysteresis loops of these two samples, their square wave response is quite different. Panel a) represents sample A while panel b) represents sample B. The top of each panel displays the voltage dependence of the in-phase response while the lower portions show the quadrature response. Considering the different frequencies shown, it is clear that this is a very slow response. The dynamics of the square wave signal continues to change and have a quadrature response with frequencies as low as 0.1 Hz. This sluggishness can also be seen in how the curves appear to move to the right with increasing frequency. Both samples begin to have a response at approximately  $V_{\text{on}}$ . This can be seen more clearly in the inset of panel a) which shows the in-phase response for small voltages for sample A. Also notice that sample A does not behave as anticipated. Instead of the in-phase response saturating at  $V_{\text{square}} = V_{\text{sat}} \sim 100\text{mV}$ , it continues to grow until  $V_{\text{square}} \sim 130\text{mV}$ . As frequency is increased, the voltage at which this saturation occurs increases and begins to slide out of our voltage window. Similarly, the quadrature signal for sample A has a peak near 80 mV which increases in both width and position with increasing frequency. On the other hand, sample B behaved slightly differently. Its low frequency in-phase response has a fairly symmetric peak near 100 mV. Also this response is larger for smaller frequencies. However instead of remaining constant, this signal begins to decay with increasing voltage. This response represents an initial twist when the square wave transitions from positive to negative or vice versa, followed by a relaxation towards its initial configuration while the applied sample voltage remains unchanged. This decay is also evident in the negative quadrature signal present at large voltages. Both the in-phase and quadrature have a peak that increase in both width and position with increasing frequency. However the position of the low frequency peak in the quadrature for sample B is at around

75 mV, which is slightly smaller than the peak position of the in-phase response.

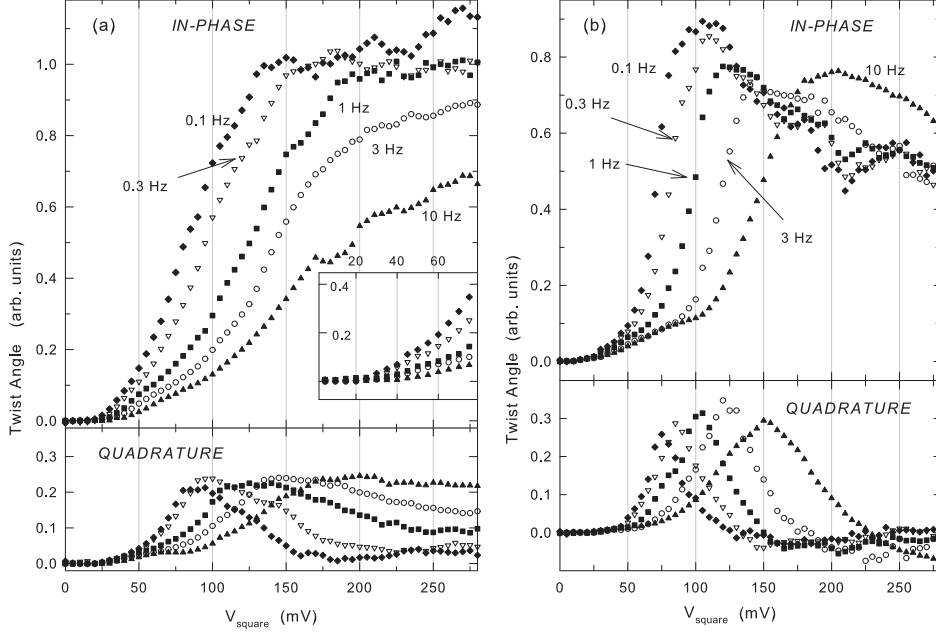


Figure 9.3: Dynamic VITS response to square wave voltage applied to sample A (a) and B (b) for several different frequencies. The in-phase and quadrature response are on top and bottom respectively. Inset of a) The in-phase response for small voltages.

The inset of Figure 9.2 b) displays the voltage dependence of the phase shifts for the VITS response (unfilled) and  $\Delta J$  (filled) response for 3 Hz (downward triangles) and 10 Hz (upward triangles). Notice that the phase shift associated with the VITS response is roughly three times larger than those associated with  $\Delta J$ . This implies that the VITS response is slower or more “sluggish” than the changes in the shear compliance. Changes in the shear compliance is known to be due to CDW domain configuration relaxing as the sample twists.

Since VITS is somewhat similar to the reverse piezoelectric effect, it was logical to investigate the presence of an analogous piezoelectric effect where an electrical potential is generated by an applied stress. Here the stress was applied to the sample

by a small 10 Hz magnetic field. This is identical to how the shear compliance measurements were conducted. However the modulated sample voltage was measured with a lock-in amplifier instead of a digital voltmeter. So the sample was rocked at a frequency of 10 Hz and the induced voltage was measured. In Figure 9.4 the AC induced emf is plotted with respect to the applied DC voltage. Samples A and B are respectively unfilled and filled symbols while the in-phase and quadrature signals are appropriately labeled. Notice that as the applied DC voltage increases there is no response until the sample voltage is  $\sim 100$  mV and then it increases steadily. Also there is no measurable quadrature response outside of the noise floor. The unshown 3 Hz data was identical with this 10 Hz data. This suggests that the induced emf response is much faster than the VITS response. When coupled to the fact there is no induced emf for voltages smaller in magnitude than  $V_{\text{sat}}$ , implies that this signal is associated with the faster torsional piezoresistance [91] and not VITS. Therefore there is either no induced emf associated with VITS or it is smaller than our noise floor of approximately  $3 \mu\text{V}$ .

The sluggishness of VITS in  $\text{TaS}_3$  can be seen in Figure 9.5 where the hysteresis loops taken at several frequencies or periods (T) are presented for samples C and D. These curves were acquired by utilizing the dynamic FM technique. The sample was driven with a triangle wave voltage and the demodulated output of the cavity in the time domain was recorded with a digital oscilloscope. These two samples were mounted using the thin film of gold on approximately half of the crystal effectively halving the torsional elastic anomalies. The depinning threshold voltages of the CDW are shown as vertical arrows at the bottom of each graph. Notice that these values are slightly larger than for samples A and B suggesting that they are less pure [61]. The threshold voltages are  $V_T \sim 300$  mV for sample C and  $V_T \sim 200$  mV for sample D. One thing that is remarkable is that even though this response is very slow and the dynamics vary greatly in the frequency window shown, the amplitude of the

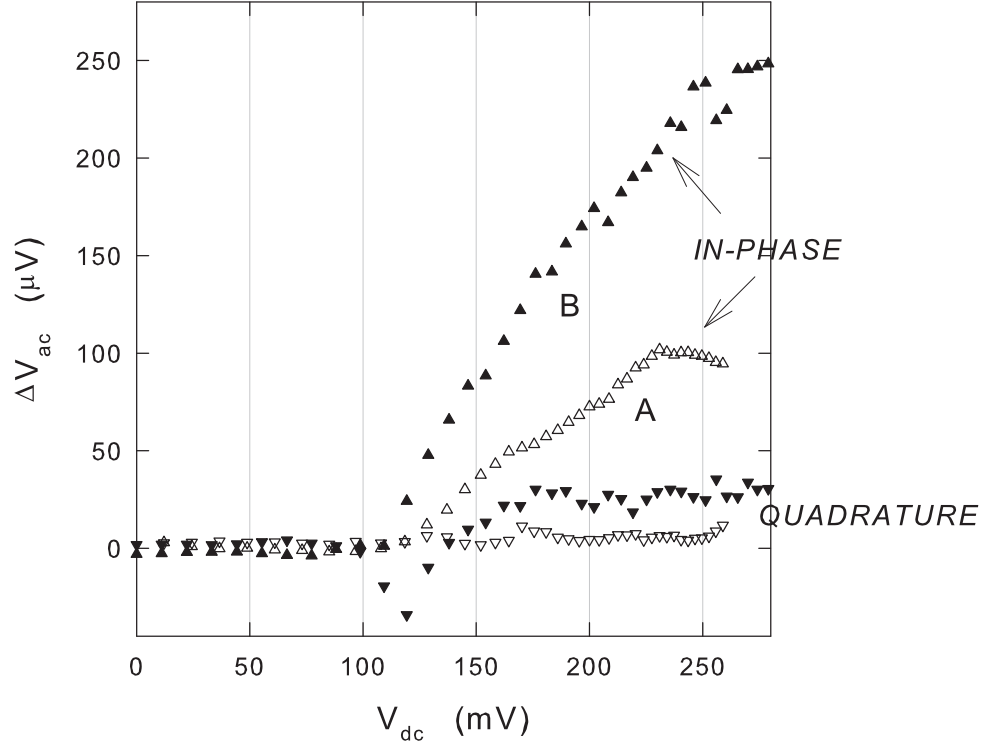


Figure 9.4: Inducted AC voltage for samples A and B with 10 Hz oscillating torque applied to the sample.

VITS response is approximately unaffected by changes in frequency for these two samples for voltage sweeps of  $\pm 2V_T$ . Another feature is that samples C and D twist in opposite directions. Similar to samples A and B, these two samples had an onset of the twisting less than  $V_T$  and a saturation voltage slightly larger than  $V_T$ . The parameter with the strongest frequency dependence is  $V_{\text{sat}}$ . As the period increases,  $V_{\text{sat}}$  decreases for both positive voltages and negative voltages. Both samples C and D have asymmetries in their hysteresis loops similar to samples A and B. However for sample C the asymmetry is more in the dynamics. For positive voltages, the voltage window in which the sample is twisting (i.e.  $V_{\text{on}} < V < V_{\text{sat}}$ ) is broader than for negative voltages. Also  $V_{\text{on}}$  is smaller for positive voltages than for negative ones. Like samples A and B, sample C does minimal twisting for voltages above  $V_{\text{sat}}$ . Sample D has a different form of asymmetry. Opposite of sample C,  $V_{\text{on}}$  is smaller

for negative voltages. Also, more drastic, is that for positive voltages there is a decay for  $V > V_{\text{sat}}$ .

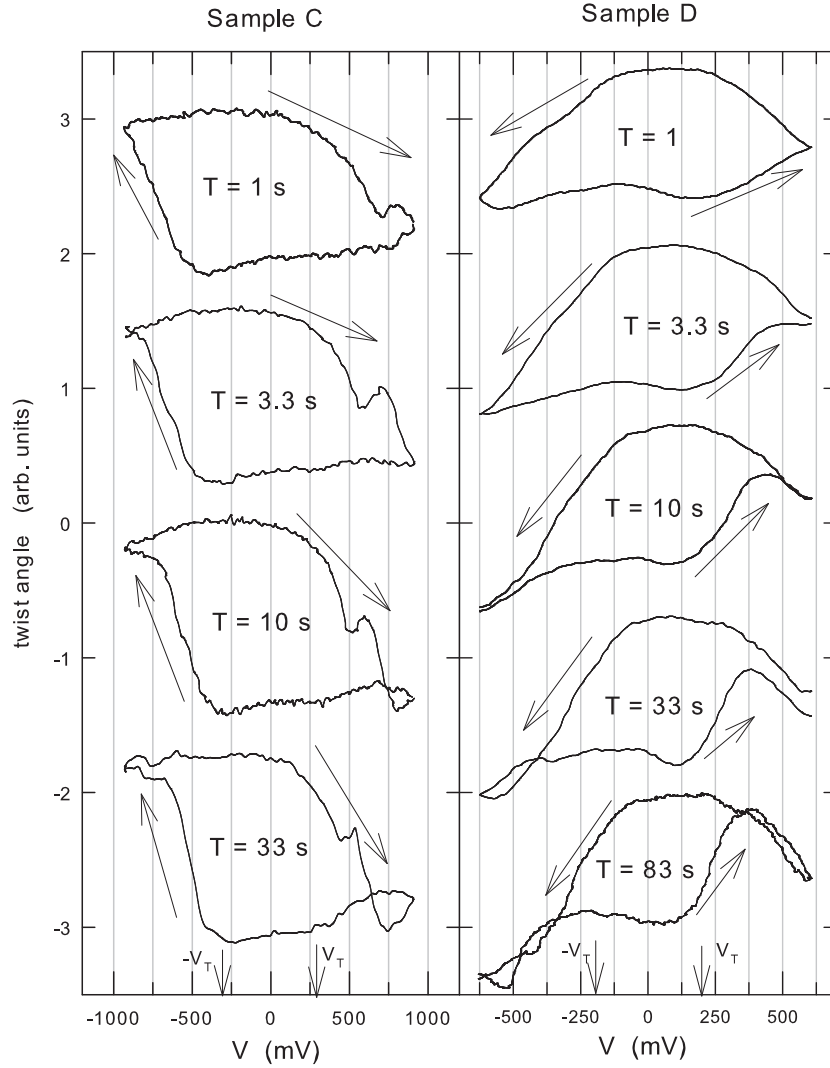


Figure 9.5: Hysteresis loops at several different frequencies for samples C and D. Each curve is a numerical average of several cycles. The appropriate depinning thresholds are shown on the bottom of each graph. There is an arbitrary vertical offset for clarity.

If  $\text{TaS}_3$  is to be utilized as a microscopic torsional actuator, most probably it will involve switching back and forth from positive and negative values. Figure 9.6 illustrates the VITS response due to a square wave potential being applied to the sample in the time domain. This was accomplished in a similar manner as the hys-

teresis loops in Figure 9.5 except the triangle wave is replaced with a square wave as discussed in Section 8.3.3. The response at voltages of  $1.5V_T$  and  $3V_T$  are presented for frequencies of 10 Hz, 1 Hz and 0.1 Hz. Each curve is normalized to its period. A sample applied square wave voltage ( $V_{\text{applied}}$ ) is shown in the lower right panel to illustrate the phase of the response. Notice that the signal from sample D is in phase with the square wave while the response from sample C is out of phase. This also implies that the two samples twist in the opposite direction and is consistent with the response in Figure 9.5. Notice that for the long period curves at  $3V_T$  for both samples the negative strains (i.e. when the response is less than zero) undergo a small delay followed by a decay. This decay is absent from the small periods, smaller voltages and for positive strains. Surprisingly in sample C for  $T = 10$  s, the response is larger for  $1.5V_T$  than it is for  $3V_T$ . Also the asymmetry in sample C is evident at both applied voltages when this voltage transitions from negative to positive. When this occurs, the VITS response spikes to a positive value before finally relaxing into its negative value approximately 5 ms after the voltage transition. The asymmetry is also evident for  $V = 1.5V_T$  by the  $T = 1$  s curve saturating after 100 ms for negative strains but not for positive strains. Also the  $T = 10$  s curve saturates after approximately 3 s for positive strains but not for negative strains. The differences in the positive and negative half-cycles suggests that VITS has a complex dependence on the history before each voltage switch in sample C. Although sample D is much noisier than sample C, its response seems more symmetric.

The VITS response was also investigated by looking at the frequency dependence when a square wave voltage was applied to the sample. Figures 9.7 and 9.8 display this for several different voltages for samples C and D, respectively. This data was obtained by sweeping the magnitude of  $V_{\text{square}}$  at a constant frequency identical to the method used to obtain the data presented in Figure 9.3. The typical voltage dependence of this response for samples C and D is shown in the inset of the respective

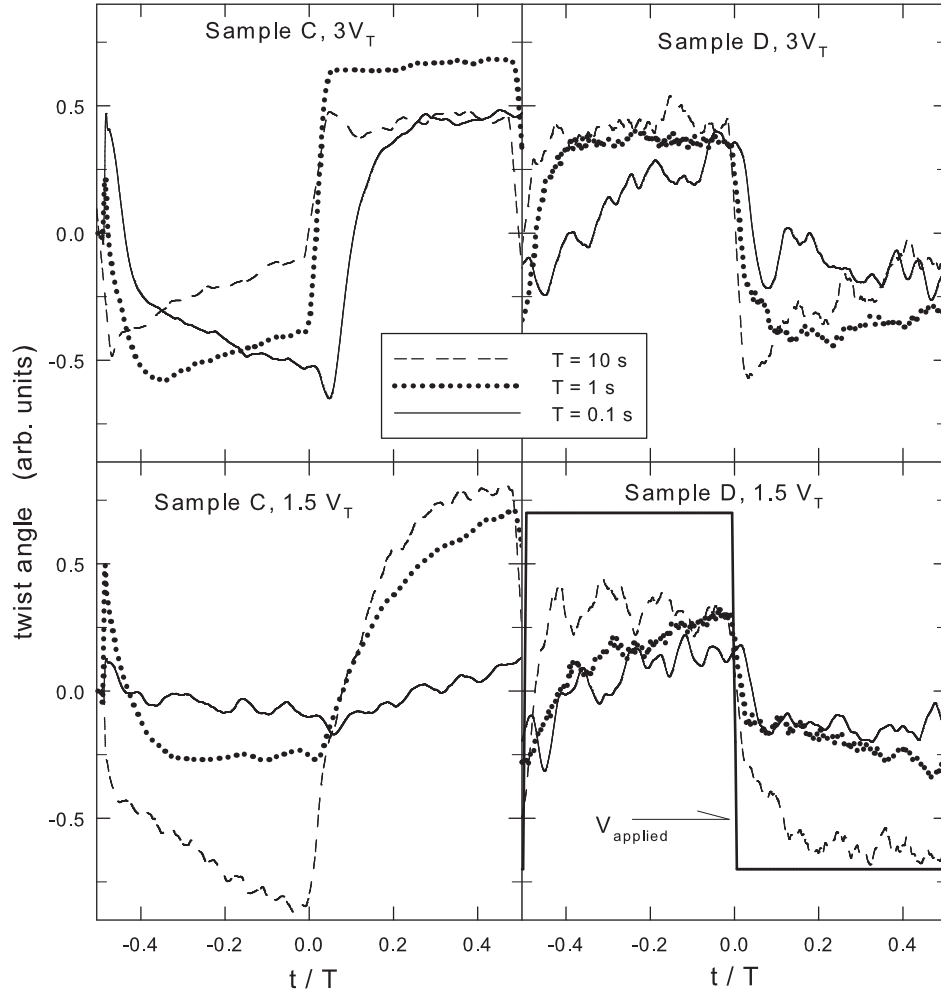


Figure 9.6: Time dependence of the VITS response due to square wave potentials of  $V = 1.5V_T$  and  $V = 3V_T$ . This response with periods of  $T = 0.1$  s, 1 s and 10 s is normalized to its period. The lower right panel shows the phase of the applied square wave.

figures. These curves were obtained at several different frequencies and then frequency slices at a constant voltage were plotted. For the insets, circles represent 0.2 Hz data and triangles represent 5 Hz data. For all other plots, the in-phase signal is represented by filled symbols and the quadrature signal is represented by unfilled symbols. Note that the behavior in the voltage domain for both samples C and D is in between the two extremes set by samples A and B illustrated in Figure 9.3. The response of sample C at  $V = 2.25V_T$  shows two inflection points in the in-phase and



two peaks in the quadrature. This suggests that there are two relaxation processes in this sample. Therefore the response is fit to the following equation:

$$\epsilon_\omega = \frac{\epsilon_{\omega 1}}{1 - i\omega\tau_1} + \frac{\epsilon_{\omega 2}}{1 - i\omega\tau_2} \quad (9.1)$$

where  $\omega$ ,  $\epsilon_{\omega i}$  and  $\tau_i$  are respectively the frequency, amplitude and time constant associated the relaxation.

The voltage dependence of these parameters can be seen in Figure 9.9. For  $V > 2V_T$  the time constants have a very strong voltage dependence  $\tau_1 \sim V^{-4.5}$  and  $\tau_2 \sim V^{-8}$ . This is much stronger than the voltage dependence of the time constant associated the the electro-optic response  $\tau_{\text{electro-optic}} \sim V^{-1.5}$  [92] which is related to the diffusion of longitudinal CDW phase deformations that are enhanced by phase-slip [93].

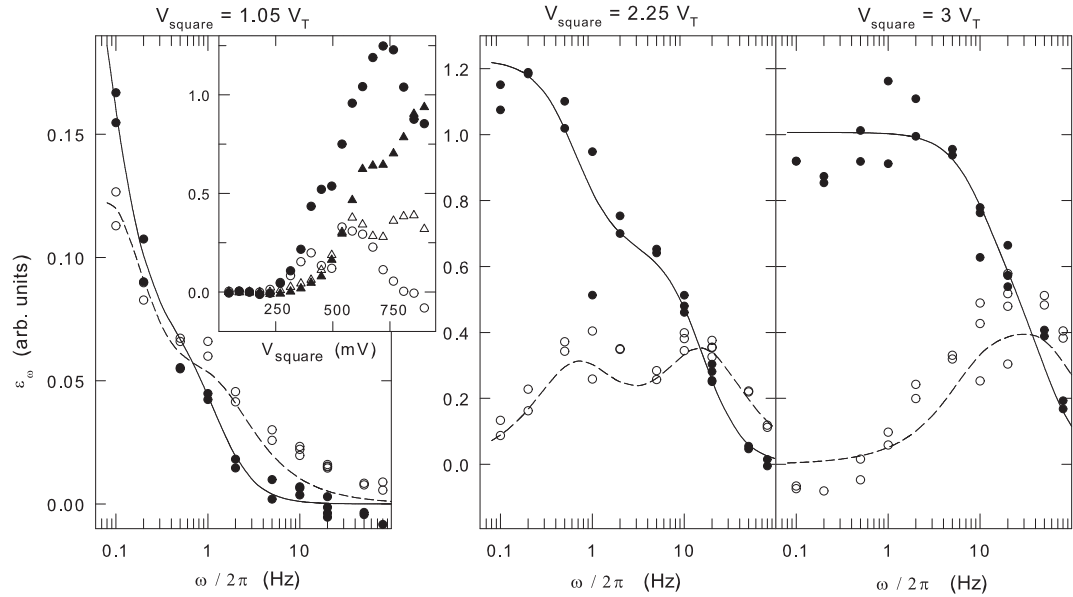


Figure 9.7: Frequency dependence of VITS response due to square waves applied to sample C for  $V = 1.05V_T$ ,  $V = 2.25V_T$  and  $V = 3V_T$ . The inset shows the voltage dependence of the square wave response for 5 Hz (triangles) and 0.2 Hz (circles). The in-phase and quadrature response is represented by filled and unfilled symbols respectively. The curves represent fits to Equation 9.1.

The response from sample D is shown in Figure 9.8. Notice that the quadrature

signal is less than half that of the in-phase response suggesting that this sample would be better modeled by a distribution of relaxation times:

$$\epsilon_{\omega} = \int \frac{a(\tau)d\text{Ln}\tau}{1 - i\omega\tau} \quad (9.2)$$

Thus the VITS response was fit to the Cole-Cole expression [94, 95]:

$$\epsilon_{\omega} = \frac{\epsilon_{\omega 0}}{1 + (-i\omega\tau_0)^{\gamma}}, \quad (9.3)$$

where  $\gamma$  is a constant and the distribution of relaxation times is represented by:

$$a(\tau) = \frac{\epsilon_{\omega 0}}{\pi} \left( \frac{\tau}{\tau_0} \right)^{\gamma} \frac{\sin(\gamma\pi)}{1 + 2\left(\frac{\tau}{\tau_0}\right)^{\gamma}\cos(\gamma\pi) + \left(\frac{\tau}{\tau_0}\right)^{2\gamma}}. \quad (9.4)$$

The voltage dependence of the parameters of this fit is also displayed in Figure 9.9.

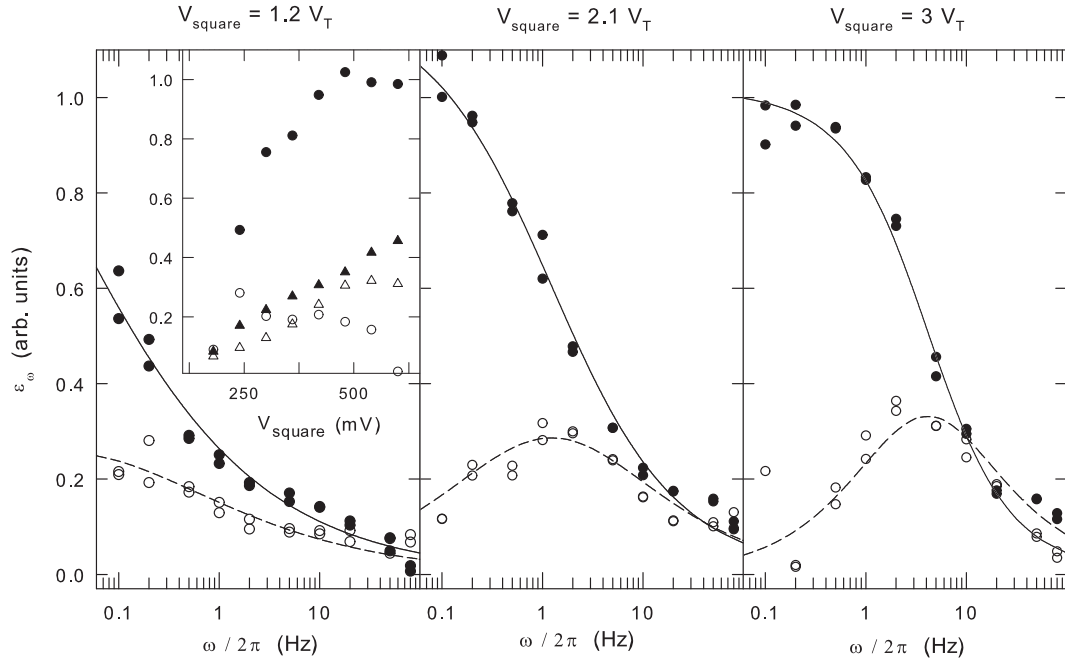


Figure 9.8: Frequency dependence of VITS response due to square waves applied to sample C for  $V = 1.2V_T$ ,  $V = 2.1V_T$  and  $V = 3V_T$ . The inset shows the voltage dependence of the square wave response for 5 Hz (triangles) and 0.2 Hz (circles). The in-phase and quadrature response is represented by filled and unfilled symbols respectively. The curves represent fits to Equation 9.3.

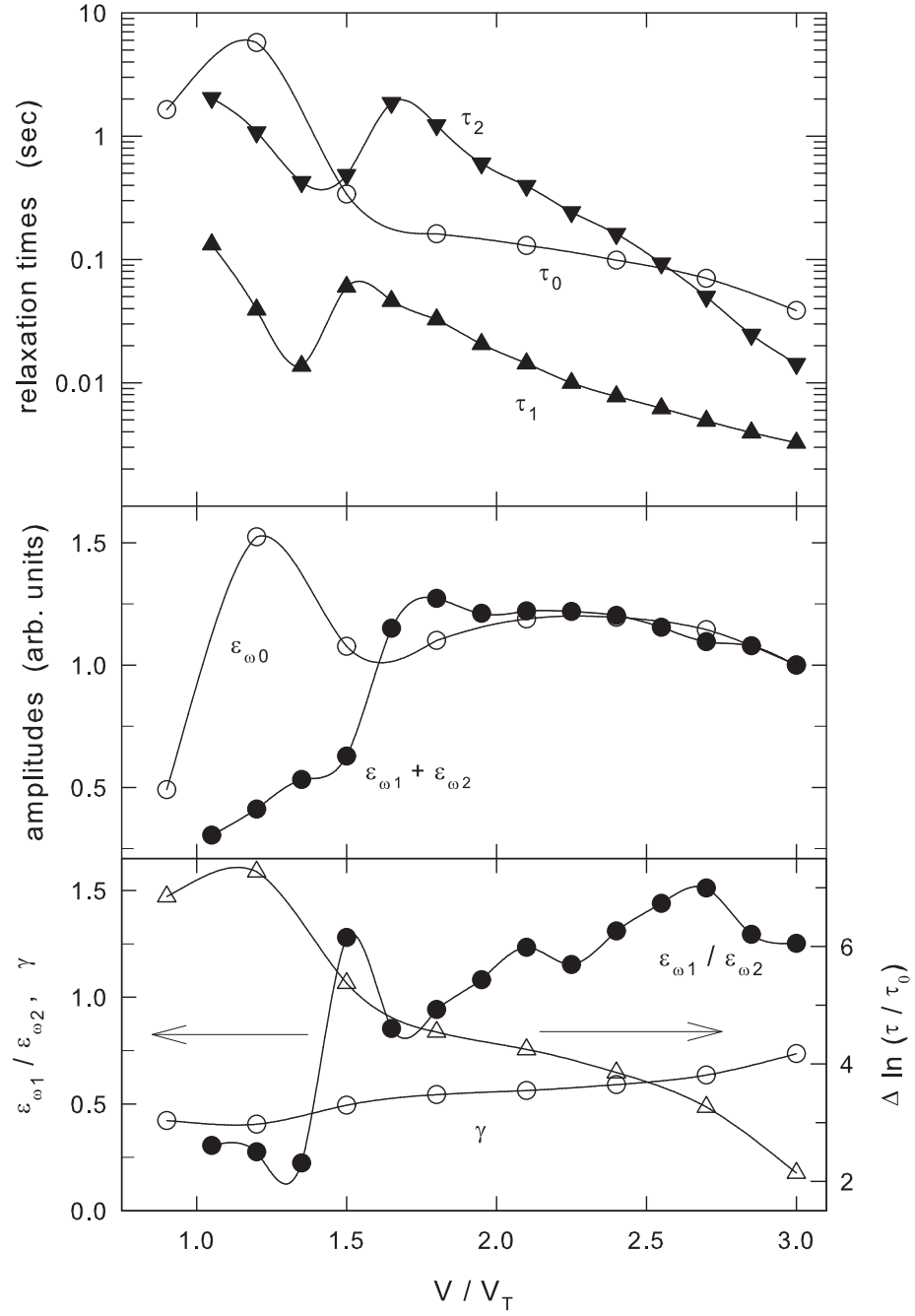


Figure 9.9: The voltage dependence of the parameters from Equation 9.1 (Sample C) and 9.3 (Sample D). Sample C is represented by filled symbols and sample D by unfilled. The width of the distribution of relaxations times for sample D is shown in the bottom panel. The curves are guides for the eye.

In addition to the voltage dependence of the parameters obtained from fits to Equations 9.1 and 9.3, the full width at half maxima ( $\Delta \text{Ln}(\tau/\tau_0)$ ) for sample D is also plotted in the bottom panel of Figure 9.9. Note that for small voltages ( $V < 1.5V_T$ ), the signal is in the hysteresis loop. This causes the peaks due to relaxation to move out of our measurable frequency window. Therefore the parameters associated with sample D for these voltages have very large uncertainties. Notice that for large voltages ( $V > 2.5V_T$ )  $\tau_0$  is larger than  $\tau_1$  and  $\tau_2$ . However for intermediate voltages ( $1.5V_T < V < 2.5V_T$ )  $\tau_0$  is larger than  $\tau_1$  but smaller than  $\tau_2$ . Also, in this voltage window the width of the distribution of relaxation times for sample D is between one and two decades wide. The voltage dependence of  $\tau_0$  is comparable to  $\tau_{\text{electro-optic}}$  however,  $\tau_0$  is roughly three orders of magnitude larger [92].

## Chapter 10 Temperature and External Torque dependence of VITS

### 10.1 Torque Dependence

We then began to investigate the dependence of VITS on an applied external torque. This torque was created by a DC magnetic field which rotated the steel wire and twisted the TaS<sub>3</sub> crystal. The magnetic field was generated by passing an electric current ( $I_B$ ) through a Helmholtz coil that is attached to the tail of the dewar. The calibration factor of this coil is 80 Gauss/Amp. The voltage dependence of the resistance and shear compliance is presented in Figure 10.1 for sample E with different external torques applied to it. The data for  $I_B = + 0.9$  A is represented by upward pointing triangles while the downward pointing triangles is for  $I_B = + 0.3$  A. Notice that the resistance is approximately independent of applied external torque. Similar to other samples, the depinning threshold is smeared out for reasons described above (see Figure 9.2 b)).

Applying an external torque will change the separation between the steel wire and the transducer. This will cause the magnitude of the response from the RF cavity to decrease as the steel wire moves away from the transducer. So in order to compare the torque dependence of the torsional response, the signal associated with different values of  $I_B$  must be normalized to each other. This is accomplished in a similar manner as the shear compliance measurements. A small AC magnetic field is applied by summing this modulated current with  $I_B$ . The demodulated output of the RF cavity with  $V_{\text{sample}} = 0$  is defined as  $V_{J_0}$ . It is assumed that the modulated twists in the crystal caused by the AC component of the magnetic field is independent of  $I_B$ . If the response is assumed to be linear,  $1/V_{J_0}$  will be a linear function of  $I_B$  (ie.  $\Delta(1/V_{J_0}) \propto \Delta I_B$ ). Notice from the inset in Figure 10.1 that this is approximately true, however there is a slight hysteresis. When the direction that  $I_B$  was swept

changes, the sample will stick slightly causing it to slightly undershoot its equilibrium position. To ensure that the sample is initially in the same state, the CDW is depinned by applying a positive voltage (i.e.  $V_{\text{sample}} > V_T$ ) to the sample. This voltage is then removed and  $V_{J_0}$  is measured.

In addition, the geometry associated with the sample such as the length of the steel wire and distance between the steel wire and the transducer can be used to normalize the response to absolute units. The estimates in these measurements coupled with the assumption that the geometry does not drastically change with temperature results in this being a “rough” normalization of the signal. This normalization could be off by up to a factor of two. In other words, the relative uncertainty remains small, but the uncertainty associated with the normalization to absolute units is large. For sample E, it was determined that the calibration factor is  $\partial\phi/\partial I_B \sim 12^\circ/\text{A}$ . Therefore the sample will twist by  $\Delta\phi \sim 7^\circ$  for changes in magnetic current of  $\Delta I_B = 0.6 \text{ A}$ .

The bottom of Figure 10.1 shows the voltage dependence of the shear compliance for two different values of  $I_B$ . Note that these curves have been normalized as described above. Notice that these two curves are similar but do not lie perfectly on top of each other. It is not clear whether this is due to the shear compliance having a small torque dependence or due to uncertainties associated with the normalization. In either case this is a much smaller effect than the dependence of the square wave response on applied torque described below. Therefore any dependence of the change in shear compliance on applied torque is considered negligible. One can clearly see that  $V_T \sim 180 \text{ mV}$  for sample E and it is independent of external torque within the sensitivity of our measurement.

Figure 10.2 a) presents the voltage dependence of the VITS response ( $\epsilon_\omega$ ) due to a square wave potential being applied to the sample. These results were obtained in a similar fashion to the ones presented in Figures 9.7 and 9.8 for magnetic currents of  $I_B = +0.3 \text{ A}$  and  $I_B = -0.6 \text{ A}$ . Note that the normalization is displayed. This data was

also obtained with sample E at  $T = 77$  K. First notice that the overall amplitude of the in-phase response (filled symbols) has a clear dependence on  $I_B$ . Most remarkable is that since the responses for the two magnetic currents have opposite signs, the sample twisted in opposite directions. This illustrates that the applied external torque not only changes the magnitude of the VITS response, but also its direction. Also, the peak in the quadrature (open symbols) is at a voltage closer to  $V_T$  for  $I_B = -0.6$  A suggesting it has a faster response than for  $I_B = +0.3$  A. Shown in Figure 10.2 b) is the frequency dependence of  $\epsilon_\omega$  for two different values of  $I_B$  and  $V_{\text{square}}$ . The lines represent fits to Equations 9.3. The dependence of the parameters of these fits and other unrepresented curves on magnetic current is presented in Figure 10.3.

Hysteresis loops for sample F can be seen in Figure 10.4. These loops were obtained in a similar manner as those in Figure 9.6. The applied triangle wave had a frequency of 0.3 Hz and an amplitude 0.75 V. Note that twist angle of this sample due to  $I_B$  will be  $\partial\phi/\partial I_B \sim 5^\circ/\text{A}$  and that the typical amplitude of a single hysteresis loop is  $\sim 0.1^\circ$ . The hysteresis loops have an asymmetry similar to samples described above. The transition at positive voltages appears to be more gradual than at negative voltages. The loop for  $I_B = +0.2$  A has the largest amplitude. As  $I_B$  is increased further, the magnitude of this response begins being suppressed. At  $I_B = +0.8$  A the main loop is completely suppressed leaving only a small loop at negative voltages. For  $I_B > +0.8$  A the main loop reopens. However, now it is twisting in the opposite direction. An external torque changing the direction of the VITS response is consistent with the results in Figure 10.2 a).

We have shown that the VITS response has a strong dependence on external torque. From this we propose that this effect is due to a residual twist initially being present in the crystal. This initial torque could be from either defects present in the crystal or from mounting the crystal. So according to this model, when the response disappears at  $I_B = +0.8$  A, the magnetic field is untwisting the twist initially in the

sample, approximately eliminating the response. The fact that there is still a small loop at  $I_B = + 0.8$  A and that response is also suppressed for  $I_B < + 0.2$  A suggests that there is a complex array of multiple twists initially present in the sample making it impossible to completely eliminate the VITS response with external torques.

Notice that the hysteresis loops in Figure 10.4 for increasing values of  $I_B$  have a  $\frown$  shaped voltage dependence superimposed onto them. This is due to the increase in the in the shear compliance for  $V > V_T$ . Therefore the angle which TaS<sub>3</sub> twists ( $\phi(V)$ ) due to the external magnetic field will also depend on the sample voltage. So as  $J$  increases for voltages above threshold, the change in the twist angle ( $\Delta\phi(V) = \phi(V) - \phi(0)$ ) will also increase. For this sample,  $J/J_0 \sim 3\%$  at  $V = 0.75$  V, resulting in the amplitude of the  $\frown$  shape being comparable to the VITS signal at  $I_B = + 1.0$  A.



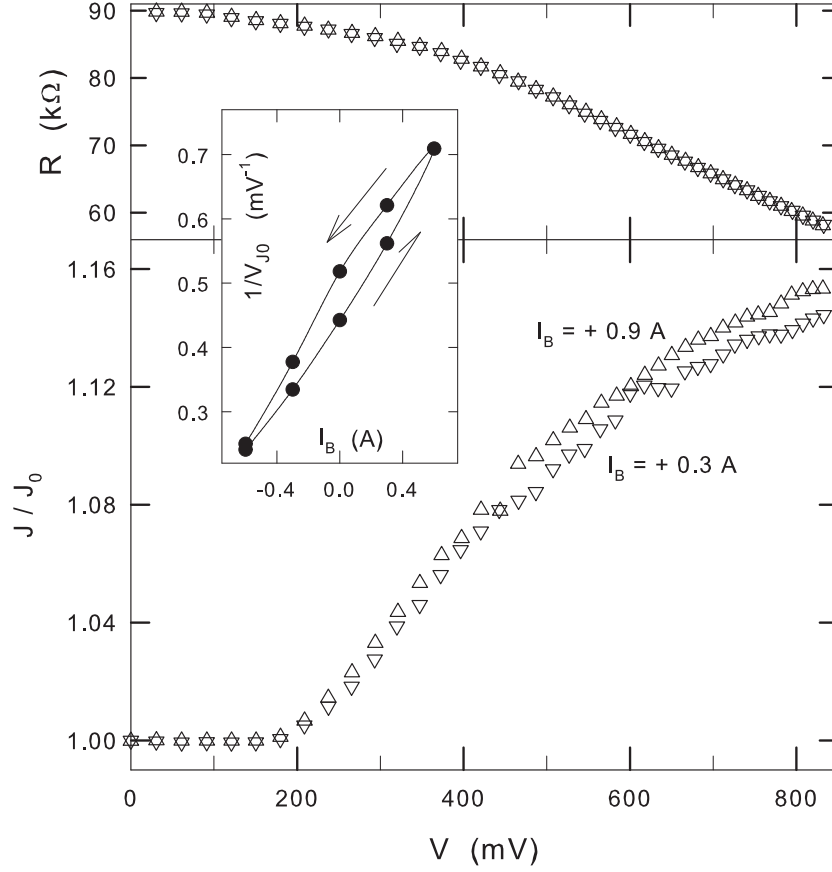


Figure 10.1: Voltage dependence of resistance and shear compliance at  $T = 77$  K for sample E. Values for applied magnetic currents of  $I_B = 0.9$  A (upward pointing triangles) and  $I_B = 0.3$  A (downward pointing triangles) are presented. Inset  $1/V_{J_0}$  dependence on  $I_B$  used to obtain twist amplitude of  $\partial\phi/\partial V_T \sim 12^\circ/\text{A}$ .

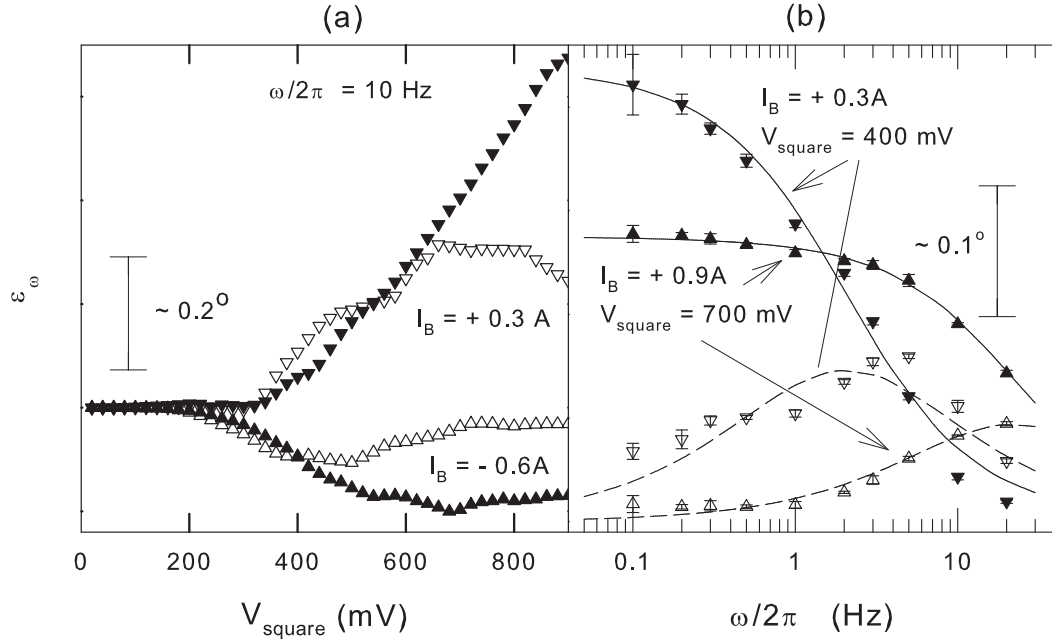


Figure 10.2: a) Voltage dependence of the VITS ( $\epsilon_\omega$ ) at  $T = 77$  K due to a 10 Hz square wave voltage applied to sample. The in-phase symbols are filled and the quadrature symbols are unfilled. Data is presented for  $I_B = +0.3$  A and  $I_B = -0.6$  A. b) Frequency dependence of  $\epsilon_\omega$  for  $I_B = +0.3$  A and  $I_B = +0.9$  A at  $V_{\text{square}} = 400$  mV and  $V_{\text{square}} = 700$  mV respectively. The curves are fits to Equation 9.3. The twist angle is  $\partial\phi/\partial I_B \sim 12^\circ/\text{A}$ .

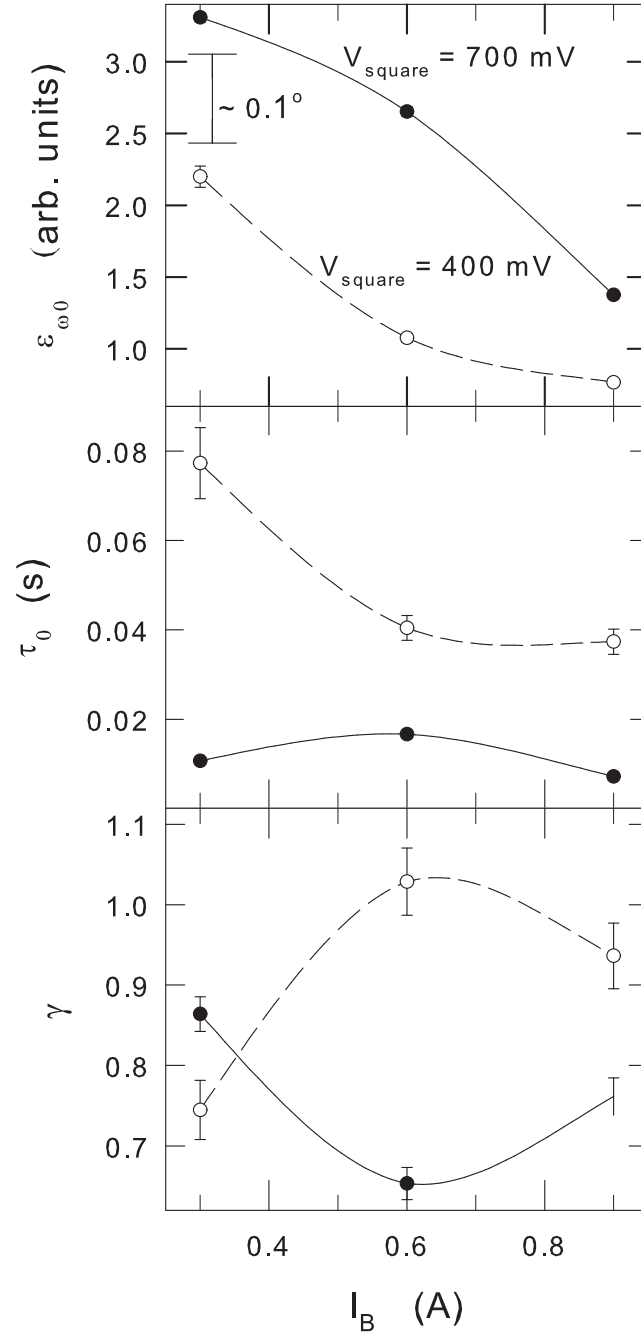


Figure 10.3: The dependence of parameters to fits to Equation 9.3 on  $I_B$  for sample E with 700 mV (closed symbols) and 400 mV (open symbols). Note that some error bars are smaller than the points. The twist angle is  $\partial\phi/\partial I_B \sim 12^\circ/\text{A}$ .

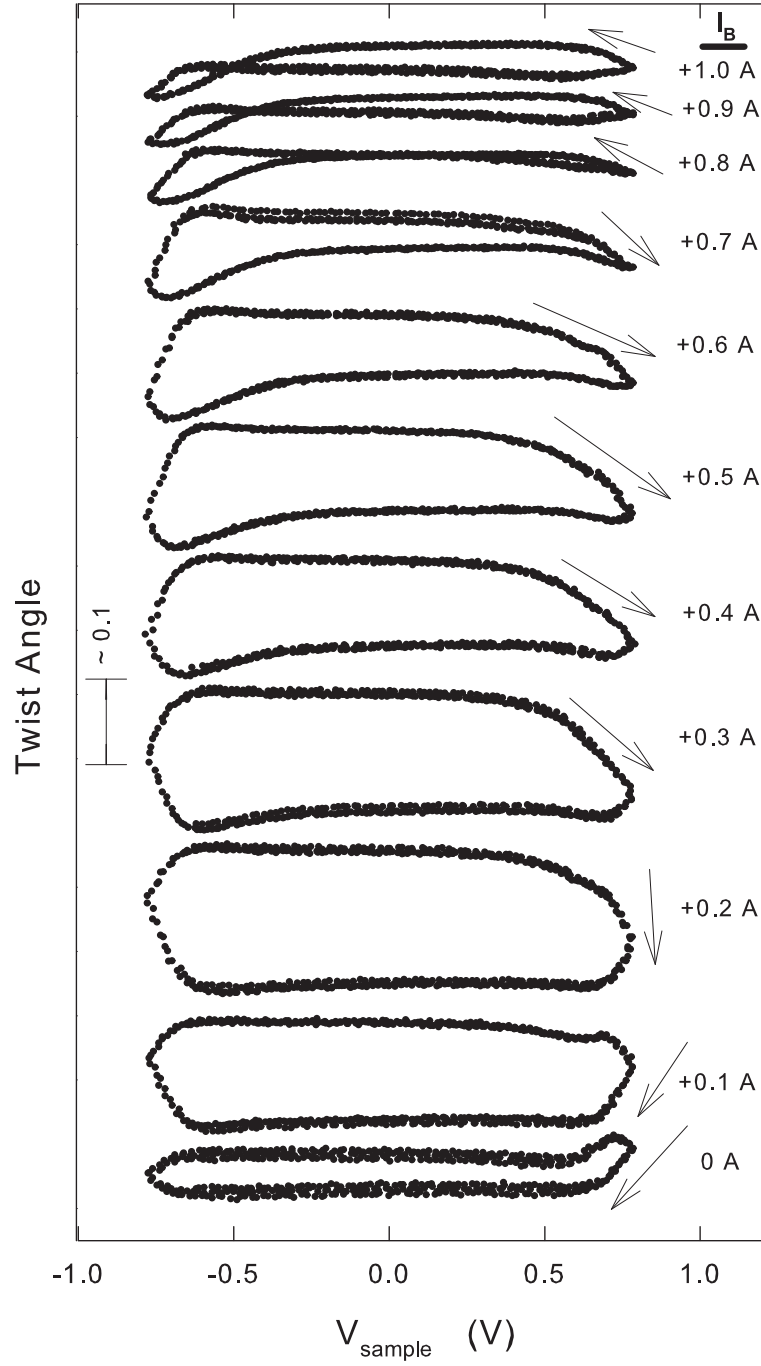


Figure 10.4: Hysteresis loops for several different values of  $I_B$  for sample F. They were obtained with 0.75 V, 0.3 Hz triangle wave at  $T = 77$  K. There is a vertical offset for clarity and arrows mark direction of each loop. The twist angle is  $\partial\phi/\partial I_B \sim 5^\circ/\text{A}$ .

## 10.2 Temperature Dependence

In order to help understand the origin of slow VITS response, a temperature dependent study was performed on sample G. This sample had a relatively short steel wire ( $L \approx 1$  mm). This gives the sample a relatively large resonant frequency of 730 Hz while limiting the magnitude of the applied external torque. This allows a larger frequency window to be investigated without contributions from resonant effects. Although the response could have been normalized to absolute units as samples E and F were, this was not done and the results for sample G are presented in arbitrary units.

The voltage dependence of the resistance and shear compliance at temperatures of 90 K, 100 K, 110 K and 120 K for sample G are shown in Figure 10.5 a). As the temperature increases, approaching  $T_P = 220$  K, the overall resistance of the sample decreases as expected. In addition, CDW creep decreases allowing for  $V_T$  to be more clearly observed in the resistance data. However note that the depinning voltage thresholds obtained from the resistance curves are still larger than the ones from the shear compliance. The reason for this difference in thresholds obtained from the resistance and shear compliance curve is due to phase slip at the contacts. This phase slip is the potential difference necessary to convert the the quasi-particle current at the contacts into the CDW current in the bulk of the crystal [87]. Since elastic properties depend on only depinning in the bulk and not on the contacts, the shear compliance provides a more accurate measurement for  $V_T$ .

A consequence of using a smaller steel wire is the linear deflections of the end of the wire will be smaller as well. This results in a decrease in the amplitude of the output of the RF cavity. This decreases the signal to noise ratio which can be seen in the slightly more noisy shear compliance data. From the bottom panel of Figure 10.5 a) notice that within this noise the change in the shear compliance is

approximately independent of temperature for  $T > 90$  K. For large voltages ( $V = 300$  mV) the magnitudes of the shear compliance change for all measured temperatures are comparable. However the  $T = 90$  K data has a weaker voltage dependence than was observed at higher temperatures. The values for  $V_T$  obtained for the different temperatures are presented in Figure 10.7 b).

In Figure 10.5 b), the voltage dependence of the VITS response due to a 10 Hz square wave being applied to the sample is presented. The in-phase and quadrature are presented in the top and bottom panels respectively. This response is displayed for the same four temperatures as the resistance and shear compliance in part a). Notice that the onset voltage of this response ( $V_{\text{on}}$ ) is slightly smaller than  $V_T$  which is consistent with the other samples. The temperature dependence of  $V_{\text{on}}$  can be seen in Figure 10.7 b). One can see that the VITS response is speeding up as the temperature is increased. Consider the quadrature response obtained at  $T = 120$  K. Notice that it has a peak at  $V \sim 150$  mV and a shoulder at  $V \sim 200$  mV. The increase in both magnitude and the positions of these features implies that the response is slowing down (i.e  $\tau_0$  is increasing) as the temperature is lowered. For  $T = 90$  K, the response has slowed to the extent that these features are moving out of our voltage window. For the responses obtained at  $T = 120$  K and 110 K, the in-phase response saturates at  $V \sim 250$  mV. As with the shear compliance, the slowing down of the VITS response can also be seen in the weaker voltage dependence at lower temperatures. Notice that as temperature is decreased, the saturation voltage increases along with the amplitude of the torsional response.

From Figure 10.7 b), notice that  $V_T$  and  $V_{\text{on}}$  have a slight temperature dependence. Therefore in making temperature dependent measurements it was necessary to develop a voltage criterion that would drive the CDW with a fixed potential. It was not clear whether  $V_{\text{on}}$  or  $V_T$  was the relevant threshold. This distinction is not very relevant for  $T \geq 90$  K since  $(V_T - V_{\text{on}})$  is approximately constant here. We

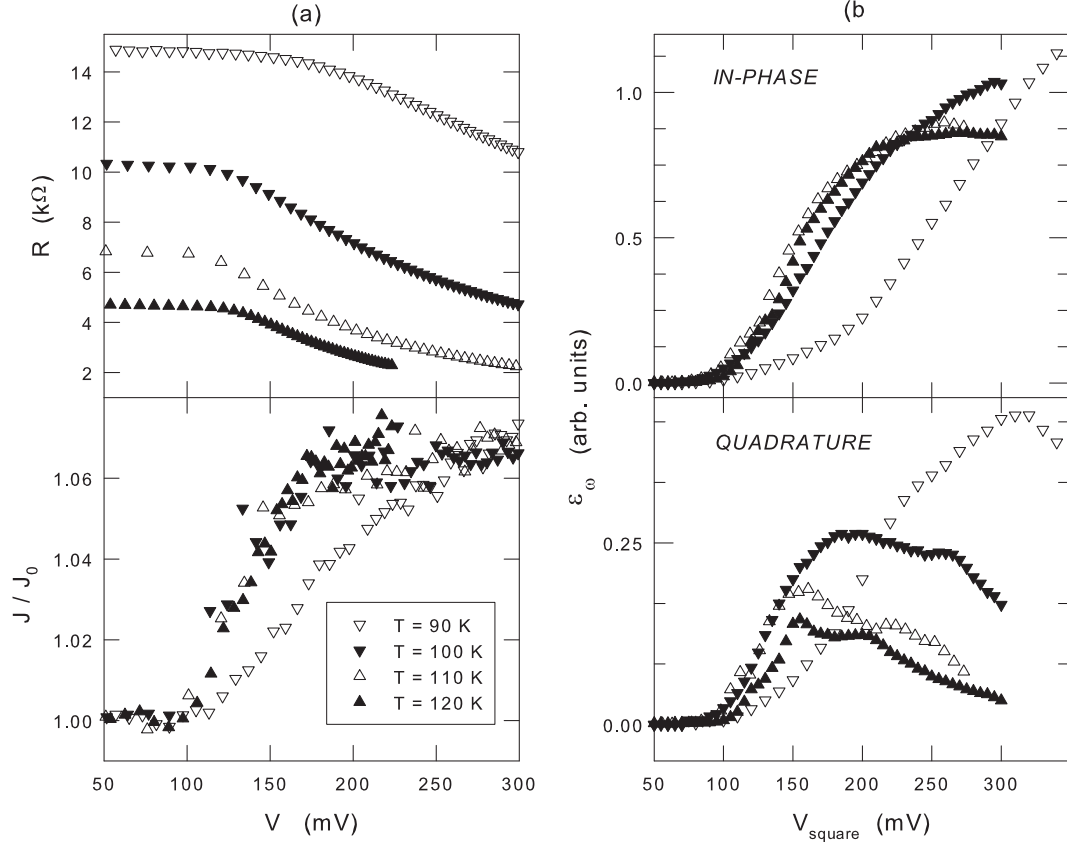


Figure 10.5: a) Voltage dependence of resistance and shear compliance for temperatures of 90 K, 100 K, 110 K and 120 K of sample G. b) Voltage dependence of the VITS response due to a 10 Hz square wave applied to the sample for the same temperatures as in a).

then measured the frequency dependence of the torsional strain due to square wave potentials being applied to the sample. The voltages used were:  $V_T$ ,  $V_{\text{on}} + 50$  mV,  $V_T + 50$  mV,  $V_{\text{on}} + 100$  mV and  $V_T + 100$  mV. These measurements were made at several different temperatures. Examples of this response is illustrated in Figure 10.6 for  $V_{\text{square}} = V_{\text{on}} + 100$  mV at temperatures of 90 K and 110 K. The increase in the speed of the VITS signal with increasing temperature is also shown in the peak in the quadrature response (open symbols) moving from  $f \sim 1$  Hz at  $T = 90$  K to  $f \sim 50$  Hz at  $T = 110$  K. The curves in the figure are fits to Equation 9.3.

The temperature dependence of the parameters to the fits for several voltages is presented in Figure 10.7 a). Notice that the amplitude of the VITS response for each

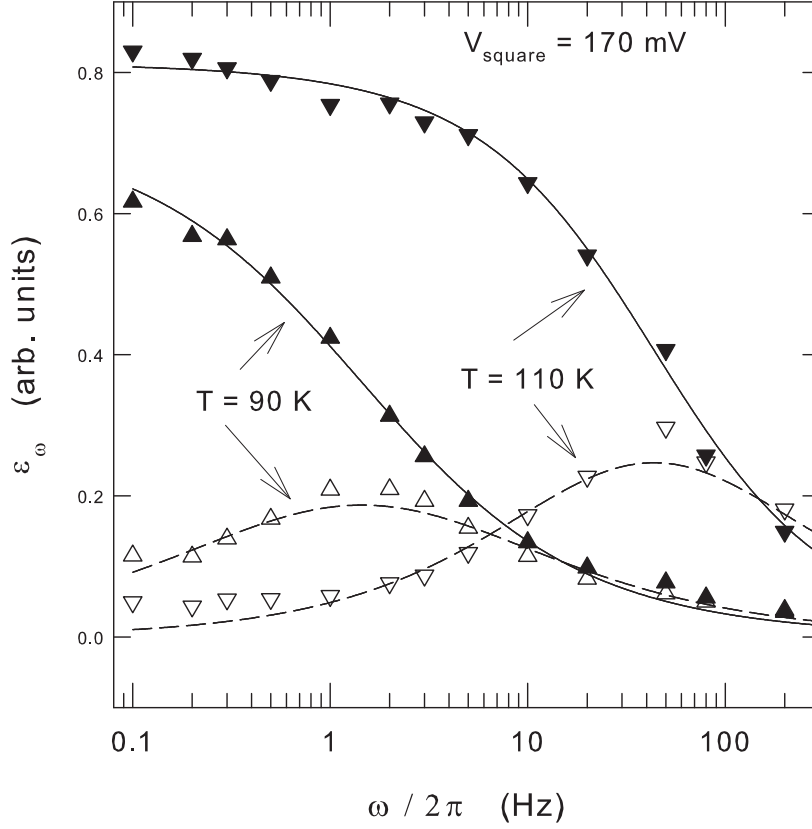


Figure 10.6: Frequency dependence due to  $V = V_{\text{on}} + 100 \text{ mV} = 170 \text{ mV}$  square wave applied to the sample at  $T = 90 \text{ K}$  and  $110 \text{ K}$  for sample G. The filled and open symbols represent the in-phase and quadrature responses respectively. The curves are fits to Equation 9.3.

voltage is roughly independent of temperature. This is consistent with the results of Pokrovskii *et. al.* (Reference [96]). Also note that the time constant ( $\tau_0$ ) decreases with increasing temperature. Changing the temperature by  $\Delta T = 30 \text{ K}$  results in  $\tau_0$  changing by approximately two orders of magnitude for a given voltage and by three orders of magnitude when comparing the extremes in this temperature and voltage window. The bottom panel displays the exponent ( $\gamma$ ). Notice that at  $T = 120 \text{ K}$ ,  $\gamma$  has a strong voltage dependence varying from  $\gamma \sim 0.7$  to  $\gamma \sim 0.3$ . These values correspond to a width in the time constant distribution peak of roughly one and five decades respectively.



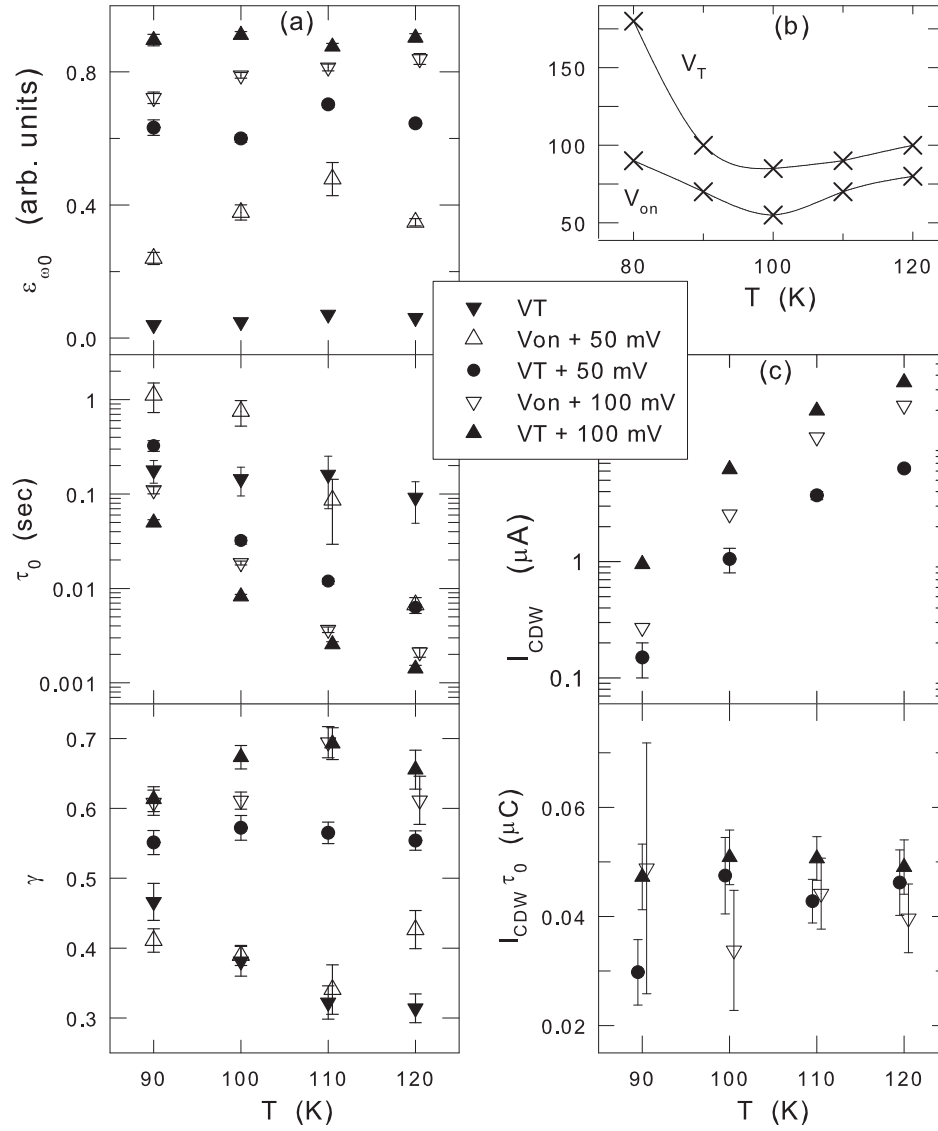


Figure 10.7: The temperature dependence for sample G of a) parameters of fits to Equation 9.3 b) square-wave and CDW onset voltages and c) the CDW current and  $I_{CDW}\tau_0$ . When not visible, the error bars are smaller than the symbols.

When the CDW is depinned it flows through the crystal carrying an additional electrical current. Therefore the total current will be the sum of the ohmic term and a component due to the CDW expressed as:

$$I_{total} = \frac{V}{R_0} + I_{CDW} \quad (10.1)$$

The temperature dependence of the CDW current ( $I_{\text{CDW}}$ ) is displayed in the top panel of Figure 10.7 c). Notice that  $I_{\text{CDW}}$  decreases by roughly two orders of magnitude for each voltage in this temperature window. In comparison, the ohmic resistance ( $R_0$ ) only drops by roughly a factor of three in this same window. Also note that the lower panel shows the temperature dependence of the term  $I_{\text{CDW}}\tau_0$  which within the uncertainty of the measurement is approximately independent of both voltage and temperature. This suggests that  $\tau_0$  primarily depends on  $I_{\text{CDW}}$  with the following relation:

$$\tau_0 \propto \frac{1}{I_{\text{CDW}}} \quad (10.2)$$

Unfortunately to date, no temperature dependent studies of the relaxation times associated with longitudinal deformations of the CDW on TaS<sub>3</sub> have been performed. However such measurements have been performed on K<sub>0.3</sub>MoO<sub>3</sub> using electro-optic techniques [97]. The dependence of this time constant on temperature and  $I_{\text{CDW}}$  is much weaker than the same dependencies of the time constant ( $\tau_0$ ) associated with the VITS response that we are observing in TaS<sub>3</sub>.

## Chapter 11 Modeling of VITS

### 11.0.1 Qualitative Modeling

It has been previously shown that in TaS<sub>3</sub> voltage-induced deformations of the CDW will have a hysteretic dependence on voltage similar to the hysteresis loops associated with the VITS response [98, 99, 100, 92, 101]. Assuming that the VITS response is coupled to the deformations in the CDW, the torsional response ( $\epsilon$ ) will obey the following equation:

$$\frac{d\epsilon}{dt} = \frac{\epsilon_0(V) - \epsilon}{\tau} \quad (11.1)$$

Where the voltage dependent time constant is:

$$\tau = \begin{cases} \infty & V < V_{ON} \\ \tau_0 & V_{ON} < V < V_{SAT} \\ \tau_0(V_{SAT}/V)^6 & V > V_{SAT} \end{cases} \quad (11.2)$$

Notice that the infinite time constant for small voltages will inhibit the response and  $\tau$  was given the voltage dependence observed in sample C for large voltages. The voltage dependent term of the strain will be:

$$\epsilon_0(V) = \begin{cases} 0 & V < V_{ON} \\ (V - V_{ON})/(V_{SAT} - V_{ON}) & V_{ON} < V < V_{SAT} \\ 1 & V > V_{SAT} \end{cases} \quad (11.3)$$

The strain can be simulated by plugging Equations 11.2 and 11.3 into Equation 11.1 and solving for  $\epsilon$  while assuming  $V_{SAT} = 1.5V_{ON}$ . Illustrated in Figure 11.1 is the voltage dependence of the theoretical torsional strain for several different periods. These curves exhibit the sluggish behavior observed in our experimental results. No-

tice that these loops continue to narrow even for  $T \gg \tau_0$ . This is consistent with the results in Figure 9.5 where even when  $T > \tau_0$ , the hysteresis loops do not have the exact shape of the static hysteresis loops obtained on the same sample.

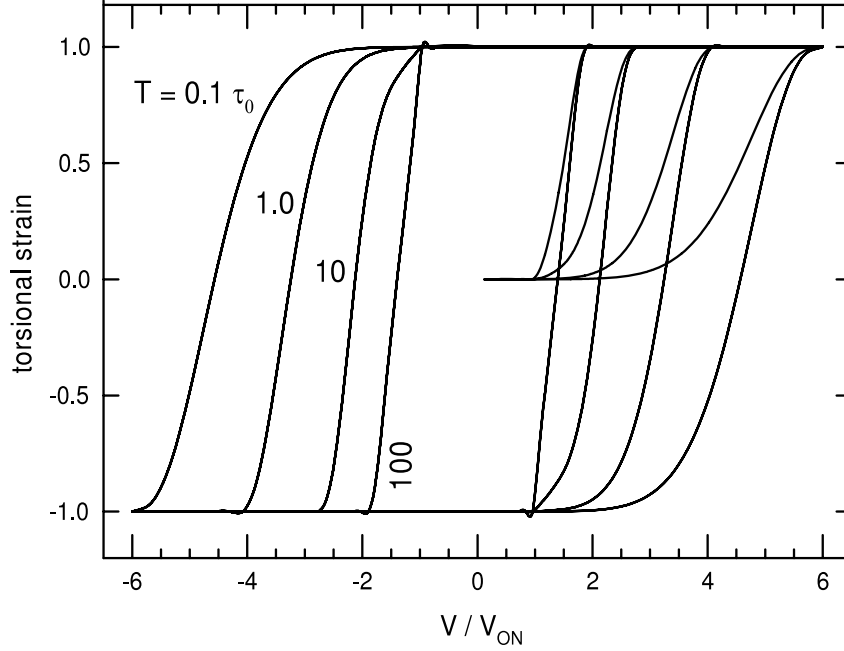


Figure 11.1: Simulated hysteresis loops from Equation 11.1 for four different periods.

### 11.0.2 Quantitative Modeling

Recall from Chapter 10 we proposed that the VITS response is due to some initial twist being present in the sample. This could be due to either defects present in the crystal or sample mounting. The initial twist from mounting could be due to not perfectly attaching the steel wire allowing gravity to produce a torque or from being twisted by motion due to the drying of the silver paint which makes the electrical contact to each end of the crystal. Whether the initial twist is inherent in the crystal or generated when mounting the sample, the wave vector will have an azimuthal

component with the following form:

$$\vec{q} = q_0(\hat{z} + \beta r \hat{\phi}) \quad (11.4)$$

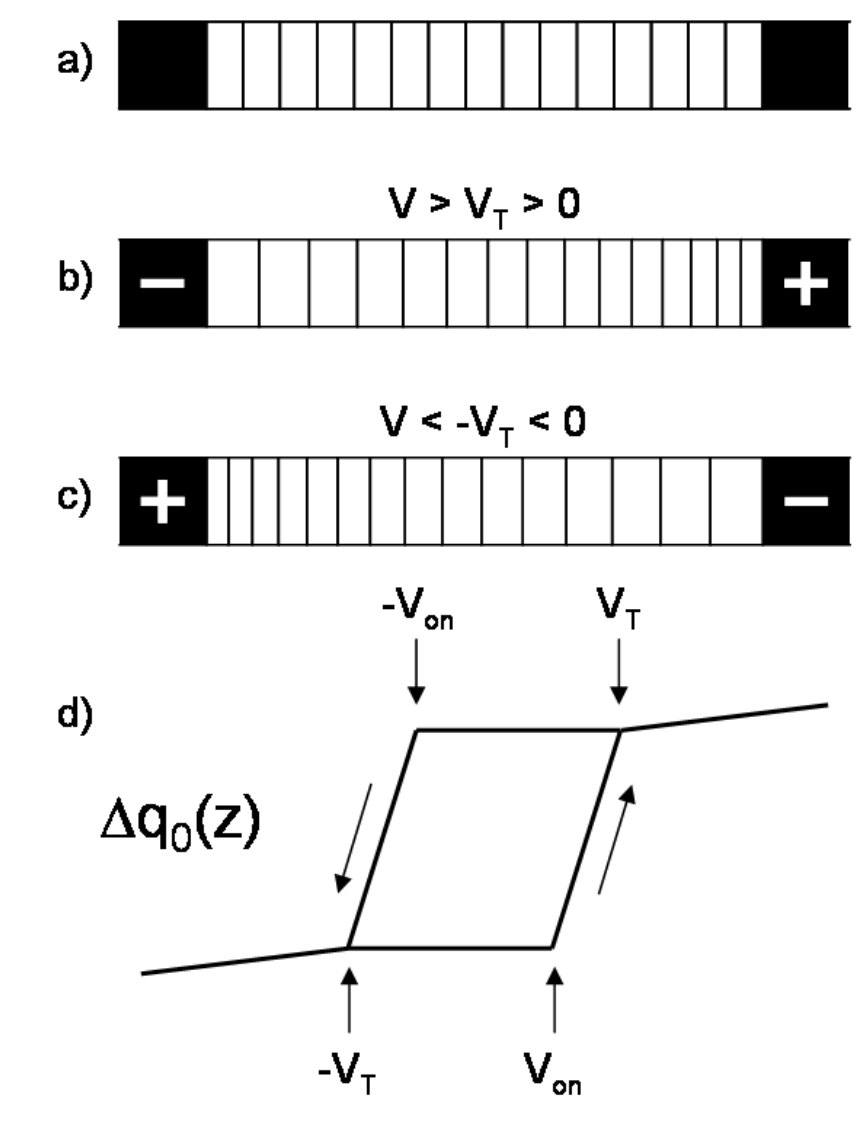


Figure 11.2: The alignment of the CDW wavefronts in an untwisted crystal due to applied voltage for a) sample with CDWs that have never been depinned, b) samples that have been above positive threshold and c) samples that have been below negative threshold. d) The general voltage dependence of  $\Delta q_0(z)$ .

where  $q_0$  is the wave vector when there is no initial twist,  $\hat{z}$  is a unit vector in the longitudinal direction,  $\hat{\phi}$  is a unit vector in the azimuthal direction,  $\beta = \partial\phi/\partial z$  and  $r$

is the distance from the center of the sample. For simplicity, a circular cross-section is assumed. When a CDW is depinned, the wave fronts will compress near the more positive contact and rarify near the other contact [98]. This effect will be modeled by:

$$q_0(z) = q_{00} + \Delta q_0(z), \quad (11.5)$$

where  $q_{00}$  is the position and voltage independent component of the wave vector and  $\Delta q_0(z)$  is the additional term that accounts for the relative motion of the wave fronts. This motion for untwisted crystals is illustrated in Figure 11.2. Panel a) displays a sample that has never had the CDW depinned ( $|V| < \pm V_T$ ). If the voltage is increased above the positive threshold ( $V > V_T$ ), the wave fronts will compress near the positive contact as shown in panel b). The motion of these wave fronts has a hysteretic dependence on voltage as shown in panel d). So the wave fronts will stay in this configuration as long the voltage is never decreased below the negative threshold ( $V < -V_T$ ). Once this occurs, the wavefronts will then shift so that they rarify near this contact as illustrated in panel c). The wave fronts will then stay in this state until the voltage is again increased above the positive threshold. This results in  $\Delta q_0(z)$  having a similar voltage dependence as is observed in the VITS response in TaS<sub>3</sub>. This behavior of  $\Delta q_0(z)$  will produce a gradient in the pitch of the azimuthal component of the CDW wave vector. In addition,  $\Delta q_0(z)$  has small non-hysteretic changes near the electrodes [100, 97] which does not appear to be related to the VITS response.

It has been shown that longitudinal strains in  $\Delta q(z)$  can couple to the lattice [81]. This will produce longitudinal stresses in the crystal lattice. This stress will change the overall length of the crystal by  $\Delta L/L \sim 10^{-6}$ . This is much smaller than the VITS response which has an effective piezoelectric coefficient of  $\sim 10^{-4}$  cm/V. We suggest the reason the changes in length are so small is due to the changes in

the wave vector ( $\Delta q_0(z)$ ). If  $\Delta q_0(z)$  were perfectly symmetric about the center of the crystal (i.e.  $\Delta q_0(z) = -\Delta q_0(L-z)$ ), then one half of the crystal will expand while the other half will compress by the same amount. This will result in the overall length of the crystal ( $L$ ) remaining constant. However there is a slight asymmetry in  $\Delta q_0(z)$  [82, 102] (i.e.  $\Delta q_0(z) \sim -\Delta q_0(L-z)$ ) (See Figure 7.6) resulting in the two halves of the crystal compressing and expanding by slightly different amounts. This will yield a small but finite length change [81, 103].

For a circular rod clamped at ( $z = 0$ ) with a torque ( $T$ ) applied at some ( $z \leq L$ ), the rod will twist by [104]:

$$\phi = \frac{Tz}{IG} \quad (11.6)$$

where  $G$  is the shear modulus and  $I = \pi R^4/2$  is the polar moment of inertial. The torsional rigidity ( $\kappa$ ) is the ratio of the applied torque and the twist angle [105] as follows:

$$\kappa \equiv \frac{T}{\phi} \quad (11.7)$$

$$= \frac{\pi GR^4}{2z} \quad (11.8)$$

$$\sim \frac{GR^4}{z} \quad (11.9)$$

where this is an order of magnitude estimate so factors of  $\sim 2$  will be ignored.

One might assume that the torsional stress is proportional to  $\beta\Delta q_0(z)$ . However if this were the case, there would be a sign inversion at the center of the crystal and almost no net twist at the free end ( $\Delta\phi(L) \sim 0$ ). It has been shown that the VITS response grows as distance from the clamped end of the crystal increases [74]. This results in a maximum twist angle at the free end ( $\Delta\phi_{\max} \sim \Delta\phi(L)$ ). This behavior will be exhibited if the torsional stress is proportional to  $\partial q/\partial z$ . This condition will be fulfilled if it is assumed that  $\beta\Delta q_0(z)$  produces an external torque ( $\eta$ ) on the sample

that is resisted by the torsional rigidity. This torque can be obtained by integrating over the moment arm as follows:

$$\eta(z) \sim \frac{\mu}{q_{00}} \int dA r (\beta r \Delta q_0) \quad (11.10)$$

$$\sim \frac{\mu}{q_{00}} (\beta \Delta q_0) \int_0^{2\pi} d\phi \int_0^R r dr r^2 \quad (11.11)$$

$$\sim \frac{\mu}{q_{00}} (\beta \Delta q_0) (2\pi) \frac{R^4}{4} \quad (11.12)$$

$$\sim \frac{\mu}{q_{00}} (R^4 \beta \Delta q_0) \frac{\pi}{2} \quad (11.13)$$

$$\sim \frac{\mu}{q_{00}} (R^4 \beta \Delta q_0) \quad (11.14)$$

where  $\mu$  is the trans-modulus that relates strains in the CDW to stresses within the crystal lattice. Now filling in for the torsional rigidity:

$$\eta(z) \sim \frac{\mu}{q_{00}} \frac{z\kappa}{G} (\beta \Delta q_0) \quad (11.15)$$

$$\therefore \frac{\eta(z)}{\kappa} \sim \frac{\mu z \beta \Delta q_0}{G q_{00}} \quad (11.16)$$

Now the total twist angle can be obtained by integrating  $\partial(\eta/\kappa)/\partial z$  over the length of the sample:

$$\frac{\partial \Delta \phi}{\partial z} \sim \frac{\partial(\eta/\kappa)}{\partial z} \quad (11.17)$$

$$\sim \frac{\partial}{\partial z} \left( \frac{\mu z \beta \Delta q_0}{G q_{00}} \right) \quad (11.18)$$

$$\sim \frac{\mu \beta}{G q_{00}} \frac{\partial}{\partial z} (z \Delta q_0) \quad (11.19)$$

$$\Delta \phi \sim \frac{\mu \beta}{G q_{00}} \int_0^L dz \frac{\partial}{\partial z} (z \Delta q_0) \quad (11.20)$$

$$\therefore \Delta \phi(L) \sim \frac{\mu \beta L \Delta q_0(L)}{G q_{00}} \quad (11.21)$$



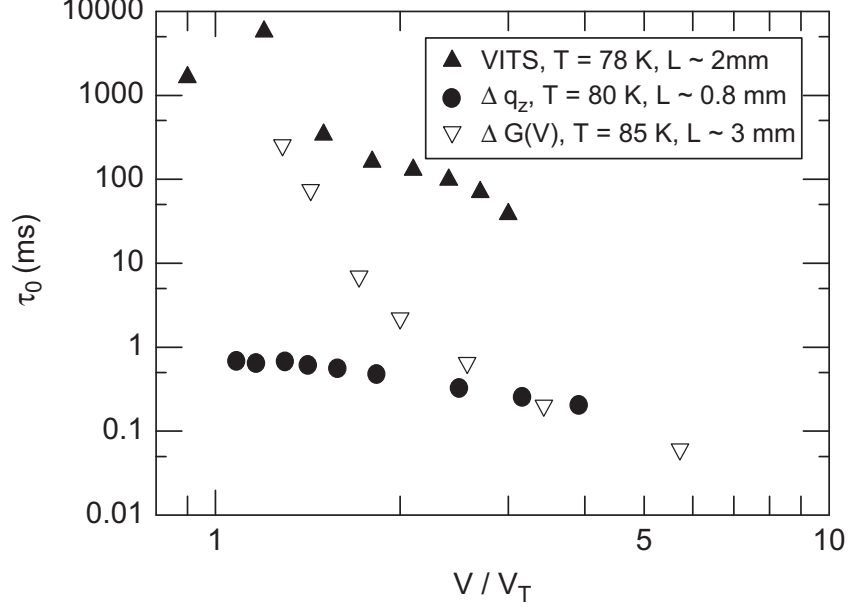


Figure 11.3: Voltage dependence of relaxation time constants associated with VITS (sample D), changes in the longitudinal wave vector ( $\Delta q_z$ ) [92] and changes in the shear modulus ( $\Delta G = 1/J$ ) [87]. The length and temperature of each sample is presented.

Recall for sample F that the hysteresis loop was fully suppressed for  $I_B = 0.8$  A. This corresponds to an initial twist of  $\beta L \sim 4^\circ$ . The shear compliance of  $\text{TaS}_3$  is  $G \sim 5$  GPa [80]. Assuming the azimuthal trans-modulus  $|\mu| \sim 10$  GPa is equal to the longitudinal trans-modulus [103] and a typical VITS response of  $\Delta\phi(L) \sim 0.1^\circ$ , the relative shift in the wave vector is calculated to be  $\Delta q_0(L)/q_{00} \sim 3 \times 10^{-3}$ . This value is comparable to the experimental result measured on  $\text{NbSe}_3$  [98, 106].

The main question left open is why is the VITS response so slow. Consider the voltage dependence of  $\tau_0$  for sample D which can be seen in Figure 11.3 along with the time constants associated with changes in the shear modulus ( $\tau(\Delta G) = \tau(1/\Delta J)$ ) [87] and changes in the longitudinal component of the wave vector ( $\tau(\Delta q_z)$ ) [92] obtained with three different samples at approximately 80 K. Our results suggests that the speed of the VITS response is determined by  $I_{\text{CDW}}$ , but it is not clear if the proportionality constant is significant. Since the VITS response is attributed to

voltage induced changes in the CDW wave vector coupling to the lattice and the elastic anomaly in the shear compliance is due to the CDW wave vector adjusting to the crystal strain, the time constants associated with the two processes are expected to be comparable. For large voltages, the time constants associated with changes in the shear compliance and the longitudinal wave vector are in fact comparable. However, the time constant associated with VITS surprisingly remains roughly two orders of magnitude larger at large voltages. This suggests that in order for  $I_{\text{CDW}}$  to create the strains in the crystal lattice, it must release defects such as dislocation lines.

## Chapter 12 Conclusions

In the SOC induced Mott insulator  $\text{Sr}_2\text{IrO}_4$ , we have observed high resolution topographic images of its surface resolving individual atomic steps. With tunneling spectroscopy at  $T = 77$  K, we have measured the Mott gap to be  $2\Delta \sim 615$  meV. In addition, at this temperature we observed an inelastic loss feature at approximately 125 meV attributed to a single magnon excitation. At  $T = 4.2$  K, additional low energy features were observed at 35 meV and 12 meV and are believed to be due to the additional magnetic ordering which occurs below  $T_N = 240$  K.

We have designed and constructed a new STM with ultra-high resolution capable of traversing macroscopic distances in two dimensions. It is sensitive enough to produce atomic resolution images of HOPG. In addition to being able to approach samples as any STM must do, it is also capable of traversing the entire width of our sample holders which have a diameter of 4 mm. It can produce numerous tunnel junctions without breaking the vacuum which makes it ideal for finding microscopically small samples such as graphene. In addition it can locate tiny features on a sample surface such as the interface between two dissimilar materials. It has proven to work at  $T = 77$  K by successfully approaching and imaging different sites on a gold surface. It is the ideal tool for any experiment requiring the sensitivity of an STM at sites separated by macroscopic distances on the material of interest.

We have observed the piezo-like VITS in single crystals of  $\text{TaS}_3$ . We have observed it to have an amplitude of roughly  $0.1^\circ$ . It is a very sluggish response with relaxation time constants that exceed 1 s near the CDW depinning threshold. Applying an external torque not only changes the magnitude of the VITS response but also the direction the crystals twist. The VITS response speeds up with increasing temperature and is related to the CDW current. We have shown through experimental

results and theoretical modeling that the VITS response could be due to an initial twist being present in the material. It is hopeful that similar materials will be used as microscopic torsional actuators.

## Bibliography

- [1] H. F. Hess, R. B. Robinson, and J. V. Waszczak, “Vortex-core structure observed with a scanning tunneling microscope,” *Phys. Rev. Lett.*, vol. 64, pp. 2711–2714, May 1990.
- [2] J. E. Hoffman, K. McElroy, D.-H. Lee, K. M. Lang, H. Eisaki, S. Uchida, and J. C. Davis, “Imaging quasiparticle interference in  $\text{Bi}_2\text{Sr}_2\text{CaCu}_2\text{O}_{8+\delta}$ ,” *Science*, vol. 297, pp. 1148–1151, 2002.
- [3] Y. Levi, O. Millo, N. D. Rizzo, D. E. Prober, and L. R. Motowidlo, “Scanning tunneling microscope studies of the superconductor proximity effect,” *Phys. Rev. B*, vol. 58, pp. 15128–15134, Dec 1998.
- [4] R. J. Hamers, R. M. Tromp, and J. E. Demuth, “Surface electronic structure of Si (111)-(7 $\times$ 7) resolved in real space,” *Phys. Rev. Lett.*, vol. 56, pp. 1972–1975, May 1986.
- [5] C. Wang, B. Giambattista, C. G. Slough, R. V. Coleman, and M. A. Subramanian, “Energy gaps measured by scanning tunneling microscopy,” *Phys. Rev. B*, vol. 42, pp. 8890–8906, Nov 1990.
- [6] U. Walter, R. E. Thomson, B. Burk, M. F. Crommie, A. Zettl, and J. Clarke, “Scanning tunneling microscopy of the blue bronzes  $(\text{Rb},\text{K})_{0.3}\text{MoO}_3$ ,” *Phys. Rev. B*, vol. 45, pp. 11474–11480, May 1992.
- [7] A. Bautista, V. Durairaj, S. Chikara, G. Cao, K.-W. Ng, and A. Gupta, “A study of the Mott transition in  $\text{Ca}_3\text{Ru}_2\text{O}_7$  by tunneling spectroscopy,” *Solid State Communications*, vol. 148, p. 240, 2008.
- [8] C. Ye, P. Cai, R. Yu, X. Zhou, W. Ruan, Q. Liu, C. Jin, and Y. Wang, “Visualizing the atomic scale electronic structure of the  $\text{Ca}_2\text{CuO}_2\text{Cl}_2$  Mott insulator,” *arXiv:1201.0342v1*, 2012.
- [9] J. Nichols, N. Bray-Ali, G. Cao, and K.-W. Ng, “Direct observation of the Mott gap in  $\text{Sr}_2\text{IrO}_4$  with a scanning tunneling microscope,” *Submitted to Phys. Rev. B*, 2012.
- [10] S. Gasiorowicz, *Quantum Physics*. Wiley, 3<sup>rd</sup> ed., 2003.
- [11] J. Bardeen, “Tunnelling from a many-particle point of view,” *Phys. Rev. Lett.*, vol. 6, pp. 57–59, Jan 1961.
- [12] C. J. Chen, *Introduction to Scanning Tunneling Microscopy*. Oxford University Press, 1993.
- [13] J. Tersoff and D. R. Hamann, “Theory and application for the scanning tunneling microscope,” *Phys. Rev. Lett.*, vol. 50, pp. 1998–2001, Jun 1983.

- [14] M. Tinkham, *Introduction to Superconductivity*. Robert I. Krieger Publishing Company, 1980.
- [15] S. H. Pan, E. W. Hudson, and J. C. Davis, “ $^3\text{He}$  refrigerator based very low temperature scanning tunneling microscope,” *Review of Scientific Instruments*, vol. 70, p. 1459, 1999.
- [16] A. K. Gupta and K.-W. Ng, “Compact coarse approach mechanism for scanning tunneling microscope,” *Review of Scientific Instruments*, vol. 72, p. 3552, 2001.
- [17] J. Nichols and K.-W. Ng, “Scanning tunneling microscope with two-dimensional translator,” *Review of Scientific Instruments*, vol. 82, p. 013706, 2011.
- [18] B. S. Elman, M. Shayegan, M. S. Dresselhaus, H. Mazurek, and G. Dresselhaus, “Structural characterization of ion-implanted graphite,” *Phys. Rev. B*, vol. 25, pp. 4142–4156, Mar 1982.
- [19] N. W. Ashcroft, *Solid State Physics*. Saunders College, 1976.
- [20] D. J. Griffiths, *Introduction to Quantum Mechanics*. Pearson Prentice Hall, 2005.
- [21] J. Callaway, *Quantum Theory of the Solid State*. Academic Press: New York and London, 1974.
- [22] J. J. J. Randall, L. Katz, and R. Ward, “The preparation of a strontium-iridium oxide  $\text{Sr}_2\text{IrO}_4$ ,” *Journal of the American Chemical Society*, vol. 79, p. 266, 1957.
- [23] M. K. Crawford, M. A. Subramanian, R. L. Harlow, J. A. Fernandez-Baca, Z. R. Wang, and D. C. Johnston, “Structural and magnetic studies of  $\text{Sr}_2\text{IrO}_4$ ,” *Phys. Rev. B*, vol. 49, pp. 9198–9201, Apr 1994.
- [24] J. Matsuno, Y. Okimoto, Z. Fang, X. Z. Yu, Y. Matsui, N. Nagaosa, M. Kawasaki, and Y. Tokura, “Metallic ferromagnet with square-lattice  $\text{CoO}_2$  sheets,” *Phys. Rev. Lett.*, vol. 93, p. 167202, Oct 2004.
- [25] R. S. Perry, F. Baumberger, L. Balicas, N. Kikugawa, N. J. C. Ingle, A. Rost, J. F. Mercure, Y. Maeno, Z. X. Shen, and A. P. Mackenzie, “ $\text{Sr}_2\text{RhO}_4$  : a new, clean correlated electron metal,” *New Journal of Physics*, vol. 8, no. 9, p. 175, 2006.
- [26] S. Chikara, O. Korneta, W. P. Crummett, L. E. DeLong, P. Schlottmann, and G. Cao, “Giant magnetoelectric effect in the  $J_{\text{eff}} = \frac{1}{2}$  Mott insulator  $\text{Sr}_2\text{IrO}_4$ ,” *Phys. Rev. B*, vol. 80, p. 140407, Oct 2009.
- [27] B. J. Kim, H. Jin, S. J. Moon, J.-Y. Kim, B.-G. Park, C. S. Leem, J. Yu, T. W. Noh, C. Kim, S.-J. Oh, J.-H. Park, V. Durairaj, G. Cao, and E. Rotenberg, “Novel  $J_{\text{eff}} = 1/2$  Mott state induced by relativistic spin-orbit coupling in  $\text{Sr}_2\text{IrO}_4$ ,” *Phys. Rev. Lett.*, vol. 101, p. 076402, Aug 2008.

- [28] F. Wang and T. Senthil, “Twisted hubbard model for  $\text{Sr}_2\text{IrO}_4$ : Magnetism and possible high temperature superconductivity,” *Phys. Rev. Lett.*, vol. 106, p. 136402, Mar 2011.
- [29] H. Watanabe, T. Shirakawa, and S. Yunoki, “Microscopic study of a spin-orbit-induced Mott insulator in Ir oxides,” *Phys. Rev. Lett.*, vol. 105, p. 216410, Nov 2010.
- [30] G. Cao, J. Bolivar, S. McCall, J. E. Crow, and R. P. Guertin, “Weak ferromagnetism, metal-to-nonmetal transition, and negative differential resistivity in single-crystal  $\text{Sr}_2\text{IrO}_4$ ,” *Phys. Rev. B*, vol. 57, pp. R11039–R11042, May 1998.
- [31] M. Ge, T. F. Qi, O. B. Korneta, D. E. De Long, P. Schlottmann, W. P. Crummett, and G. Cao, “Lattice-driven magnetoresistivity and metal-insulator transition in single-layered iridates,” *Phys. Rev. B*, vol. 84, p. 100402, Sep 2011.
- [32] B. J. Kim, H. Ohsumi, T. Komesu, S. Sakai, T. Morita, H. Takagi, and T. Arima, “Phase-sensitive observation of a spin-orbital Mott state in  $\text{Sr}_2\text{IrO}_4$ ,” *Science*, vol. 323, no. 5919, pp. 1329–1332, 2009.
- [33] S. J. Moon, H. Jin, W. S. Choi, J. S. Lee, S. S. A. Seo, J. Yu, G. Cao, T. W. Noh, and Y. S. Lee, “Temperature dependence of the electronic structure of the  $J_{\text{eff}} = \frac{1}{2}$  Mott insulator  $\text{Sr}_2\text{IrO}_4$  studied by optical spectroscopy,” *Phys. Rev. B*, vol. 80, p. 195110, Nov 2009.
- [34] J. Kim, D. Casa, M. H. Upton, T. Gog, Y.-J. Kim, J. F. Mitchell, M. van Veenendaal, M. Daghofer, J. van den Brink, G. Khaliullin, and B. J. Kim, “Magnetic excitation spectra of  $\text{Sr}_2\text{IrO}_4$  probed by resonant inelastic x-ray scattering: Establishing links to cuprate superconductors,” *Phys. Rev. Lett.*, vol. 108, p. 177003, Apr 2012.
- [35] Q. Wang, Y. Cao, J. A. Waugh, T. F. Qi, O. B. Korneta, G. Cao, and D. S. Dessau, “Dimensionality controlled Mott transition and correlation effects in single- and bi-layer perovskite iridates,” *submitted to Phys. Rev Lett.*, 2012.
- [36] C. Kittel, *Introduction to Solid State Physics*. Wiley, 8th ed., 2005.
- [37] M. F. Cetin, P. Lemmens, V. Gnezdilov, D. Wulferding, D. Menzel, T. Takayama, K. Ohashi, and H. Takagi, “Crossover from coherent to incoherent scattering in spin-orbit dominated  $\text{Sr}_2\text{IrO}_4$ ,” *arXiv:1201.3841v1 [cond-mat.str-el]*.
- [38] J. S. Blakemore, *Solid State Physics*. Cambridge University Press, 1985.
- [39] J. H. de Boer and E. J. W. Verwey, “Semi-conductors with partially and with completely filled 3d-lattice bands,” *Proceedings of the Physical Society*, vol. 49, p. 59, 1937.

- [40] N. F. Mott and R. Peierls, “Discussion of the paper by de Boer and Verwey,” *Proceedings of the Physical Society*, vol. 49, p. 72, 1937.
- [41] N. F. Mott, “The basis of the electron theory of metals, with special reference to the transition metals,” *Proceedings of the Physical Society*, vol. 62, p. 416, 1949.
- [42] J. Hubbard, “Electron correlations in narrow energy bands,” *Proceedings of the Royal Society of London*, vol. A276, p. 238, 1963.
- [43] J. Hubbard, “Electron correlations in narrow energy bands. II. the degenerate band case,” *Proceedings of the Royal Society of London*, vol. A277, p. 237, 1964.
- [44] J. Hubbard, “Electron correlations in narrow energy bands. III. an improved solution,” *Proceedings of the Royal Society of London*, vol. A281, p. 401, 1964.
- [45] F. Gebhard, *The Mott Metal-Insulator Transition*. Springer, 1997.
- [46] J. C. Slater, “Magnetic effects and the Hartree-Fock equation,” *Phys. Rev.*, vol. 82, pp. 538–541, May 1951.
- [47] E. Fradkin, *Field Theories of Condensed Matter Systems*. Addison-Wesley Publishing: Redwood City, CA, 1991.
- [48] O. B. Korneta, T. Qi, S. Chikara, S. Parkin, L. E. De Long, P. Schlottmann, and G. Cao, “Electron-doped  $\text{Sr}_2\text{IrO}_{4-\delta}$  ( $0 \leq \delta \leq 0.04$ ): Evolution of a disordered  $J_{\text{eff}} = \frac{1}{2}$  Mott insulator into an exotic metallic state,” *Phys. Rev. B*, vol. 82, p. 115117, Sep 2010.
- [49] T. Kwapiński and M. Jałochowski, “Signature of tip electronic states on tunneling spectra,” *Surface Science*, vol. 604, p. 1752, 2010.
- [50] X. Wang, E. Gull, L. de’ Medici, M. Capone, and A. J. Millis, “Antiferromagnetism and the gap of a Mott insulator: Results from analytic continuation of the self-energy,” *Phys. Rev. B*, vol. 80, p. 045101, Jul 2009.
- [51] A. Georges, G. Kotliar, W. Krauth, and M. J. Rozenberg, “Dynamical mean-field theory of strongly correlated fermion systems and the limit of infinite dimensions,” *Rev. Mod. Phys.*, vol. 68, pp. 13–125, Jan 1996.
- [52] D. C. Tsui, R. E. Dietz, and L. R. Walker, “Multiple magnon excitation in NiO by electron tunneling,” *Phys. Rev. Lett.*, vol. 27, pp. 1729–1732, Dec 1971.
- [53] G. Binnig and H. Rohrer, “Scanning tunneling microscopy,” *Helvetica Physica Acta*, vol. 55, pp. 726–735, 1982.
- [54] J. A. Stroscio and W. J. Kaiser, *Methods of Experimental Physics: Scanning Tunneling Microscopy*. Academic, 1993.



- [55] D. W. Pohl, “Dynamic piezoelectric translation devices,” *Review of Scientific Instruments*, vol. 58, no. 1, pp. 54–57, 1987.
- [56] C. Renner, P. Niedermann, A. D. Kent, and O. . Fischer, “A vertical piezoelectric inertial slider,” *Review of Scientific Instruments*, vol. 61, no. 3, pp. 965–967, 1990.
- [57] A. K. Gupta and K.-W. Ng, “Compact coarse approach mechanism for scanning tunneling microscope,” *Review of Scientific Instruments*, vol. 72, no. 9, pp. 3552–3555, 2001.
- [58] T. H. Chang, C. H. Yang, M. J. Yang, and J. B. Dettellis, “Cryogenic scanning tunneling microscope for quantum dot spectroscopy,” *Review of Scientific Instruments*, vol. 72, no. 7, pp. 2989–2995, 2001.
- [59] D. J. Peters and B. L. Blackford, “Piezoelectric bimorph-based translation device for two-dimensional, remote micropositioning,” *Review of Scientific Instruments*, vol. 60, no. 1, pp. 138–140, 1989.
- [60] J. Nichols and K.-W. Ng, “Scanning tunneling microscope with long range lateral motion,” *Physica B*, vol. 407, pp. 1852–1854, 2011.
- [61] G. Grüner, “The dynamics of charge-density waves,” *Rev. Mod. Phys.*, vol. 60, pp. 1129–1181, Oct 1988.
- [62] R. Comès, M. Lambert, H. Launois, and H. R. Zeller, “Evidence for a Peierls distortion or a Kohn anomaly in one-dimensional conductors of the type  $\text{K}_2\text{Pt}(\text{CN})_4\text{Br}_{0.30}\cdot x\text{H}_2\text{O}$ ,” *Phys. Rev. B*, vol. 8, pp. 571–575, Jul 1973.
- [63] F. Denoyer, F. Comès, A. F. Garito, and A. J. Heeger, “X-ray-diffuse-scattering evidence for a phase transition in tetrathiafulvalene tetracyanoquinodimethane (TTF-TCNQ),” *Phys. Rev. Lett.*, vol. 35, pp. 445–449, Aug 1975.
- [64] S. Kagoshima, H. Anzai, K. Kajimura, and T. Ishiguro, “Observation of the Kohn anomaly and the Peierls transition in TTF-TCNQ by x-ray scattering,” *Journal of the Physical Society of Japan*, vol. 39, p. 1143, 1975.
- [65] P. Monceau, N. P. Ong, A. M. Portis, A. Meerschaut, and J. Rouxel, “Electric field breakdown of charge-density-wave—induced anomalies in  $\text{NbSe}_3$ ,” *Phys. Rev. Lett.*, vol. 37, pp. 602–606, Sep 1976.
- [66] Z. Z. Wang, P. Monceau, H. Salva, C. Roucau, L. Guemas, and A. Meerschaut, “Charge-density-wave transport above room temperature in a polytype of  $\text{NbS}_3$ ,” *Phys. Rev. B*, vol. 40, pp. 11589–11593, Dec 1989.
- [67] T. Sambongi, K. Tsutsumi, Y. Shiozaki, and M. Yamamoto, “Peierls transition in  $\text{TaS}_3$ ,” *Solid State Communications*, vol. 22, p. 729, 1977.

- [68] G. Travaglini, P. Wachter, J. Marcus, and C. Schlenker, “The blue bronze  $\text{K}_{0.3}\text{MoO}_3$ : A new one-dimensional conductor,” *Solid State Communications*, vol. 37, no. 7, pp. 599 – 603, 1981.
- [69] M. Sato, H. Fujishita, and S. Hosnino, “Neutron scattering study on the structural transition of quasi-one-dimensional conductor  $\text{K}_{0.3}\text{MoO}_3$ ,” *Journal of Physics C: Solid State Physics*, vol. 16, p. L877, 1983.
- [70] K. Nomura, K. Kume, and M. Sato, “Incommensurate cdw in  $\text{Rb}_{0.3}\text{MoO}_3$ :  $^{87}\text{Rb}$  NMR,” *Solid State Communications*, vol. 57, no. 8, pp. 611 – 613, 1986.
- [71] H. Fujishita, M. Sato, and S. Hosnino, “Incommensurate superlattice reflections in quasi one dimensional conductors,  $(\text{MSe}_4)_2\text{I}$  (M=Ta and Nb),” *Solid State Communications*, vol. 49, p. 313, 1984.
- [72] P. Monceau, *Electronic Properties of Inorganic Quasi-One-Dimensional Compounds*. No. 2, D.Reidel Publishing Company, 1985.
- [73] P. A. Lee and T. M. Rice, “Electric field depinning of charge density waves,” *Phys. Rev. B*, vol. 19, pp. 3970–3980, Apr 1979.
- [74] V. Y. Pokrovskii, S. G. Zybtsev, and I. G. Gorlova, “Torsional strain of  $\text{TaS}_3$  whiskers on the charge-density wave depinning,” *Phys. Rev. Lett.*, vol. 98, p. 206404, May 2007.
- [75] K. Hasegawa, A. Maeda, S. Uchida, and S. Tanaka, “Non-linear conductivity of monoclinic  $\text{TaS}_3$ ,” *Physica B+C*, vol. 117-118, pp. 599–601, 1983.
- [76] C. Roucau, R. Ayroles, P. Monceau, L. Guemas, A. Meerschaut, and J. Rouxel, “Electron diffraction and resistivity measurements on the one-dimensional orthorhombic and monoclinic structures of  $\text{TaS}_3$ . comparison with  $\text{NbSe}_3$ ,” *Physica Status Solidi A*, vol. 62, p. 483, 1980.
- [77] J. Rouxel and C. Schlenker, *Charge Density Waves in Solids*, vol. 25 of *Modern Problems in Condensed Matter Sciences*. North Holland, 1989.
- [78] J. W. Brill and W. Roark, “Electric field dependence of elastic properties of  $\text{TaS}_3$ ,” *Phys. Rev. Lett.*, vol. 53, pp. 846–849, Aug 1984.
- [79] G. Mozurkewich, P. Chaikin, W. Clark, and G. Gruner, “Elastic properties of linear charge density wave materials in the regime of nonlinear conduction,” *Solid State Communications*, vol. 56, p. 421, 1985.
- [80] X. D. Xiang and J. W. Brill, “Shear modulus of  $\text{TaS}_3$ ,” *Phys. Rev. B*, vol. 36, pp. 2969–2971, Aug 1987.
- [81] S. Hoen, B. Burk, A. Zettl, and M. Inui, “Metastable length states of a random system:  $\text{TaS}_3$ ,” *Phys. Rev. B*, vol. 46, pp. 1874–1877, Jul 1992.

- [82] M. E. Itkis, F. Y. Nad', and V. Y. Pokrovskii, "Laser-induced emf in the quasi-one-dimensional conductor  $\text{TaS}_3$ ," *Soviet Physics Journal of Experimental and Theoretical Physics*, vol. 90, p. 307, 1986.
- [83] X.-D. Xiang, J. W. Brill, and W. L. Fuqua, "Use of a helical resonator as a capacitive transducer in vibrating reed measurements," *Review of Scientific Instruments*, vol. 60, p. 3035, 1989.
- [84] S. G. Zybtsev, M. V. Nikitin, and V. Y. Pokrovskii, "Shapiro steps in the torsion of a quasi-one-dimensional conductor  $\text{TaS}_3$ ," *Journal of Experimental and Theoretical Physics Letters*, vol. 92, pp. 405–409, 2010.
- [85] X. Zhan, *Shear Compliance of  $\text{TaS}_3$* . PhD thesis, University of Kentucky, 1997.
- [86] X. Zhan and J. W. Brill, "Static and low-frequency shear compliance of  $\text{TaS}_3$ ," *Phys. Rev. B*, vol. 52, pp. R8601–R8604, Sep 1995.
- [87] X. Zhan and J. W. Brill, "Frequency and voltage dependence of the complex shear compliance of  $\text{TaS}_3$ : A relaxation analysis," *Phys. Rev. B*, vol. 56, pp. 1204–1212, Jul 1997.
- [88] R. E. Thorne, "A history of the I-V characteristic of CDW conductors," *Journal of Physics IV France*, vol. 131, p. 89, 2005.
- [89] A. H. Thompson, A. Zettl, and G. Grüner, "Charge-density-wave transport in  $\text{TaS}_3$ ," *Phys. Rev. Lett.*, vol. 47, pp. 64–67, Jul 1981.
- [90] M. E. Itkis, F. Y. Nad', and P. Monceau, "Nonlinear conductivity of quasi-one-dimensional  $\text{TaS}_3$  at low temperatures," *Journal of Physics: Condensed Matter*, vol. 2, p. 8237, 1990.
- [91] V. Pokrovskii and S. G. Zybtsev, "Self-sensitive torsional microresonators based on a charge-density wave system," *arXiv:0708:2694*, 2007.
- [92] R. C. Rai and J. W. Brill, "Dynamics of the electroreflective response of  $\text{TaS}_3$ ," *Phys. Rev. B*, vol. 70, p. 235126, Dec 2004.
- [93] L. Ladino and J. W. Brill, "Frequency domain simulations of charge-density-wave strains: Comparison with electro-optic measurements," *Solid State Communications*, vol. 145, p. 469, 2008.
- [94] K. S. Cole and R. H. Cole, "Dispersion and absorption in dielectrics i. alternating current characteristics," *Journal of Chemical Physics*, vol. 9, p. 341, 1941.
- [95] S. Havriliak and S. Negami, "A complex plane representation of dielectric and mechanical relaxation processes in some polymers," *Polymer*, vol. 8, p. 161, 1967.

- [96] V. Pokrovskii, S. Zybtssev, V. B. Loginov, V. Timofeev, D. Kolesov, I. Yaminsky, and I. Gorlova, “Deformations of charge-density wave crystals under electric field,” *Physica B: Condensed Matter*, vol. 404, p. 437, 2009.
- [97] L. Ladino, J. W. Brill, M. Freamat, M. Uddin, and D. Dominko, “Dynamics of the electro-optic response of blue bronze  $\text{K}_{0.3}\text{MoO}_3$ ,” *Phys. Rev. B*, vol. 74, p. 115104, Sep 2006.
- [98] T. L. Adelman, M. C. de Lind van Wijngaarden, S. V. Zaitsev-Zotov, D. DiCarlo, and R. E. Thorne, “Spatially resolved studies of charge-density-wave dynamics and phase slip in  $\text{NbSe}_3$ ,” *Phys. Rev. B*, vol. 53, pp. 1833–1849, Jan 1996.
- [99] M. E. Itkis, B. M. Emerling, and J. W. Brill, “Imaging charge-density-wave strains with electromodulated transmission,” *Phys. Rev. B*, vol. 52, pp. R11545–R11548, Oct 1995.
- [100] S. Brazovskii, N. Kirova, H. Requardt, F. Y. Nad, P. Monceau, R. Currat, J. E. Lorenzo, G. Grübel, and C. Vettier, “Plastic sliding of charge density waves: X-ray space resolved-studies versus theory of current conversion,” *Phys. Rev. B*, vol. 61, pp. 10640–10650, Apr 2000.
- [101] M. E. Itkis, B. M. Emerling, and J. W. Brill, “Electrooptical imaging of charge-density wave phase gradients: polarity and temperature dependence of phase slip,” *Synthetic Metals*, vol. 86, p. 1959, 1997.
- [102] F. Nad’, M. E. Itkis, P. Monceau, and M. Renard, “Spatial distribution of charge-density-wave excitations due to current conversion near contacts,” *Journal de Physique IV*, vol. 03, p. 175, 1993.
- [103] A. V. Golovnya, V. Y. Pokrovskii, and P. M. Shadrin, “Coupling of the lattice and superlattice deformations and hysteresis in thermal expansion for the quasi-one-dimensional conductor  $\text{TaS}_3$ ,” *Phys. Rev. Lett.*, vol. 88, p. 246401, May 2002.
- [104] W. C. Young, *Roark’s Formulas for Stress and Strain*. McGraw-Hill Book Company, 6th ed., 1989.
- [105] S. P. Timoshenko and J. N. Goodier, *Theory of Elasticity*. McGraw-Hill Book Company, 3rd ed., 1970.
- [106] D. DiCarlo, E. Sweetland, M. Sutton, J. D. Brock, and R. E. Thorne, “Field-induced charge-density-wave deformations and phase slip in  $\text{NbSe}_3$ ,” *Phys. Rev. Lett.*, vol. 70, pp. 845–848, Feb 1993.

## **VITA**

**John A. Nichols**

### **Place of Birth:**

Nuremberg, Bavaria, Germany  
May 4, 1982

### **Education:**

University of Kentucky  
Lexington, KY  
M.S., Physics  
August 2008

University of the Cumberlands  
Williamsburg, KY  
B.S., Physics and B.S., Mathematics  
May 2004

### **Professional Positions:**

University of Kentucky  
Research Assistant  
May 2008 - Present

University of Kentucky  
Teaching Assistant  
June 2006 - May 2008

University of Kentucky  
University Fellowship  
August 2004 - June 2006

## Publications:

“Direct observation of the Mott gap in  $\text{Sr}_2\text{IrO}_4$  with a scanning tunneling microscope”, J. Nichols, N. Bray-Ali, G. Cao, K.-W. Ng, *Submitted to Physical Review B*.

“Scanning tunneling microscope with long range lateral motion”, J. Nichols, K.-W. Ng, *Physica B: Condensed Matter* **407**, 1852 (2012). [Proceedings]

“Electromechanical response of sliding charge-density-waves: Voltage-induced torsional strain in tantalum trisulfide”, J. W. Brill, H. Zhang, J. Nichols, *Physica B: Condensed Matter* **407**, 1737 (2012). [Proceedings]

“Torque and temperature dependence of the hysteretic voltage-induced torsional strain in tantalum trisulfide”, H. Zhang, J. Nichols, and J. W. Brill, *Physical Review B* **84**, 125134 (2011).

“Scanning tunneling microscope with two-dimensional translator”, J. Nichols and K.-W. Ng, *Review of Scientific Instruments* **82**, 013706 (2011).

“Dynamics of the hysteretic voltage-induced torsional strain in tantalum trisulfide”, J. Nichols, C. Sandamali Weerasooriya, and J. W. Brill, *Journal of Physics: Condensed Matter* **22**, 334224 (2010).

“Erratum: Characterization of the torsional piezoelectric like response of tantalum trisulfide associated with charge-density-wave depinning”, J. Nichols, D. Dominko, L. Ladino, J. Zhou, and J. W. Brill, *Physical Review B*, **80**, 039903 (2009).

“Characterization of the torsional piezoelectric like response of tantalum trisulfide associated with charge-density-wave depinning”, J. Nichols, D. Dominko, L. Ladino, J. Zhou, and J. W. Brill, *Physical Review B*, **79**, 241110(R) (2009).